

UNIVERSITY OF SÃO PAULO
GEOSCIENCES INSTITUTE

**Deformation regime variations across the Neoproterozoic Araçuaí hot orogen (SE
Brazil): insights from structural and magnetic fabric analyses**

TIAGO VALIM ANGELO

Master Dissertation submitted to the
Geosciences Institute of the University of
São Paulo to obtain a Master of Science
degree.

Concentration area: Geotectonics

Advisor: Prof. Dr. Marcos Egydio-Silva

SÃO PAULO

2019

UNIVERSIDADE DE SÃO PAULO
INSTITUTO DE GEOCIÊNCIAS

**Deformation regime variations across the Neoproterozoic Araçuaí
hot orogen (SE Brazil): insights from structural and magnetic
fabric analyses**

TIAGO VALIM ANGELO

Orientador: Prof. Dr. Marcos Egydio da Silva

Dissertação de Mestrado

Nº 831

COMISSÃO JULGADORA

Dr. Marcos Egydio da Silva

Dr. Vinícius Tieppo Meira

Dr. Eric Tohver

SÃO PAULO
2019

Autorizo a reprodução e divulgação total ou parcial deste trabalho, por qualquer meio convencional ou eletrônico, para fins de estudo e pesquisa, desde que citada a fonte.

Serviço de Biblioteca e Documentação do IGc/USP
Ficha catalográfica gerada automaticamente com dados fornecidos pelo(a) autor(a)
via programa desenvolvido pela Seção Técnica de Informática do ICMC/USP

Bibliotecários responsáveis pela estrutura de catalogação da publicação:
Sonia Regina Yole Guerra - CRB-8/4208 | Anderson de Santana - CRB-8/6658

Angelo, Tiago Valim
Deformation regime variations across the
Neoproterozoic Araçuaí hot orogen (SE Brazil):
insights from structural and magnetic fabric
analyses / Tiago Valim Angelo; orientador Marcos
Egydio-Silva. -- São Paulo, 2019.
113 p.

Dissertação (Mestrado - Programa de Pós-Graduação
em Geoquímica e Geotectônica) -- Instituto de
Geociências, Universidade de São Paulo, 2019.

1. fluxo magmático. 2. Faixa Araçuaí. 3.
anisotropia de susceptibilidade magnética. 4.
magnetismo de rochas. 5. petrotrama. I. Egydio-
Silva, Marcos, orient. II. Título.

ACKNOWLEDGMENTS

I would like to express my sincere gratitude to my family, who have been very supportive and helpful and encouraged me every step of the way. Although we were separated during my postgraduate studies, I always took with me all the affection to go forward.

Thank you very much, Prof. Dr. Marcos Egydio-Silva, for guiding me throughout this research experience. Your uncommon patience, friendship, conversations, and disponibility were fundamental for the completion of this work.

A great thank to Adriano and Ubiratan from the Geosciences Institute (IGc-USP), who helped in our fieldwork missions with enthusiasm and determination. Moreover, I would like to thank the geochronology staff from the Universities of Brasília and São Paulo for sample preparation, and Dr. Irene Raposo from the Anisotropy laboratory housed at IGc-USP for our discussions and experiments.

I thank Ph.D. candidate and friend Filipe Temporim for his help during data acquisition and processing at the Paleomagnetism Laboratory (IAG-USP). Our discussions regarding rock magnetism and hot orogenic settings really helped me in the preparation of this manuscript.

I am also grateful to Marina. Thank you for your enormous encouragement, companionship, and your dedication to our plans. Your support was fundamental in this journey and has been the greatest help I have received.

ABSTRACT

Angelo, T. V., 2019, Deformation regime variations across the Neoproterozoic Araçuaí hot orogen (SE Brazil): insights from structural and magnetic fabric analyses [Master's Thesis], São Paulo, Instituto de Geociências, Universidade de São Paulo, 113p.

The Neoproterozoic Araçuaí belt of East Brazil formed during the amalgamation of Western Gondwana and holds characteristics of a hot collisional belt, involving large amount of magma, partial melting of the middle crust, and slow cooling rates. This work combines structural analysis, magnetic fabric, and geochronological studies in order to access information related to the flow of rocks, deformation history, and structural patterns associated with the behavior of this orogenic setting. Microstructural observations support that deformation of the plutonic bodies occurred in the magmatic state while the host metasedimentary and basement rocks remained in the solid-state. A detailed structural mapping integrating field and anisotropy of magnetic susceptibility (AMS) revealed four domains with contrasting flow patterns. The structural patterns from W to E are characterized by: westward thrusting orthogonal to the belt (region 1), orogen-parallel transpression induced strain partitioning (regions 2 and 3), and orogen-parallel flow and subsidiary eastward vergence magmatic flow (region 4). Anisotropy of anhysteretic remanent magnetization (AARM) and magnetic mineralogy investigations suggest that the main carriers of the AMS are biotite and/or amphibole in paramagnetic samples (host metasediments and basement unit), and multi-domain (MD) or pseudo-single domain (PSD) magnetite grains in ferromagnetic materials (hosted in plutonic bodies). U-Pb dating of zircons from granitoids in the western arc border and central arc regions (structural regions 1, 2, and 3) reveal that magmatism occurred between 615-567 Ma. Microstructural investigations in the igneous bodies suggest that deformation occurred before complete solidification. This magmatism is associated with the main tectono-metamorphic peak attained by the orogen. To the east (structural region 4), younger bodies were emplaced in a still thermally buffered environment, but after solidification of the anatectic country rock. This late magmatism (540-480 Ma) is associated with a minor tectono-metamorphic peak, and magmatic deformation affected these bodies during that time. In the context of protracted deformation under slow cooling conditions, the composite observed fabric results from the interplay of collision-driven (thrusting and transpression strain partitioning) and gravity-driven (orogen-parallel flow) deformations, induced by the East-West convergence between the São Francisco and Congo Cratons.

Keywords: magmatic flow; anisotropy of magnetic susceptibility; rock magnetism; Araçuaí belt, magnetic fabric; hot orogen

RESUMO

Angelo, T. V., 2019, Variações no regime de deformação de uma crosta orogênica quente: análise estrutural e de fábrica magnética na Faixa Araçuaí (Sudeste do Brasil) [Dissertação de Mestrado], São Paulo, Instituto de Geociências, Universidade de São Paulo, 113p.

A Faixa Araçuaí formada no Neoproterozóico durante a aglutinação do Gondwana Ocidental possui características de um cinturão colisional “quente”, envolvendo amplo magmatismo, fusão parcial da crosta média e baixas taxas de resfriamento. Este trabalho combina estudo estrutural, magnético e geocronológico para acessar informações relacionadas ao fluxo das rochas, histórico de deformação e padrões estruturais associados ao comportamento desse orógeno. Observações microestruturais sustentam que a deformação dos corpos plutônicos ocorreu no estado magmático; enquanto as rochas metassedimentares e do embasamento no estado sólido. Mapeamento estrutural detalhado integrando medidas obtidas em campo e através de anisotropia de susceptibilidade magnética (ASM) revelou quatro domínios com padrões de distribuição da deformação contrastantes. Os padrões estruturais de W a E são caracterizados por: esforços contracionais para oeste com orientação ~NS (perpendicular à estruturação do orógeno) (região 1), partição de deformação induzida por transpressão paralela à faixa orogênica (regiões 2 e 3) e fluxo magmático horizontal e de vergência para leste (região 4). Anisotropia anisterética de remanência magnética (AARM) e investigações de mineralogia magnética sugerem que os principais carreadores da ASM são biotita e / ou anfibólio em amostras paramagnéticas (metassedimentos do hospedeiro e unidade do embasamento), e grãos de magnetita multi-domínio (MD) ou pseudo-domínio simples (PSD) em materiais ferromagnéticos (corpos magmáticos). Datações U-Pb de zircões de granitóides nas regiões de oeste e central do arco magmático na área de estudo (regiões estruturais 1, 2 e 3) revelam que o magmatismo ocorreu entre 615-567 Ma, e a deformação ocorreu antes da cristalização. Este magmatismo está associado ao principal pico tectono-metamórfico atingido pelo orógeno. Para o leste (região estrutural 4), os corpos mais jovens foram intrudidos ainda em condições de temperatura elevada, mas após a solidificação da rocha hospedeira. Este magmatismo tardio (540-480 Ma) está associado a um pico tectono-metamórfico menor, e a deformação magmática afetou esses corpos durante este período. Nesse contexto de deformação prolongada sob condições de resfriamento lentas, as contrastantes fábricas observadas resultam da interação de deformações acionadas por colisão (partição da deformação por esforços contracionais e transpressionais) e por gravidade (fluxo orogênico paralelo) induzidas pela convergência Leste-Oeste entre os crátons São Francisco e Congo.

Palavras-chave: fluxo magmático; anisotropia de susceptibilidade magnética; magnetismo de rocha; Faixa Araçuaí; fábrica magnética; orógeno quente

SUMMARY

CHAPTER I	1
I.1. INTRODUCTION	1
I.2. OBJECTIVES	2
I.3. LOCALIZATION AND ACCESS TO THE STUDY AREA	2
I.4. PRESENTATION AND STRUCTURE OF THE DISSERTATION	3
CHAPTER II.....	5
II.1 MATERIALS AND METHODS	5
II.1.1. Fieldwork and Sampling	5
II.1.2. Microstructural Investigations	5
II.1.3. Anisotropy of Magnetic Susceptibility (AMS).....	5
II.1.3.1. Rock magnetism	5
II.1.3.2. Magnetic behaviors	7
II.1.3.3. Magnetic domains	9
II.1.3.4. The relation between magnetic fabric and petrofabric	11
II.1.3.5. Magnetic mineralogy investigations	13
II.1.3.6. Analytical method	13
II.1.4. U-Pb Zircon (LA-ICP-MS) Geochronology	14
II.1.4.1. Analytical method	16
CHAPTER III	19
III.1. GEOLOGICAL BACKGROUND	19
III.1.1. The Western Gondwana	19
III.1.2. The Ribeira-Araçuaí Orogenic System.....	21
III.1.3. The Araçuaí Orogenic Belt	24
II.1.3.1. Tectonic and structural framework.....	25
II.1.3.2. Lithological units.....	27
II.1.3.2.1. The Basement	28
II.1.3.2.2. Paleo/Mesoproterozoic Rift Assemblage	29
II.1.3.2.3. Basin Material.....	30
II.1.3.2.4. Magmatic suites	32
II.1.3.3 Tectonic evolution models of the Araçuaí orogen	38
CHAPTER IV	43
IV.1. INTRODUCTION	44
IV.2. GEOLOGICAL SETTING	45
IV.3. THE CENTRAL PLUTONIC UNIT	49
IV.3.1. The imbricated synkinematic magmatic São Vitor Tonalite and metasedimentary host rock.....	49

IV.3.2. Arc western border – The Guarataia, Brasilândia and Chaves plutons and the Mantiqueira Complex (Western Mylonitic Unit)	51
IV.3.2. Arc eastern border - The Aimorés Suite (emplaced in the Eastern AnatecticUnit)	52
IV.4. ANISOTROPY OF MAGNETIC SUSCEPTIBILITY (AMS)	54
IV.4.1 The AMS and macrostructural fabrics	56
IV.4.2 Magnetic mineralogy investigation.....	60
IV.4.3 Anisotropy of anhysteretic remanent magnetization (AARM)	65
IV.5. U-PB ZIRCON (LA-ICP-MS) GEOCHRONOLOGY	67
IV.5.1 Sampling and methods	67
IV.5.2 Results	68
IV.6. DISCUSSION	75
IV.6.1. Significance of magnetic fabrics	75
IV.6.2. Microstructures	77
IV.6.3. Geochronology	78
IV.6.4. Structural setting	79
IV.7. CONCLUSIONS	82
CHAPTER V	85
V.1. SYNTHESIS AND CONCLUSIONS	85
REFERENCES	87
APPENDIX.....	101
APPENDIX A – Location of the visited points in the study area and compiled measurements.....	101
APPENDIX B – Ages obtained in the study region	102
APPENDIX C – Parameters of the Vibrating Sample Magnetometer.	103
APPENDIX D – AMS graphs and directional parameters.	104

CHAPTER I

I.1. INTRODUCTION

Convergent continental margins and zones of continental collision are characterized by the formation of mountain belts, which are areas that are affected by deformation, widespread metamorphism, magmatism, pluton emplacement, and sometimes extensive partial melting of the continental crust. Recently, a growing body of research is concerned with the study of partially molten crusts involved in continental collision and how deformation is accommodated in such orogens. Seismological investigations in the Tibetan plateau (Brown, et al., 1996; Nelson, et al., 1996; Alsdorf and Nelson, 1999), Altiplano (Partzsch et al., 2000), and Pyrenees (Pous et al., 1995) indicate that the middle crust is partially molten, containing large amounts of melt as anatexis or incompletely solidified plutons. These studies gave birth to the concept of “hot orogens”.

Such “hot orogens” are characterized by high temperature, slow cooling rates, and excessive amount of melt in the hinterland, behaving with decreased rock strength due to the effects of large volume of magma in the crust. Abnormally high geotherms ($>30^{\circ}\text{C}/\text{km}$) and slow cooling ($\ll 10^{\circ}\text{C}/\text{Ma}$) promote partial melting of a large volume of the middle crust. As a consequence, these orogens evolve atop a very hot mantle and are subjected to magmatism over long periods, leading to an extremely mechanically weak behavior over protracted periods of deformation.

An associated issue with these hot orogenic domains is the strain repartition within the middle- to lower-crust and constraints on how it operates are being investigated from both field investigations (such as this study) and analogue and numerical modelling (e.g. Cagnard et al., 2006; Beaumont et al., 2006; Duclaux et al., 2007). Collisional belts involving a stiff lithosphere tend to localize strain within major shear zones. However, under high-temperature conditions due to high radioactive heat production (e.g. Jamieson et al., 1988; Sandiford and McLaren, 2002; Faccenda et al., 2008) partial melting is pervasive in the middle crust and strain repartition is less efficient, leading to homogeneous deformation of a large volume of rocks (Vauchez and Tommasi, 2003; Vauchez et al., 2007). These conditions lead to a weak lithosphere that becomes unable to sustain the load of high topographies and the gravitational potential energy stored in thickened crust during convergence can be released via lateral spreading (e.g. Rey et al., 2001) along magmatic channeled flows. In this context, a complex structural pattern would be promoted as a result of the combination of gravity forces and

tangential tectonics related to plates convergence. Evaluating the flow of “hot” orogenic crust deformed under high geothermal gradient is, therefore, a key aspect for understanding the structural patterns in the deep crust.

I.2. OBJECTIVES

In this present work, the focus is on the Neoproterozoic Araçuaí orogen, which is the northern segment of the Ribeira-Araçuaí orogenic system formed during the Brasiliano/Pan-African Orogeny during the amalgamation of West Gondwana (Almeida et al., 1977; Bento dos Santos et al., 2015). This collisional belt experienced slow regional cooling, high temperature, and low pressure conditions (Petitgirard et al., 2009; Cavalcante et al., 2014; Moraes et al., 2015; Richter et al., 2016), where large volumes of magma were emplaced and deformed before solidification (Vauchez et al., 2007; Mondou et al., 2012; Cavalcante et al., 2014). The objective is to characterize the deformation framework of the partially molten crust using anisotropy of magnetic susceptibility (AMS) to define the structural fabric of syn- to late-magmatic bodies intruded in high-temperature metasedimentary rocks. A detailed rock magnetism investigation was performed in order to confirm if magnetic fabric obtained from AMS can be used as a proxy for petrofabric. In addition, the study incorporates a new U-Pb zircon crystallization age for a syn-kinematic tonalitic body emplaced within metasediments. Combining these procedures with existing structural and geochronological data from the literature allow a discussion regarding the deformation history associated with the behavior of this orogenic setting.

I.3. LOCALIZATION AND ACCESS TO THE STUDY AREA

The study area (Figure 1) is located in the eastern portion of the Minas Gerais State (Brazil), between the towns of Governador Valadares to the south and Teófilo Otoni to the north, corresponding to part of the geological sheets of Teófilo Otoni SE.24-V-C-IV (Paes, 2000), Itambacuri SE.24-Y-A-I (Signorelli, 2000), Ataléia SE.24-V-A-II (Tuller, 2000), and Mucuri SE.24-V-C-V (Moreira, 2000), mapped by the “Projeto Leste” survey. The ca. 6.330 Km² study region includes the towns of Itambacuri, Frei Gaspar, Ouro Verde de Minas, Ataléia, and Nova Módica (Figure 1). The delimitation of the area is given by the decimal degrees coordinates: -41.995 / -17.925; -41.048 / -17.925; -41.048 / -18.462; -41.995 / -18.462 (datum: WGS 1984). The main access is made by the BR-116 highway, which connects the states of Rio de Janeiro and Bahia.

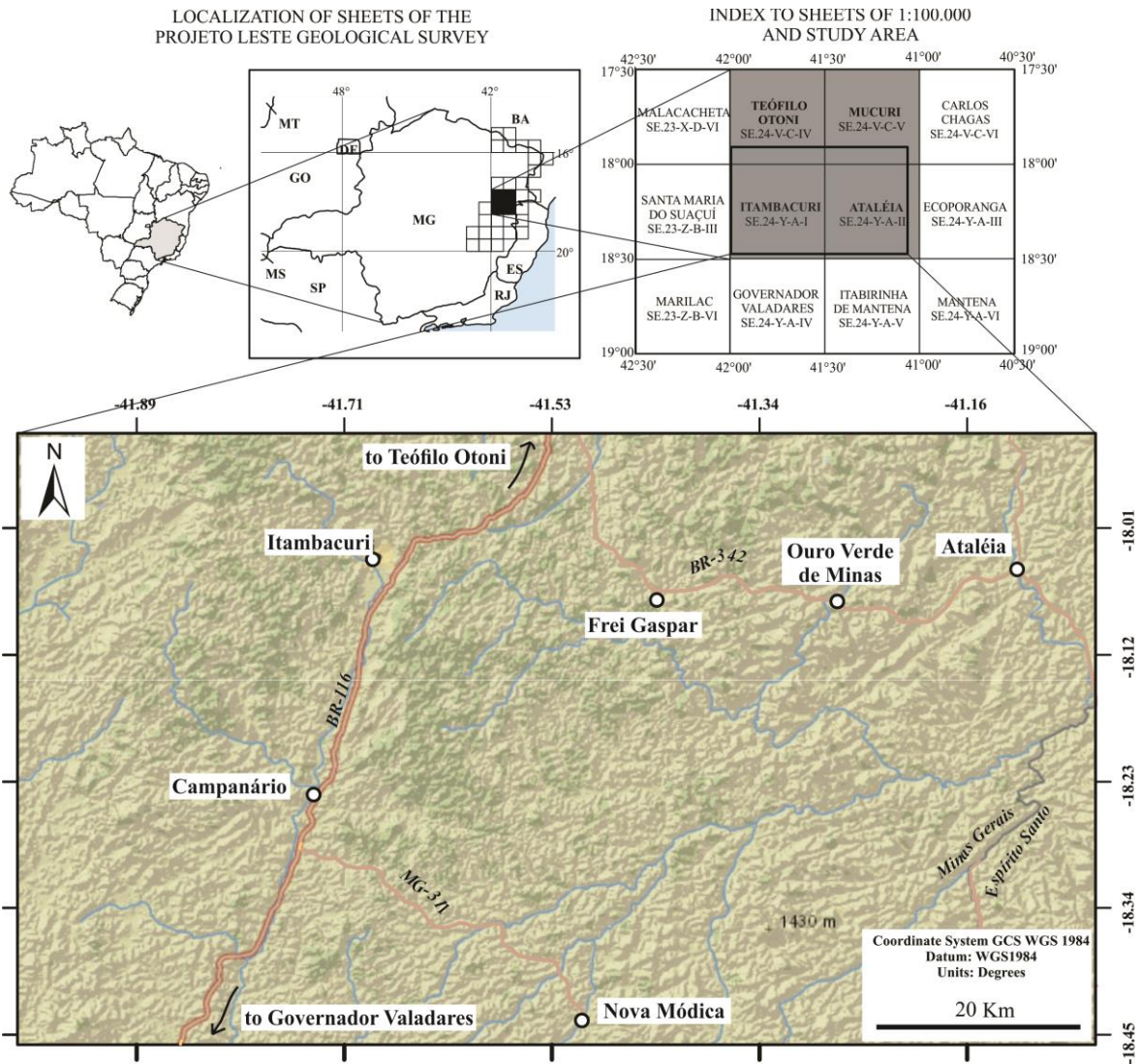


Figure 1 - Localization of the study area within the sheets of 1:100.000 mapped by the “Projeto Leste” survey. Main roads and towns within the study area are also shown.

I.4. PRESENTATION AND STRUCTURE OF THE DISSERTATION

The present study results from a multidisciplinary approach that focuses on the deformation regime variations across a segment of the Araçuaí orogen, that displays evidence of high-temperature contractional deformation. The dissertation consists of five chapters, with, one chapter presented in the form of scientific manuscript. The current chapter (I) introduces the research theme and aims of the work. Chapter II presents the materials and methods utilized in the development of this research to achieve the objectives. Chapter III describes a synthesis of the geological context that the studied region is inserted, highlighting the geotectonic framework of the Neoproterozoic-Cambrian Pan-African Orogenic System in West Gondwana, and the consequent formation of the Neoproterozoic Araçuaí belt by the convergence between the Congo (Africa) and São Francisco (Brazil) cratons. Chapter IV is

organized in scientific manuscript form, which is titled “Midcrust deformation regime variations across the Neoproterozoic Araçuaí hot orogen (SE Brazil): insights from structural and magnetic fabric analyses”, submitted to the Journal of Structural Geology. The paper deals with the results obtained from field and AMS measurements, microstructural observations, magnetic mineralogy investigations, and new geochronological results. The last chapter (V) synthesizes the results and discussions obtained in the master’s dissertation, final considerations, and suggestions for future works.

CHAPTER II

II.1 MATERIALS AND METHODS

In this research, the approach carried out to achieve the proposed objectives followed the application of different techniques regarding structural mapping, rock deformation, rock magnetism, and geochronology. The present study was developed alternating field and laboratory work, and the details about the methods applied are described in this chapter.

II.1.1. Fieldwork and Sampling

Fieldwork for this study was conducted in a total of thirteen days, during December 2017 and May 2018. Geological and structural mapping involving the characterization of the outcropping lithotypes and measurements of planar and linear elements was performed together with sampling for petrography and microstructural studies, AMS, magnetic mineralogy investigations, and geochronology.

II.1.2. Microstructural Investigations

A total of 26 thin sections were studied in order to access information regarding the mineralogical composition of the main lithotypes of the study area and determine magmatic versus solid-state deformation fabrics. Thin sections were described and imaged under an Olympus BX 50 petrographic microscope hosted in the Geosciences Institute of the University of São Paulo. Microstructures were identified following definitions provided by Vernon (2004) and Passchier and Trouw (2005) during this step.

II.1.3. Anisotropy of Magnetic Susceptibility (AMS)

II.1.3.1. Rock magnetism

The induced volumetric magnetization of a rock is a function of its magnetic history, and its characterization is made in terms of two vectors: applied magnetic field (H) and induced magnetization (M). Many materials define a linear correlation between M and H so that $M=KH+M_r$, where KH is the induced part that occurs only under the presence of an applied magnetic field, and M_r is the remanent magnetization (a permanent component of the magnetization when H is removed). The term K (adimensional) is a function of H and it is denominated magnetic susceptibility.

The magnetic susceptibility is an intrinsic physical property of materials and may be regarded as their magnetizability (Butler, 1992). It represents the ratio between the induced magnetization M and the applied field H ($K=M/H$), which results in the measurement of the response of a crystalline substance submitted to an applied field. Rocks in which the intensity of magnetization (whether induced or remanent) depends on the direction of the applied magnetic field display magnetic anisotropy. In this case, the magnetic susceptibility can be described by a symmetrical second rank tensor, and geometrically by an ellipsoid (Tarling and Hrouda, 1993).

The anisotropy of minerals comprises two components, the magnetocrystalline anisotropy, and the shape anisotropy. The magnetocrystalline anisotropy is related to the mineral lattice, where magnetic susceptibility is higher along specific crystallographic axes. The shape anisotropy results from the mineral grain shape or distribution of minerals within a rock. When an external field is applied in asymmetric grains, magnetostatic forces are minimum when the superficial poles are distant and preferential magnetization forms along the long crystallographic axes. The shape anisotropy is important in minerals that crystallize in isometric system such as magnetite, where crystalline anisotropy is reduced.

In an isotropic medium, K is a simple scalar; however, in minerals, variation in chemical composition, defects in the crystal lattice, or even the particular disposition of magnetic moments can create anisotropies. In such cases, the susceptibility varies in function of the direction of the applied field. When the material is anisotropic, K is a second rank tensor described through the equation $M_i = K_{ij}H_j$. The magnitude and the principal directions of the magnetic susceptibility are defined by the three diagonal and symmetrical terms of the magnetic susceptibility K_{ij} tensor, K_{11} , K_{22} , and K_{33} . The susceptibility anisotropy ($K_1 > K_2 > K_3$) can be represented by a triaxial ellipsoid, in which each axis define one of the respective main susceptibilities (Hrouda, 1982). K_1 represents the magnetic lineation and K_3 the magnetic foliation pole.

Several parameters are used to quantify the symmetry of the ellipsoid. The most representative can be estimated through the corrected degree of anisotropy (P') and the shape factor (T), defined by Jelinek (1981) as: $P' = \exp\{(\ln K_1 - \ln K_m)^2 + (\ln K_2 - \ln K_m)^2 + (\ln K_3 - \ln K_m)^2\}^{1/2}$ and $T = (\ln(K_2 / K_3) - \ln(K_1 / K_2)) / (\ln(K_2 / K_3) + \ln(K_1 / K_2))$.

The susceptibility is isotropic if $P'=1$ and the ellipsoid is a sphere. The degree of eccentricity increases if P' values increase. The shape of the ellipsoid can be oblate when

$0 < T \leq 1$ ($K_1 = K_2 \gg K_3$), prolate when $-1 \leq T < 0$ ($K_1 > K_2 = K_3$), or triaxial when $T = 0$ ($K_1 > K_2 > K_3$).

A schematic depiction of the types of ellipsoids is shown in Figure 2.

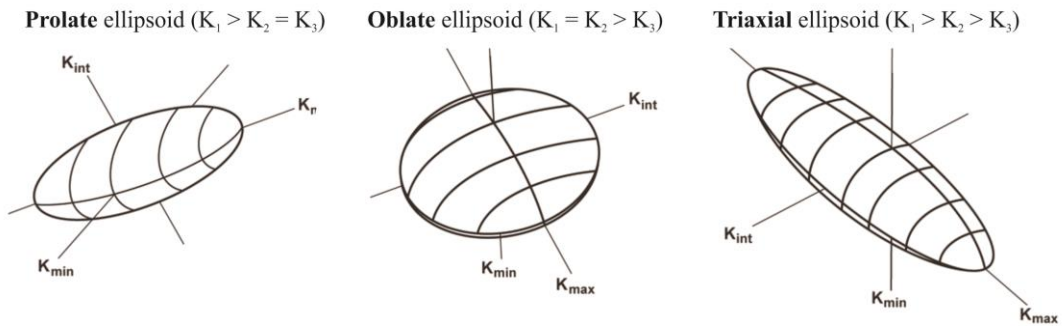


Figure 2 – Schematic depiction of prolate, oblate, and triaxial magnetic susceptibility ellipsoids. The three orthogonal axes correspond to the maximum (K_1), intermediate (K_2), and minimum (K_3) susceptibility values (adapted from Tarling and Hrouda, 1993)

II.1.3.2. Magnetic behaviors

Materials can be classified as diamagnetic, paramagnetic, or ferromagnetic depending on its response to an applied magnetic field. When a magnetic field is applied in a diamagnetic material, the resulting magnetization is opposite to the applied field. Thereby, a diamagnetic mineral has a negative magnetic susceptibility (K_d), proportional to the applied field (Figure 3). In the absence of the applied field, the magnetization disappears (Figure 4A). Calcite, quartz, feldspar, zircon, and apatite are examples of diamagnetic minerals.

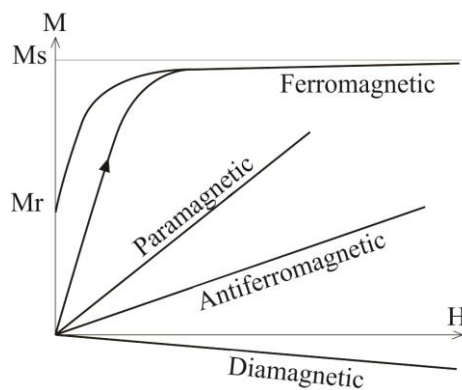


Figure 3 – Types of magnetic behavior in a material. Magnetization (M) as a function of the applied field (H) (Nédélec and Bouchez, 2015).

The disposition of magnetic moments in paramagnetic materials is statistically disordered (Figure 4B), resulting in null magnetization in the absence of an applied field. In an applied field, these moments tend to orientate parallel to the applied field. Consequently, the paramagnetic susceptibility (K_p) is positive (Figure 3), constant, and dependent on the

applied field. K_p decreases with the increase of temperature and this property is one of the criteria used to identify the paramagnetic contribution of minerals to the bulk susceptibility. In the paramagnetic minerals, the magnetocrystalline anisotropy is determined by the complexity of the mineral crystal lattice. Trigonal and orthorhombic crystal systems, such as serpentine and orthopyroxene, the crystallographic axes and main directions (K_1 , K_2 , and K_3) are coaxial. In the monoclinic system, as in the case of biotite and amphibole, only the crystallographic axis “b” is parallel to K_1 . However, the presence of metallic inclusions in the crystal lattice of minerals may result in an inconsistency between magnetic and crystallographic axes.

Crystalline materials in which iron ions strongly interact with each other creating a spontaneous magnetization have a behavior known as ferromagnetic “*lato sensu*” (s.l.) Ferromagnetism s.l. includes the ferromagnetism “*sensu strictu*” (s.s.), the ferrimagnetism, and the antiferromagnetism. In the presence of an external applied field, the magnetic moments of ferromagnetic s.l. materials are oriented parallel to the applied field. In the absence of an applied field, ferromagnetic materials still have a magnetization, which is described as remanent magnetization that results from the past applied fields that the material underwent through its magnetic history. This results in a positive (Figure 3) induced magnetization that increases until the saturation magnetization (M_s). This property to reach a saturation magnetization under high applied field and retain a remanent magnetization when no field is applied is illustrated by the hysteresis loop (Figure 6B).

Magnetic moments oriented in opposite directions (antiparallel) characterize antiferromagnetic materials (Figure 4D). In the absence of an applied field, there is a compensation of opposite magnetic moments and a resulting null magnetization. Under an applied field, antiferromagnetic materials behave similar to the ferromagnetic materials, however, with lower values of magnetic susceptibility (Figure 3).

Ferrimagnetic materials also have antiparallel interactions, but with different intensity values (Figure 4E). Opposite magnetic moments are not compensated and result in a spontaneous magnetization of lower values than ferromagnetic s.s. materials in the absence of an applied field (Figure 3).

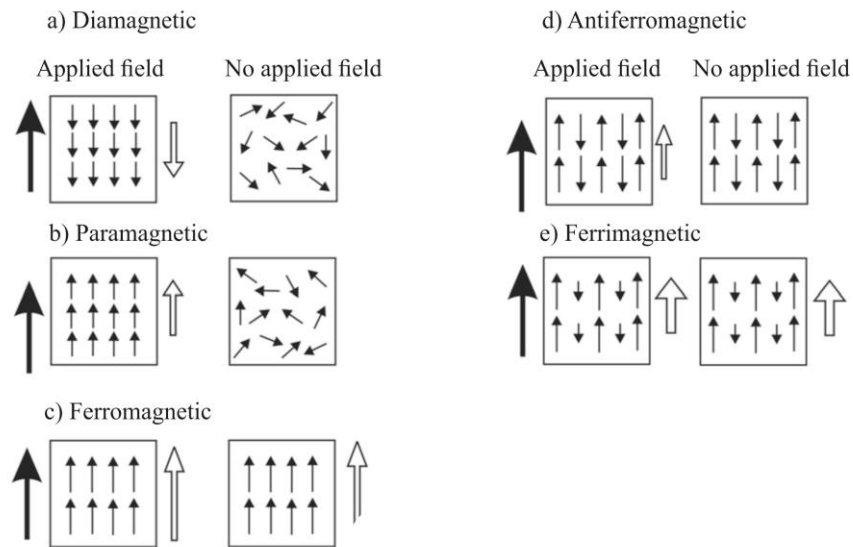


Figure 4 – Types of alignment of the magnetic moments. The diagrams of the left side from (a) to (e) show the magnetization (white arrow) that a material acquires when a magnetic field is applied (black arrow). The diagrams of the right side illustrate the magnetization after the applied field is removed (adapted from Tarling and Hrouda, 1993).

The magnetic moments become disorganized and behave paramagnetic-like when reaching the Curie Temperature (T_C) for ferromagnetic minerals, and the Néel Temperature (T_N) for antiferromagnetic minerals.

II.1.3.3. Magnetic domains

The determination of the magnetic domain status in ferromagnetic minerals is extremely important for AMS interpretations (Potter and Stephenson, 1988; Ferré, 2002; Guerrero-Suárez and Martín-Hernández, 2016). When a ferromagnetic s.l. mineral is magnetized, the distribution of the magnetic moments inside the grain is organized to reach a minimum magnetostatic energy state. This is achieved through the creation of areas where the magnetic moments have the same orientation (magnetic domains). The magnetic domain is an evenly magnetized volume that can be considered as a single oriented magnetic domain. The domains are separated by boundaries that can rearrange depending on the intensity of the applied field (Figure 5). Increasing the volume, the grain becomes energetically unstable and consequently, new magnetic domains are formed with their own magnetization orientations. Particles can be subdivided in multi-domain (MD), single-domain (SD), and pseudo-single domain (PSD). The behavior of coercivity (H_C), which is the magnetic field necessary to suppress remanent magnetization of a material, depends on the magnetic domains and grain-size (volume) (Figure 6A). H_C is maximum in the transition of MD-SD grains (dc). With an increase in grain size, the grain is subdivided into domains and H_C decreases. When grain size

decreases, H_C also decreases and becomes null in the transition (ds) to the superparamagnetic behavior, in which grains do not present remanence and their susceptibility is null in the absence of an applied field. A shift in the direction of magnetization occurs in the MD-SD transition. MD grains present a resulting magnetization parallel to the long axis of the grain (direction of where there is more material). Magnetic susceptibility in SD particles is higher in the axis perpendicular to the long axis of the crystal.

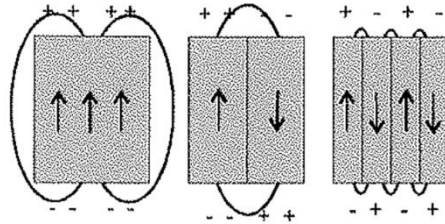


Figure 5 – Subdivision of a ferromagnetic grain in magnetic domains (modified from Hrouda, 1993).

The presence of MD or SD grains can be detected through the ratios M_r/M_s and H_r/H_c from a hysteresis loop (Figure 6B) (e.g. Archanjo, 2003; Lowrie, 1997; Nédélec and Bouchez, 2015; Putnis, 1992; Tarling and Hrouda, 1993). With the progressive increase of an applied field H , the magnetization increases until reaching saturation (M_s). When H decreases, the magnetization reduces but does not reach zero when H is completely removed. This residual magnetization is the remanent magnetization (M_r). To cancel M_r it is necessary to apply an external field in the opposite direction until the remanence is completely removed. The inverse field necessary to remove M_r is denominated coercivity ($-H_c$). When the sample is saturated in the opposite direction ($-M_s$), the hysteresis loop is completed. SD grains have ratio $M_r/M_s \geq 0.5$ and $H_r/H_c < 2$, while MD grains $M_r/M_s < 0.02$ and $H_r/H_c > 5$. The behavior of PSD grains is not well understood. It may be treated as MD particles with few internal domains and difficulties to isolate new domains, or coexistence of MD (low coercivity) and SD (high coercivity) grains in which this mixture would provide values of M_r/M_s H_r/H_c characteristic of PSD components.

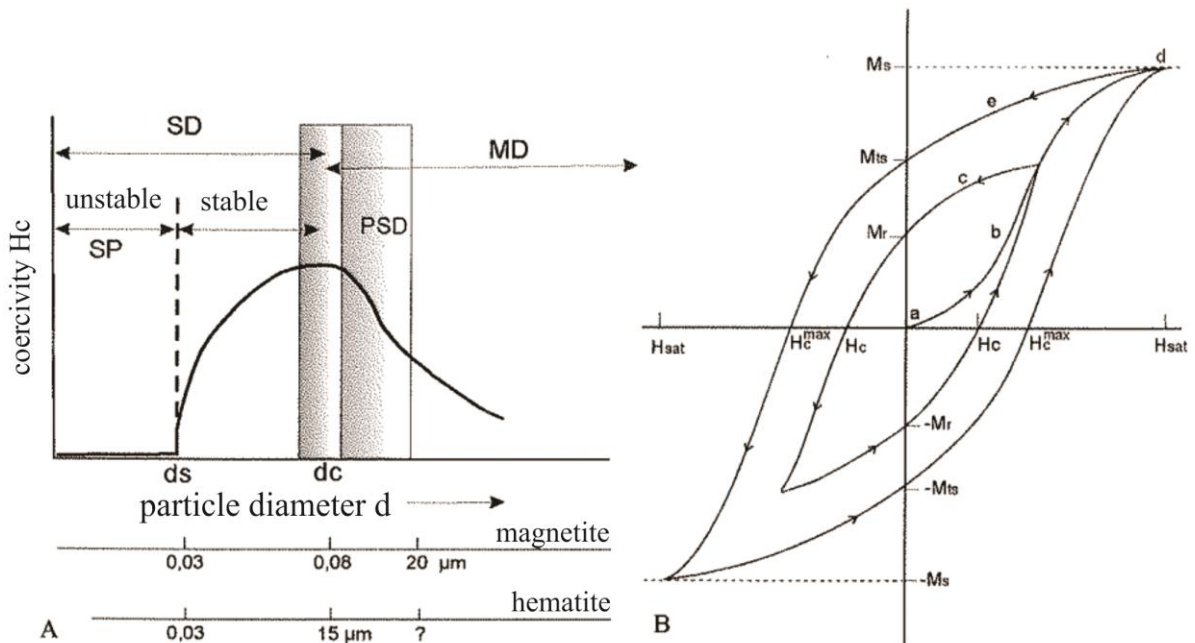


Figure 6 – A: Coercivity variation versus particle diameter. Multi-domain (MD), single-domain (SD), pseudo-single domain (PSD), and superparamagnetic (SP). d_c and d_s are critical diameters for particles MD-SD and SP, respectively. B: Hysteresis loop for ferromagnetic minerals s.l. H is the applied field; M_s the saturation magnetization; M_r the remanent magnetization; H_c refers to coercivity. a, b, c, d, and e correspond to the hysteresis loop trajectory (In: Borradaile and Henry (1997)).

II.1.3.4. The relation between magnetic fabric and petrofabric

Magnetic fabrics can be hosted by ferro-, ferri-, para-, or diamagnetic phases. However, as mentioned above, the magnetic susceptibility of diamagnetic materials is very low, and its influence can be disregarded from the bulk magnetic susceptibility. The AMS of a rock is then controlled by the shape anisotropy and magnetocrystalline anisotropy of the ferromagnetic and paramagnetic minerals.

Magnetite has a high susceptibility and it is characterized by its shape anisotropy since the magnetocrystalline anisotropy is negligible due to the isotropic crystalline structure of magnetite. In magnetite-bearing rocks, magnetic domains cause their magnetic susceptibility to be grain size dependent, with larger grains displaying greater susceptibilities. As grain size increases the magnetic domain state changes from SD to MD, passing through the PSD state. SD magnetite has an inverse magnetic fabric (Potter and Stephenson, 1988; Rochette et al., 1992) where the susceptibility axes are interchanged; however, this is not the case for MD or PSD magnetite (and/or paramagnetic phases biotite and amphibole) which leads to direct magnetic fabrics (Bouchez, 1997; Launeau and Cruden, 1998). MD or PSD magnetite particles are large enough for the AMS ellipsoid to correspond to the shape ellipsoid and can

be interpreted as consistent with the petrofabric. Coexistence of SD and MD magnetite particles within the rock might lead to intermediate fabrics (Stephenson et al., 1986; Hrouda and Ježek, 2017), affecting potential interpretations.

In pyrrhotite or hematite-bearing rocks, AMS is controlled by the magnetocrystalline anisotropy. Shape anisotropy is not determinant and the bulk AMS of the rock is a function of the preferred orientation of the crystallographic axes and particularly their alignment in the rock petrofabric (Rochette et al., 1992).

Paramagnetic rocks have similar characteristics of the pyrrhotite or hematite case. Biotite and amphibole are important minerals which have predominant magnetocrystalline anisotropy. During deformation, the “c” axis of biotite tend to parallel the pole of the flow plane (foliation), and “c” axis of amphibole tends to parallel the flow direction (lineation) (Hrouda, 1982). The AMS ellipsoid for biotite is consistent with the crystallographic fabric and with the petrofabric. In amphibole, K_3 is perpendicular to the “c” axis of the elongated prism (Figure 7). In this sense, the AMS ellipsoid is perpendicular to the lineation of the petrofabric. However, studies reveal that this is only valid for “pure” amphibole. Measurements in single amphibole crystals suggest that the maximum susceptibility is parallel to the crystallographic “c” axis, due to magnetite inclusions that have their long axis parallel to the elongated prism of amphibole. Therefore, the magnetic fabric of the magnetite grains is parallel to the petrofabric. A very few amounts of magnetite included in amphibole are sufficient to control the AMS ellipsoid of the amphibole, and the resulting magnetic fabric is generally compatible with the petrofabric.

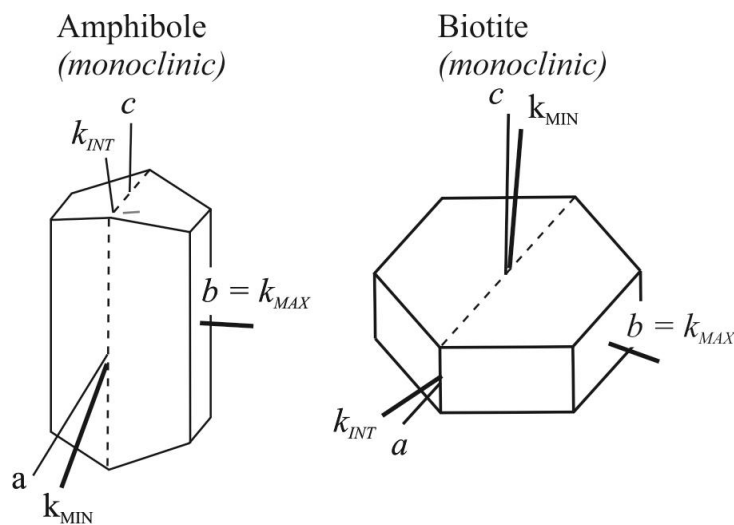


Figure 7 – Magnetocrystalline anisotropy in pure amphibole and biotite. (Source: Borradaile and Jackson, 2010).

II.1.3.5. Magnetic mineralogy investigations

Magnetic mineralogy investigations are necessary to determine the contribution of mineral phases to the magnetic susceptibility, in order to retrieve geological significance to the AMS result. The classification of the magnetic behavior, identification of the ferromagnetic mineral, grain size, and domain state determine the significance of the observed fabric.

Determination of the magnetic behavior is done through the acquisition of thermomagnetic curves (K-T curves) and hysteresis loops. Thermomagnetic curves are done through the measurement of the magnetic susceptibility in function of the temperature, while hysteresis loops are obtained through the induced magnetization in function of the applied field. These experiments allow the detection or not of ferromagnetic particles in the rock sample. If ferromagnetic minerals are not present, it is estimated that the AMS is carried by paramagnetic minerals and the anisotropy is magnetocrystalline. If ferromagnetic minerals are detected, isothermal remanence magnetization (IRM) curves are performed in order to identify which minerals are present. IRM curves are defined by the measurement of the remanent magnetization in function of the applied field. The next step consists in distinguishing the magnetic domain (MD, SD, or PSD) of the ferromagnetic particles and this can be achieved through the acquisition of First-order reversal curves (FORC), where the sample is subjected to a saturating field, as in most hysteresis experiments. The field is lowered, then increased again through some value to saturation. The magnetization curve between these field values is a FORC, and a series of FORCs are generated to the desired resolution. Finally, the anisotropy of anhysteretic remanent magnetization (AARM) provides the remanence ellipsoid of the ferromagnetic particles which can be used as a complement to AMS measurements to evaluate whether the ferromagnetic and the matrix fabrics are coaxial, isolating the contribution of remanence-bearing minerals from that of the paramagnetic and/or diamagnetic matrix.

II.1.3.6. Analytical method

In the present study, the low-field magnetic susceptibilities and its anisotropy were measured using a Kappabridge instrument (KLY-4S, Agico, Czech Republic) housed in the Paleomagnetism Laboratory of the University of São Paulo, Brazil. The AMS parameters were computed using Aniso software version 4.2 (Jelinek, 1978). Oriented samples were extracted using a portable gasoline-powered rock drill. Between 4 to 9 oriented cores were

drilled in each site. The cores were cut into cylindrical specimens with 2.5 cm in diameter and 2.2 cm in height, the standard for magnetic measurements. The specimens were named with a “TM” code. In addition, compiled data from previous studies (Portela, 2013; Sanchez, 2014, Pinto, 2015, codes BP, TFE, and TFN, respectively) were also utilized in the present study. The drilling and preparation procedures also obeyed the standards for AMS measurements.

Magnetic mineralogy investigations through the acquisition of thermomagnetic curves (K-T curves), hysteresis loops, isothermal remanent magnetization curves (IRM), and First-Order Reversal Curve (FORC) diagrams were performed on representative samples within the study area. The low-field thermomagnetic curves were measured at low- and high-temperature using powdered samples in an Ar atmosphere CS-3 apparatus coupled to the KLY-3 bridge instrument. Each sample was submitted to continuous heating and cooling cycles from -200°C up to 700°C using a CS-L cryostat and CS-4 furnace coupled to a Kappabridge KLY-4S susceptibility meter (Agico) hosted in the Paleomagnetic Laboratory at the Institute of Astronomy, Geophysics, and Atmospheric Sciences at the University of São Paulo (IAG-USP). Hysteresis loops, IRM acquisition curves, and FORC were measured at the Oceanographic Institute of the University of São Paulo (Geoprocessing Laboratory – LabGeo) using a MicroMag 3900 (Princeton Measurements Corporation) vibrating sample magnetometer (VSM) at room temperature. The applied fields for the three methods were up to 1T. FORC diagrams were generated using FORCinel (Harrison and Feinberg, 2008).

The AARM acquisition on standard cylinders also took place at the Paleomagnetism Laboratory hosted in the IAG-USP. Alternating field (AF) demagnetization and anhysteretic remanence acquisition were performed with a LDA-3A (Agico) demagnetizer/magnetizer and remanence was measured with JR6-A magnetometer (Agico). To obtain the AARM tensor, the magnitude and orientation of the principal axes were obtained using an eighteen position scheme with a peak field of 80 mT and a biasing field of 100 μ T. Before AARM measurements, samples were AF demagnetized at a peak field of 100 mT to establish a base level. AARM parameters were also computed using Aniso software version 4.2 (Jelinek, 1978).

II.1.4. U-Pb Zircon (LA-ICP-MS) Geochronology

Absolute age determinations serve for a variety of applications (e.g. Jackson et al. 2004) including geotectonic studies and dating of igneous rocks. The decay of a radioactive isotope in a natural mineral with a half-life favorable for the expected age of the material or

process is used for these determinations. Materials of considerable age (millions of years), suggest the usage of the radioactive uranium isotopes ^{235}U and ^{238}U with half-lives of 7.04×10^8 and 4.47×10^9 years, and the radiogenic daughter isotopes ^{207}Pb and ^{206}Pb , respectively. This isotopic decay system and analysis of the parent and daughter isotopes allow the determination of the crystallization age of the mineral. The analyzed mineral should show high resistance to chemical exchange and recrystallization, and high contents of U and Pb. Zircon is a mineral that meet these requirements, and it is, therefore, widely used in geochronological studies.

The ratios between the stable decay products and the radioactive parent isotopes ($^{206}\text{Pb}/^{238}\text{U}$ and $^{207}\text{Pb}/^{235}\text{U}$) are interrelated in the U-Pb decay system. Works of Ahrens (1955) and Wetherill (1956) define the “concordia curve” (Figure 8), in which under closed-system conditions, the curve extends from today towards the formation of the Earth and the solar system at approximately 4.53 Ga, following these ratios. The ratios have to concord one to another following the relationship:

$$\frac{^{206}\text{Pb}}{^{238}\text{U}} = \left(\frac{^{207}\text{Pb}}{^{238}\text{U}} + 1 \right)^{\lambda^{238}\text{U}/\lambda^{235}\text{U}}$$

with λ being the decay constant of the respective radioactive isotope. Another age information can be obtained by the $^{207}\text{Pb}/^{206}\text{Pb}$, based on the relationship:

$$\frac{^{207}\text{Pb}}{^{206}\text{Pb}} = \frac{^{235}\text{U}}{^{238}\text{U}} \times \frac{e^{\lambda^{235}\text{U} \times t} - 1}{e^{\lambda^{238}\text{U} \times t} - 1}$$

With the constant present-day $^{238}\text{U}/^{235}\text{U}$ ratio (137.88) this age considers only the radiogenic isotope. Hence, the more accurate and valid age information is obtained from the $^{206}\text{Pb}/^{238}\text{U}$ and $^{207}\text{Pb}/^{235}\text{U}$ isotope ratios.

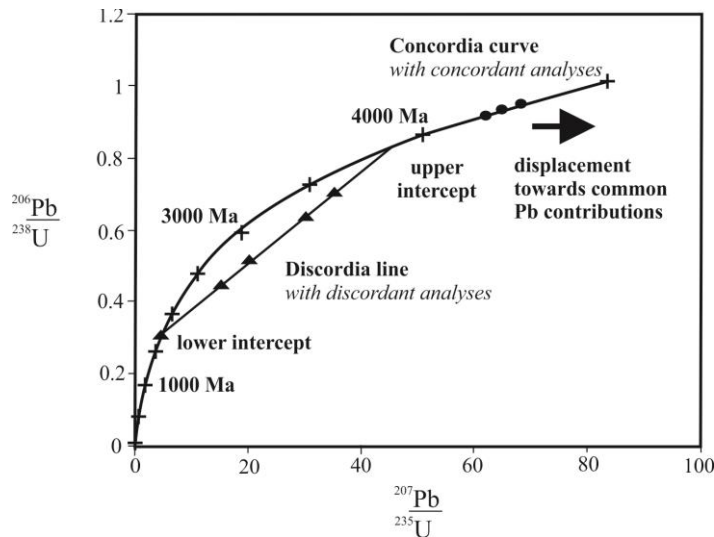


Figure 8 – Concordia diagram $^{207}\text{Pb}/^{235}\text{U}$ versus $^{206}\text{Pb}/^{238}\text{U}$. Concordant analyses are displayed in the concordia curve. Lead loss plot in the discordia line, intersecting an upper and a lower intercept. Common Pb to the bulk Pb content plot below the Concordia diagram (Bühn et al., 2009).

The system must have been closed to the gain or loss of the parent or daughter isotopes (Faure and Mensing, 2005). In some cases, the loss of radiogenic Pb can result in “discordant” isotopic analyses, where the analytical points do not coincide with the concordia curve in the $^{206}\text{Pb}/^{238}\text{U}$ versus $^{207}\text{Pb}/^{235}\text{U}$. The discordia line intersects the concordia curve twice, providing an upper and a lower intercept. The upper intercept generally represents the crystallization age of the mineral, while the lower may represent the age of the event that has caused the loss of radiogenic Pb. Another problem with this method is that the material analyzed may contain common Pb of non-radiogenic origin and, in order to avoid correction procedures, it is always more adequate use minerals that contain sufficient U to analyse and the daughter isotope, and that do not accommodate common Pb in its crystal lattice. These are, for example, zircon or monazite.

II.1.4.1. Analytical method

The samples collected in the field for age determinations were prepared in Geochronology Research Center at the University of São Paulo (CPGeo-USP), according to the standard procedure of the laboratory. First, the samples are crushed and pulverized in a disk mill. The pulverized sample is then hydraulically processed with a Wiffley table, which consists of a slightly inclined vibrating table that receives a constant water flow. The heavier minerals are drained through the upper channels of the table, while the lighter minerals follow the lower ones. Two collectors arranged properly on the side of the table collect the heavier grains and the lighter grains, which are then dried under an incandescent bulb. The heavier

minerals are then submitted to separation of magnetic and non-magnetic fractions using a hand magnet, and an electromagnetic device (Frantz) configured to separate the material under a current of 0.4 A. The zircon grains are in the non-magnetic fraction. This fraction is then inserted in heavy liquids (methylene iodide and bromoform) in order to separate dense grains (such as zircon) from the bulk lighter grains (such as quartz and feldspar). Finally, zircons from the heavy minerals fraction are handpicked under a microscope. The selected crystals are mounted in an epoxy disk and polished.

The analyses of the U-Th-Pb contents of the zircons were conducted at the Geochronology Laboratory at the University of Brasília (UnB, Brazil), using a Finnigan Neptune couple with a Nd-YAG laser ablation system. The abundances of U, Th, and Pb, and the Pb isotopic ratios were normalized using the GJ-1 zircon standard (608.5 ± 1.5 Ma; Jackson et al., 2004). More details on the instrumental operation procedures are described in Bühn et al. (2009). The data was then reduced using a spreadsheet known as Chronus (Oliveira et al., 2015), and the statistical assessments were calculated using Isoplot/Excel 3.0 (Ludwig, 2003). Finally, selected zircon grains were imaged using back-scattered electron (BSE) using a scanning electron microscope, housed at UnB.

CHAPTER III

III.1. GEOLOGICAL BACKGROUND

III.1.1. The Western Gondwana

The orogenic belts of Brazil were generated mainly during the amalgamation of Western Gondwana in the Neoproterozoic and early Paleozoic (640-520 Ma) with the accretion of fragments derived from the supercontinent Rodinia, forming a complex crustal mosaic (Trompette, 1994; Brito-Neves et al., 1999; Almeida et al., 2000). These fragments represent continental Archean and Paleoproterozoic blocks and constitute the different cratons of Brazil and western Africa. The collision and closure of basins that generated this mosaic are the Brasiliano orogeny of Brazil and Pan-African orogeny of Africa. Currently, the term Pan-African orogeny is used specifically to qualify the orogenic belts resulting from the collision between blocks that resulted in the South American and African continents (between 680 Ma and 550 Ma). Brasiliano orogeny is a term that refers to the orogenic belts located in Brazil.

In the context of the Western Gondwana amalgamation, the Brasiliano / Pan-African domains can be related as the result of the assemblage, collision, and adjustment of continental masses or cratons, such as: São Francisco-Congo, Rio de la Plata, Amazonian, West African, Tanzania, and Kalahari (Alkmim et al., 2006). The different collisions resulted in a complex setting of orogenic belts marginal to the cratons (Figure 9).

Numerous orogenic belts were identified and studied, which allowed Trompette (1997) to group them into six major mega-belts. Four are sub-meridional to the current North, while the other two are approximately E-W, sub-perpendicular to the previous ones. The sub-meridional Brasiliano / Pan-African orogenic mega-belts are the Trans-Saharan mega-belt, thrusting the West African craton; the Brasilia mega-belt, thrusting over the São Francisco Craton; the South African mega-belt containing the Araçuaí, Western Congo, Ribeira, and Kaoko belts, forming its northern portion, and the southern portions comprising the Gariep, Malmesbury, and Dom Feliciano belts, which thrust upon the Kalahari and Rio de la Plata cratons; and the West African-South American mega-belt comprised of the Bassaride, Rokelide, Araguaia, Paraguay, and Pampean Ranges developed on the west portion of the Western Gondwana supercontinent. The other two sub-perpendicular mega-belts are: Oubanguide-Sergipe thrust upon the São Francisco craton and the Damara orogen thrusting

the Kalahari craton. The chronology and amalgamation of Western Gondwana are still under debate, however, the characterization of these belts has allowed several researchers to develop different evolutionary models for this portion of the supercontinent (Brito-Neves and Cordani, 1991; Trompette 1994; Noce et al. 2000; Cordani et al., 2003).

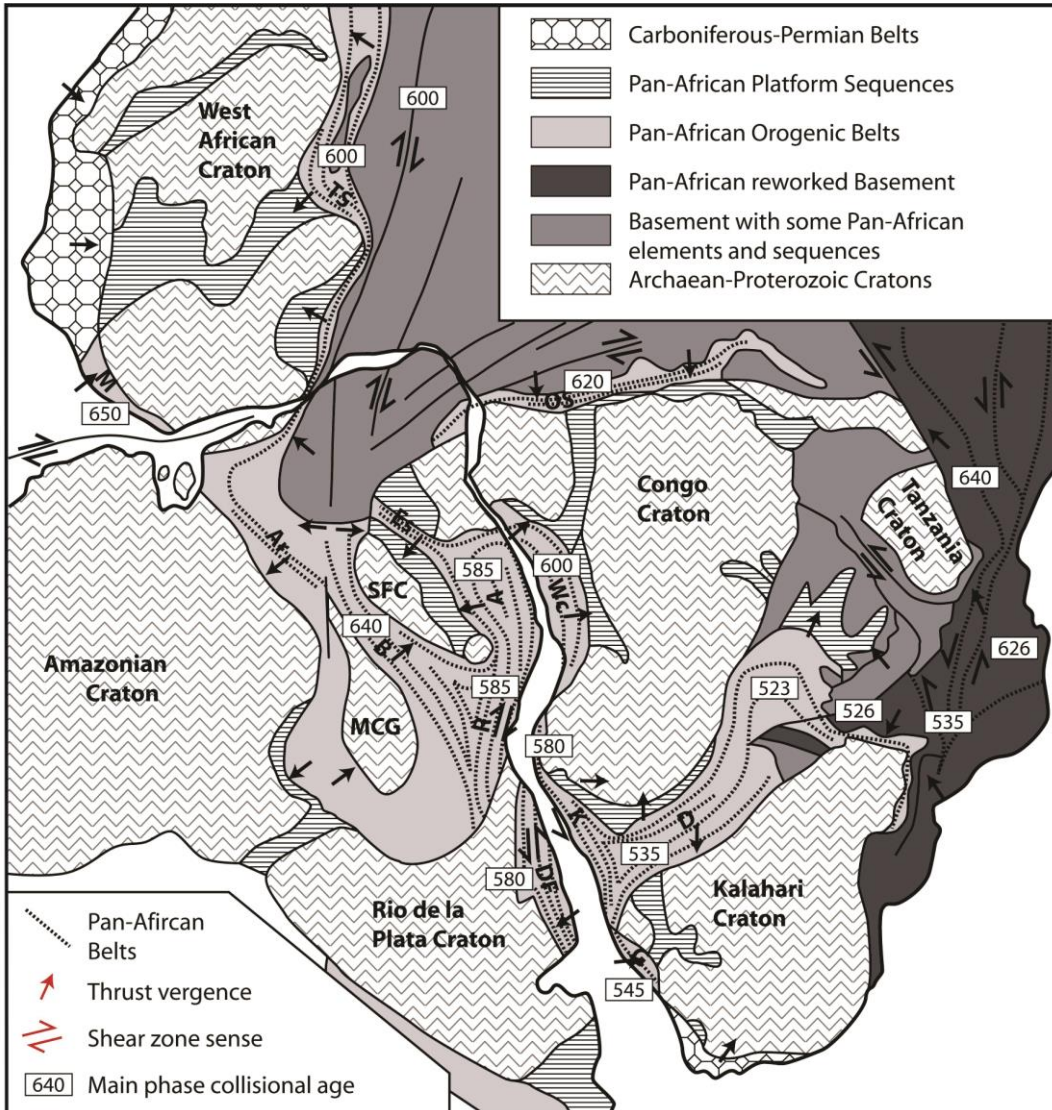


Figure 9 – Location of the Araçuaí and Ribeira belts (letters “A” and “R”, respectively) within the regional context of the Neoproterozoic-Cambrian Pan-African Orogenic System in West Gondwana (Goscombe and Gray, 2008).

At the end of the agglutination of West Gondwana, the Ribeira-Araçuaí belt, the São Francisco craton, and the western portion of the Congo craton occupied the central part of a newly formed continent. The Ribeira-Araçuaí belt represents a product of the amalgamation of these cratons during the Neoproterozoic, and it extends continuously in the east and south-east edges of the São Francisco craton (Figure 9). The West Congo belt is the eastbound

counterpart inherited by Africa after the opening of the South Atlantic Ocean in the Cretaceous.

III.1.2. The Ribeira-Araçuaí Orogenic System

The Mantiqueira Province, as defined by Almeida (1977), is the orogenic system along the Brazilian coast that extends from the southern border of the eastern São Francisco craton (16°S) to Uruguay (33°S). It constitutes a more than 3000 km long NNE-trending Neoproterozoic orogenic system that recorded the protracted sequence of orogenic events associated to the West Gondwana amalgamation and comprises in its northern portion, the Ribeira and Araçuaí orogens (Figure 10).

The Ribeira-Araçuaí belt (Figure 10), from North to South, is characterized by a change in the pattern of deformation regime (Figure 11A) and with the advancement of the investigations, the limit of the belts began to be discussed based on correlation and continuity of lithostratigraphic units, structural patterns, and geophysics (e.g., Egydio Silva and Vauchez, 2011). The structural pattern of the Ribeira belt is of dextral transcurrent zones parallel to the orogen (Trompette, 1994; Egydio-Silva et al., 2002), whereas in the northern portion it is represented by the Araçuaí belt, where the structural pattern is characterized by contractional tectonics (Figure 11B), with thrusting towards the São Francisco craton (Oliveira et al., 2000; Cunningham et al., 1998; Egydio-Silva, et al., 2005). This distinction led to the separation of the belts in Ribeira and Araçuaí belts. The E-W convergence between the São Francisco and Congo cratons is NE-SW oriented in the Ribeira belt (oblique), while in the Araçuaí belt it is approximately orthogonal (Vauchez et al., 1994; Egydio Silva et al., 2002). However, this variation is interpreted as a reflex of the rigid termination of the southern portion of the São Francisco craton. Consequently, the Ribeira and Araçuaí belts are attributed to the same orogenic system.

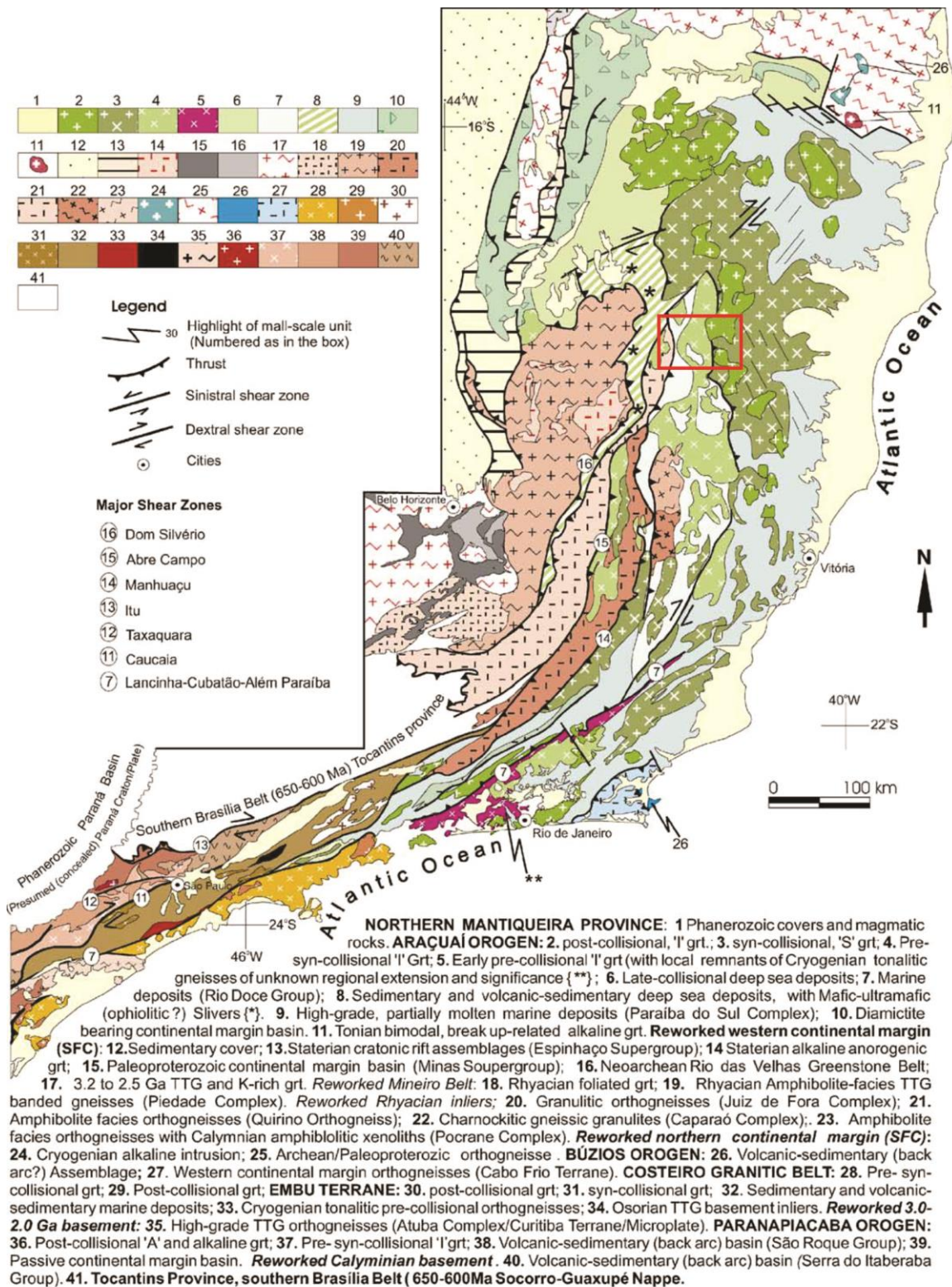


Figure 10 – Geological map of the northern Mantiqueira Province, highlighting the Ribeira and Araçuaí orogens (Source: Silva et al., 2005). The red box represents the studied area.

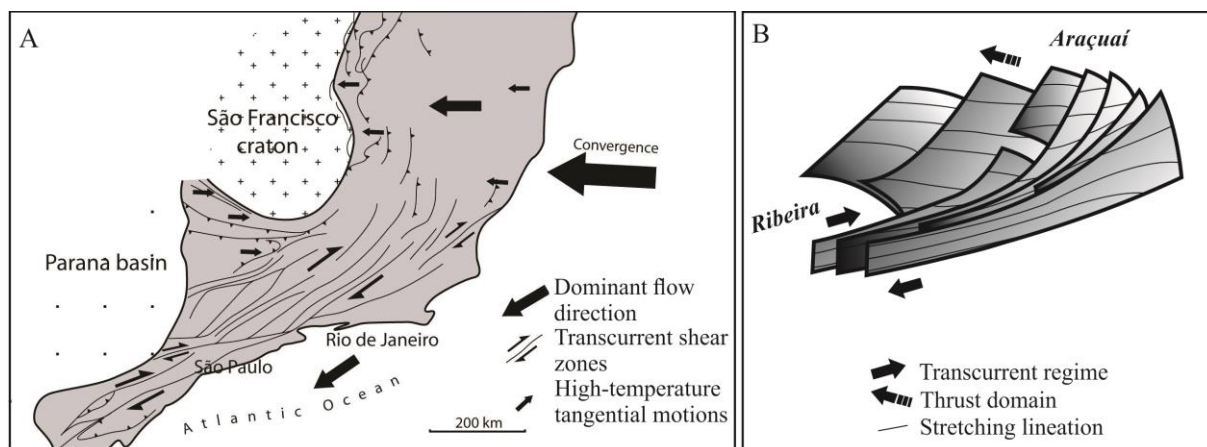


Figure 11 – Schematic structural map of the Ribeira-Araçuaí orogenic system (A) showing the variations of the structures from south to north (from Mondou 2012, adapted from Vauchez et al 1994). A schematic illustration (B) of how the structural style and kinematics vary along with the transition between the Ribeira and Araçuaí belts (Vauchez et al., 1994; Egydio-Silva et al., 2005).

Uhlein (1991), Pedrosa-Soares and Noce (1998), Pedrosa-Soares and Weidemann-Leonardos (2000), Pedrosa-Soares et al. (2001), and Alkmim et al. (2006) contributed to the elaboration of the concept of Araçuaí-Western Congo orogen, describing several geotectonic components that reinforce the proposition that this orogen evolved from the closing of an oceanized basin with the formation of a magmatic arc (Pedrosa-Soares et al., 1992, 1998). However, the presence of this ocean between the San Francisco and Congo cratons is under debate (Cavalcante et al., 2019). The presence of marine deposits and a probable representative unit of a typical metavulcanosedimentary rock of the ocean floor found in the northern portion of the Araçuaí belt and dated to ~850 Ma (Pedrosa-Soares et al., 1998) are observations that support the hypothesis. However, no oceanic remnants were observed in the southern portion, represented by the Ribeira belt, despite the occurrence of Mid-Ocean Ridge Basalts (MORB) magmatism dating to ~850 Ma. Mafic dykes support that this ocean formed due to the displacement of Rodinia (~900Ma) (Djama et al., 1992). Pedrosa-Soares et al. (1992), Pedrosa-Soares et al. (1998) and Uhlein et al. (1998) describe a stage of continental rift evidenced by Neoproterozoic deposits of the pre-collision basins, even though evidence of oceanic spread is not so clear. This ocean opening is probably related to the Paramirim Aulacogen (~850 Ma), suggested in Cruz and Alkmim (2006), which separates the São Francisco craton into northern and southern lobes. This aulacogen accommodated extensional forces and formed the Macaúbas rift system, described as the precursor basin of the Araçuaí-Western Congo orogen.

The convergence between the São Francisco and Congo cratons would mark the development of the magmatic arc, reflecting active subduction and demonstrated by rocks of the calcium-alkaline series at ~790 Ma, ~635-620 Ma and ~625-575 Ma (Heilbron and Machado, 2003; Pedrosa-Soares et al., 2001). However, even if there is evidence of the break-up of Rodinia, the fact that there is no obvious identification of oceanic crust in the northern portion of the Ribeira belt and in the southern portion of the Araçuaí belt causes the subduction hypothesis to be considered with caution. The Paramirim Aulacogen indicates that the rift was aborted in the northern portion of the San Francisco craton and this suggests that a more southern oceanic spread occurred, resulting in an extension not large enough to initiate subduction and generate a magmatic arc during the convergence between the cratons (Mondou, 2010; Cavalcante et al., 2019).

The construction of the magmatic arc lasts from ca. 630 Ma to 580 Ma (Silva et al., 2005; Alkmim et al., 2006) in both the northern and southern segments of the Ribeira and Araçuaí belts. At this stage, crustal thickening occurs due to the insertion of a large volume of magmatic rocks, deformation, and metamorphism of the sediments of the Macaúbas basin and inversion of the Paramirim Aulacogen.

Several studies suggest that the final stage of evolution would be marked by lateral escape followed by a gravitational collapse of the Ribeira-Araçuaí orogen, a process that is recorded by normal shear zones and the generation of large volume of post-collisional granites (Noce et al., 2000). The exhumation of the Ribeira-Araçuaí belt is lacking inquiries; no associated tectonic event is described in the literature and the phase of orogenic collapse is doubtful to consider as a factor of exhumation. Vauchez et al. (2007) and Petitgard et al. (2009) suggest that the Araçuaí orogen had a slow cooling rate, a low exhumation rate, and probably there was no collapse.

II.1.3. The Araçuaí Orogenic Belt

The Araçuaí belt represents the northern segment (Figure 10) of the Mantiqueira Province (Almeida et al., 1977, 1981; Heilbron et al., 2004) and refers to the region adjacent to the south and southeast edges of the São Francisco craton in Minas Gerais and neighboring regions of Bahia, extending to the Atlantic coast, approximately between the parallels 15° and 21° S (Figure 12). The northern border describes a curvature, defined by the São Francisco craton. The southern boundary is marked by the structural trend of NE direction of the Ribeira

belt that undergoes inflection for NNE to NS to the north (Pedrosa-Soares and Weidemann-Leonardos, 2000).

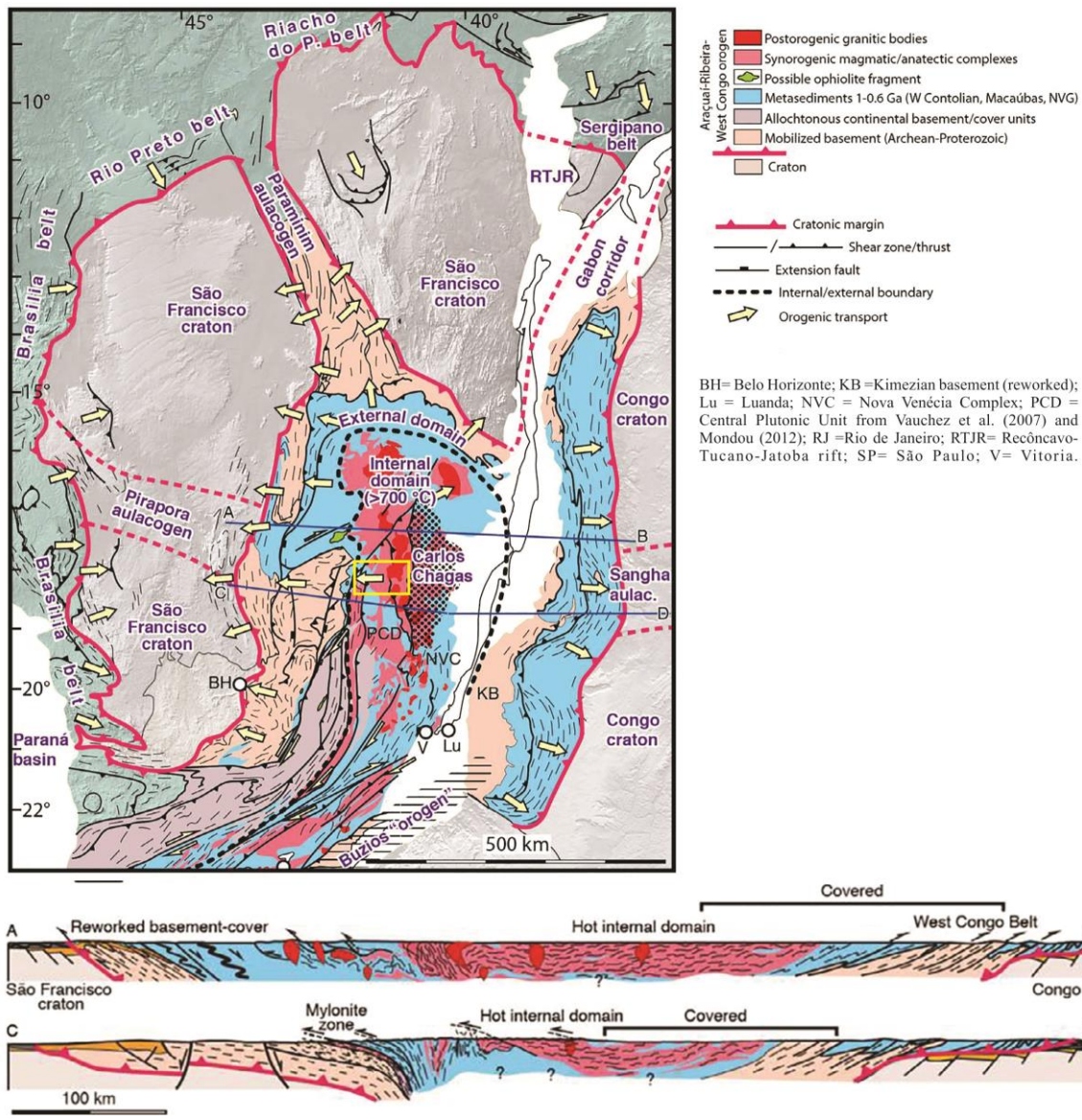


Figure 12 – Simplified geological map of the Araçuaí belt of the Araçuaí-West Congo and northern Ribeira orogen. Yellow arrows represent kinematics during main/late stages of orogeny. Based on maps from “Projeto Leste” and Tack et al. (2001). Cross-sections are based on Tack et al. (2001), Alkmim et al. (2006), and Vauchez et al (2007). Dotted area indicates the Carlos Chagas (Eastern Anatectic Unit) anatectic domain (Source: Cavalcante et al., 2019). The yellow box represents the location of the studied area.

II.1.3.1. Tectonic and structural framework

The compartmentalization of the Araçuaí orogen consists of several structural domains, which differ in terms of style, orientation, and deformation. Two domains are described by some authors: an external domain and an internal domain (Siga-Júnior, 1986; Pedrosa-Soares and Weidemann-Leonardos, 2000; Pedrosa-Soares et al., 2001). The external

domain corresponds to the western portion and is characterized by west-verging thrusts and folds that fringes the eastern edge of the São Francisco craton and low-grade metamorphism, from greenschist facies to the transition between the greenschist and amphibolite facies, from west to east. The eastern internal domain contains high-grade metamorphic rocks and extensive orogenic plutonism. The tectonic vergence of the inner domain is generally to the west, but vergence to the east is also observed.

Another proposal of compartmentalization, based on kinematic analysis, spatial orientation and nucleation of dominant structures is found in Alkmim et al. (2006), which subdivided the orogen into ten tectonic compartments, highlighting the external domain.

Oliveira et al. (2000) and Vauchez et al. (2007) prioritize descriptive terms to compartmentalize the orogen (Figure 13), being subdivided into para-autochthonous metasedimentary cover of the São Francisco craton, corresponding to the external domain, and on a stacking of allochthonous units, representative of the internal domain. The allochthonous domains are: the eastern domain or anatectic unit (EAU), which constitutes a thick layer (>10 km) of diatexites and anatectic granites representing a partially molten middle crust, which is topped by migmatitic kinzigites; the central domain or plutonic unit (CPU), comprised of pre- to syn-collisional magmatic bodies intruded in high-temperature metasediments; and the western domain or mylonitic unit (WMU), involving metasedimentary and meta-igneous mylonites thrust upon the para-autochthonous metasedimentary cover of São Francisco craton. A late generation of porphyritic granitoids associated with charnockites intruded the stack of allochthonous units.

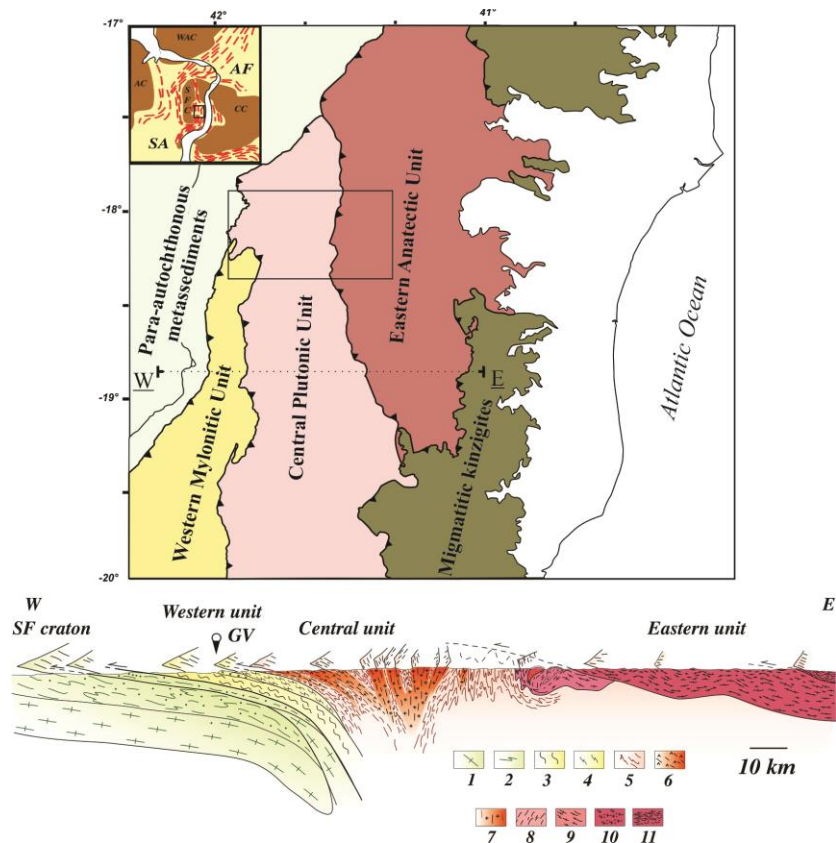


Figure 13 – Schematic map (modified from Oliveira et al., 2000 and Vauchez et al., 2007) and cross-section showing the four main domains of the Araçuaí belt. The Eastern Anatectic domain thrust upon the Central and Western Mylonitic units, directly onto the para-autochthonous metasedimentary cover of the São Francisco craton. From W to E: the granulitic (1) and metasedimentary (2) of the São Francisco craton; the western domain involving metasedimentary (3) and tonalitic mylonites (4); the central domain composed of metasedimentary (5) and pre- to syn-collisional intrusives São Vitor tonalite (6) and Galileia batholith (7); the eastern domain comprises a thick layer of anatexites (9) and anatectic granites representing the partially molten middle crust, with minor metasediments (8) intruded by syn- to late-granitoids (10). The black box represents the studied area and dashed line the cross-section “W-E” by Vauchez et al. (2007).

II.1.3.2. Lithological units

The lithological units of the Araçuaí orogenic belt will be presented in this section, highlighting the main rock types inserted in the study area of this present work (Figure 14). The study region includes part of the Central Plutonic Unit (CPU), and parts the Para-autochthonous sedimentary cover, Western Mylonitic Unit (WMU), and Eastern Anatectic Unit (EAU).

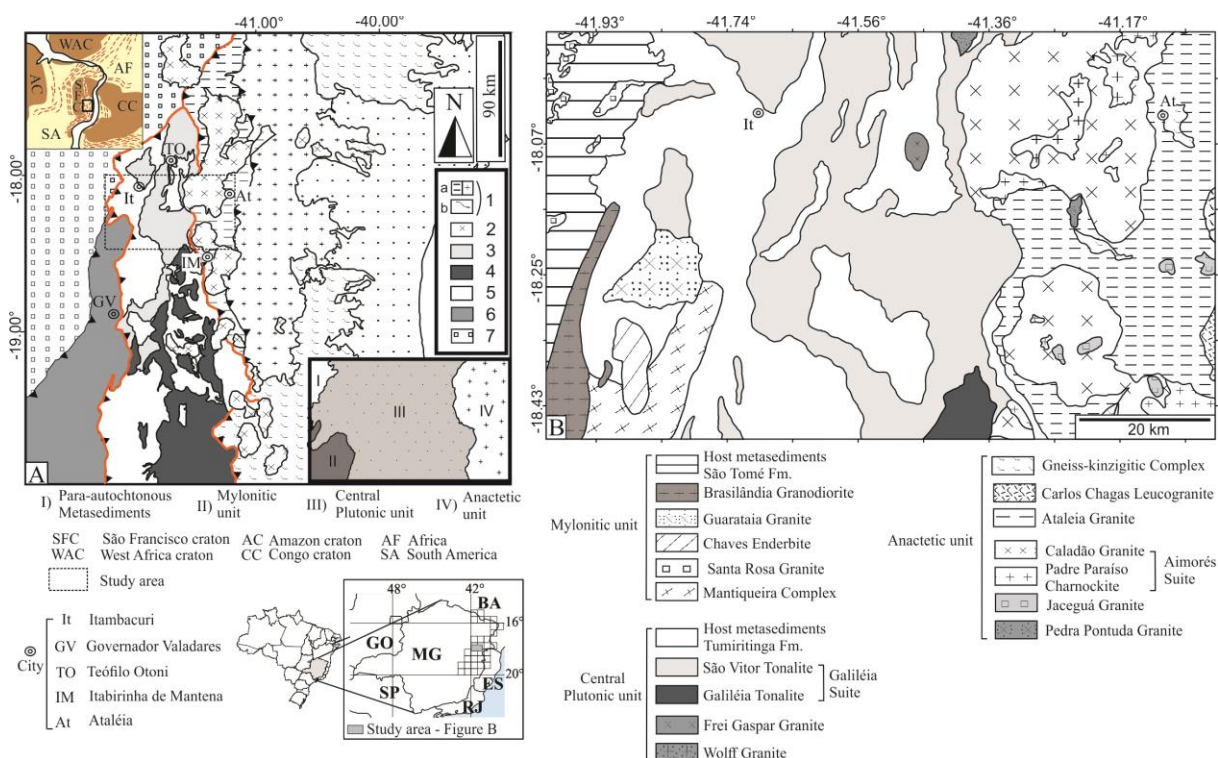


Figure 14 - A: Simplified map of the Araçuaí belt (after Vauchez et al., 2007) showing its main tectonic domains: (1) thick (> 10 km) layer of diatexites, metatexites, and anatectic granites (a) associated with migmatitic granulites and migmatitic kinzigite (b) intruded by late orogenic porphyritic granitoids associated with charnockites (2) characterizing the Eastern Anatectic Unit. The Central Plutonic Unit comprises the São Vitor Tonalite (3) and (4) Galiléia batholith intruding (5) high-T metasedimentary rocks. Metasedimentary and meta-igneous mylonites from the Mylonitic Unit (6) thrust upon the para-autochthonous metasedimentary cover of the São Francisco craton (7). The orange line separates the limit between lithological domains, showed in the inset box. The dashed box shows the location of the study area, detailed in B. B: Schematic geological map showing the various rock types in the studied region (adapted from Oliveira et al., 2000 and Tedeschi, 2013).

II.1.3.2.1. The Basement

Along the western portion of the Araçuaí belt, the basement units are essentially composed of metamorphic complexes, granitoids, and supracrustal units (Noce et al. 2007a; Alkmim et al., 2006) of Archaean and Paleoproterozoic ages (Figure 10, #14 to 19). These units have been affected by the c.a. 2.2-2.0 Ga Trasamazonian orogeny, and later reworked by the Brasiliano orogeny (Figueiredo and Teixeira, 1996; Alkmim and Marshak, 1998; Noce et al., 1998, 2000). In the central portion of the Araçuaí belt, high-grade amphibolite facies orthogneiss and granulitic rocks associated with magmatic protoliths of Paleoproterozoic age (2.2-2.0 Ga) are interpreted as segments of the Transamazonian orogen reworked within the Araçuaí belt (Figueiredo and Teixeira, 1996; Alkmim and Marshak, 1998) (Figure 10, #20 and 21).

Signorelli (2000) describes the basement rocks of the studied region (Figures 14B and 15A to C) and classifies them as belonging to the Mantiqueira Complex, hosted in the WMU.

The author describes migmatitic gneiss of tonalitic to granitic composition. Signorelli (2000) and Tedeschi (2013) mapped these units in the western portion of the study region. The basement unit is comprised of medium to coarse-grained banded migmatitic gneiss. Garnet, amphibole, and biotite constitute the dark bands, while a quartzo-feldspathic association characterizes the lighter bands, of tonalitic to granitic composition. Portions that are more migmatized show a neosome represented by a quartzo feldspathic association with amphibole and a paleosome by amphibole-biotite gneiss. Thin section studies show that composition varies from tonalitic to granitic, the texture is granoblastic to porphyroclastic, and structures are described as protomylonitic to mylonitic (Signorelli, 2000). U-Pb in zircon yielded a crystallization age of 2110 ± 12 Ma (appendix B) for this complex (Tedeschi, 2013). Noce et al. (2007b) attribute that the rocks of the Mantiqueira Complex were generated as a result of a continental magmatic arc in the eastern border of the São Francisco craton, formed due to partial melting of archaean material (Figueiredo and Teixeira, 1996; Fischel et al., 1998).



Figure 15 – Outcrops of the Mantiqueira Complex in the studied area. A: migmatitic gneiss showing dark bands of biotite and amphibole and lighter bands represented by quartzo-feldspathic association. B and C: migmatite showing gneissic foliation that is associated with melt extraction texture and schollen structure represented by large blocks of melanosome.

II.1.3.2.2. Paleo/Mesoproterozoic Rift Assemblage

The Espinhaço Supergroup (Figure 10, #13) outcrops in the external portion of the fold-thrust belt in the western margin of the Araçuaí Orogen, and also in the Paramirim Aulacogen (Alkmim et al., 2006). The Espinhaço stage represents a rift around 1.75 Ga (Brito-Neves et al., 1996), comprising volcano-sedimentary and sedimentary sequences, deposited in a continental rift basin c.a. 1.75 Ga (Brito-Neves et al., 1996; Machado et al., 1989; Dussin and Dussin, 1995; Uhlein et al 1998; Martins-Neto, 2000).

II.1.3.2.3. Basin Material

The Macaúbas Group outcrops in the western portion of the Araçuaí belt (Figure 10, #6 to 10), and it characterizes an important continental margin depositional assemblage. At the western edge of the belt, the basal portion of the proximal deposition is characterized by metasandstones and metarkoses with metaconglomerate lenses of fluvial environment. These rocks record the beginning of the rifting stage (Noce et al., 1997; Pedrosa-Soares et al., 2000). The maximum age of sedimentation is c.a. 900 Ma (U-Pb SHRIMP, Babinski et al., 2007), indicated by detrital zircon grains of metasandstones. Evidence of glaciation is observed in the other formations of the proximal Macaúbas Group (Noce et al., 1997; Uhlein et al., 2007; Pedrosa-Soares et al., 2008), associated to tilités, metadiamicctites, iron formations, and subordinate metasandstones and metapelitic rocks. A transition from rift to passive margin is marked by the distal sedimentation of diamicctites, orthoconglomerates, and turbidites, together with mafic volcanism characterized by basalts that present transitional geochemical signature and inherited zircons of ages ranging from 1.1 to 2.7 Ga (Gradim et al., 2005; Babinski et al., 2005). Sandstones and pelitic rocks (Martins-Neto, 2000) characterize the platform sequence and represent the proximal sedimentation of the passive margin setting (Pedrosa-Soares et al., 2008). Pedrosa-Soares et al. (2000) provide the maximum sedimentation age for this platform sequence which yields c.a. 864 Ma (U-Pb SHRIMP in detrital zircons). The distal sedimentation of the passive margin is described as turbidites with calcareous lenses and marlstones. In addition, this sequence is associated to ophiolitic meta-ultramafic and meta-mafic rocks, in which petrographic, geochemical, and isotopic characteristics suggest that it records the generation of oceanic lithosphere (Pedrosa-Soares et al., 1998, 2008; Queiroga et al., 2006). Pedrosa-Soares et al. (1998) show that magmatic protoliths of amphibolites crystallized about ca. 816 Ma (Sm-Nd whole rock isochron). The temporal evolution of this basin is marked by the rift stage magmatism of the mafic dykes of the Pedro Lessa Suite (c.a. 906 Ma, U-Pb TIMS in zircon and baddeleyite, Machado et al., 1989), anorogenic plutonism of the Salto da Divisa Suite (c.a. 875 Ma, U-Pb SHRIMP in zircon, Silva et al., 2008), and plagiogranites associated to the mafic/ultra-mafic rocks of oceanic lithosphere signature, that yielded a crystallization age of ca. 660 Ma (Queiroga et al., 2007), which constrains the timing of oceanic crust generation.

In the central portion of the Araçuaí belt, distal units are represented by a large set of formations. These formations are the main host rocks of the plutons that emplaced subsequently. The Salinas Formation comprises sediments that represent shallow platform

deposition in a syn-orogenic context (Figure 10, #6 and 8), or next to a magmatic arc. U-Pb SHRIMP in detrital zircons of graywacke samples indicate maximum sedimentation age of ca. 568 Ma (Lima et al., 2002). This formation also contains mafic-ultramafic plutonics, tholeiitic amphibolites, metamorphosed deep-sea pelite, banded iron formation and ocean-floor basalt (Pedrosa-Soares et al., 2001). The Jequitinhonha and Paraíba do Sul complexes (Figure 10, #9) are composed of high-grade partially molten marine deposits (Seidensticker and Wiedmann, 1992; Faria, 1997; Pedrosa-Soares et al., 2001). Rocks of the Rio Doce Group (Figure 10, #7) host magmatic units in the study area. It is characterized by a metavolcano-sedimentary succession that encompasses the supracrustal rocks of the Rio Doce magmatic arc (Vieira, 2007; Tedeschi et al., 2016; Novo et al., 2018). The metasedimentary rocks represented by the Rio Doce Group comprises four formations (from base to top): Palmital do Sul, Tumiritinga, São Tomé, and João Pinto. The Palmital do Sul and Tumiritinga formations mostly include pelitic schists to paragneisses, interbedded with metavolcanic and meta-volcaniclastic rocks. The São Tomé Formation is characterized by psammitic to pelitic meta-turbidites with lenses of calc-silicate rocks. The João Pinto Formation includes sandstones. The magmatic crystallization ages of ca. 595 and ca. 584 Ma were obtained for the volcanic protoliths (U-Pb on zircon). The Tumiritinga and São Tomé formations are the metasedimentary rocks present in the studied area, the former included in the CPU and WMU, while the latter covers the para-autochthonous metasedimentary cover of the São Francisco Craton (Vauchez et al., 2007; Mondou et al., 2010; Vieira et al., 2007; Novo et al., 2018).

The metasediments represented by the Tumiritinga and São Tomé formations in the studied region (Figure 14A and B, and 16A to C) were mapped and described by Signorelli (2000). The rocks of Tumiritinga Formation are essentially medium-grained biotite-quartz schists to gneiss with cordierite, garnet, sillimanite, muscovite, quartz, and biotite. Common intercalations composed of calc-silicate rocks are observed. Microscopic observation of thin sections of the schists/gneisses reveals as the main constituents quartz, plagioclase, biotite, sillimanite, cordierite, and muscovite. Accessory minerals are represented by apatite, zircon, garnet, microcline, sericite, chlorite, epidote, and titanite. The texture is granoblastic to lepidoblastic. Recrystallization features are also described. The predominant lithotype of the São Tomé Formation is a (feldspar)-(muscovite)-(sillimanite)-quartz-biotite fine-grained schist. Intercalation of calc-silicate rocks within the schists are composed of quartz, biotite, muscovite, amphibole, and epidote.



Figure 16 – Outcrops of the partially molten metasediments in the study area (Tumiritinga Formation). A, B and C: migmatitic gneisses showing compositional banding and well-defined foliation planes.

II.1.3.2.4. Magmatic suites

Extensive magmatism is recognized in the Araçuaí orogenic belt and Pedrosa-Soares et al. (2011) proposed a subdivision to the magmatic bodies according mainly to their location, ages, and geochemistry. These magmatic bodies in the internal domain (Siga-Júnior, 1986; Pedrosa-Soares and Weidemann-Leonardos, 2000; Pedrosa-Soares et al., 2001) were grouped into the G1 (ca. 630-585 Ma), G2 (ca. 585-560 Ma), G3 (ca. 545-530 Ma), G4 and G5 (530-490 Ma) supersuites (Pedrosa-Soares et al., 2011), characterizing different orogenic stages. This subdivision represents a long period of continuous emplacement of igneous bodies between ca. 640 and 480 Ma in a collisional context. The G1 pre- to syn-collisional supersuite (Figure 10, #4) mainly consists of tonalite to granodiorite, with mafic to dioritic facies and enclaves, representing a continental calc-alkaline magmatic arc. The G2 includes S-type granites (Figure 10, #3) formed during the syn-collisional stage and comprises peraluminous garnet-biotite granites, with ubiquitous remnants of banded paragneisses and migmatites. The typical G3 rocks are garnet-cordierite leucogranites, described as a result of anatexis of S-type G2 granites during late- to post-collisional stage (Figure 10, #3). At the post-collisional stage (530-480 Ma) G4 and G5 supersuites were generated (Figure 10, #2). The S-type G4 mostly consists of garnet-bearing two mica leucogranites associated with orogen gravitational collapse. The main rock types of the G5 supersuite vary in composition from syenogranites to granodiorites, related to partial re-melting from a mainly metaluminous continental crust and dehydration melting from slightly peraluminous rock (Roncato, 2009; Pedrosa-Soares et al., 2007, 2011; Gradim et al, 2014; Gonçalves et al., 2015).

These plutonic bodies are included in the allochthonous domain in the internal portion of the Araçuaí orogenic belt, which is comprised of the three main units previously

cited above: the WMU, CPU, and EAU (Vauchez et al., 2007; Mondou et al., 2012; Cavalcante et al., 2013).

The WMU is an allochthonous unit thrust onto the para-autochthonous cover of the São Francisco craton (Oliveira et al., 2000). The WMU is comprised of HT-LP (ca. 750 °C, 0.6 GPa) mylonites that display evidence of westward thrusting derived from metasedimentary protoliths. A few zircon ages have been obtained for plutonic bodies hosted in this unit (appendix B). The magmatic evolution started with gabbro-dioritic and tonalitic plutons (e.g. Chaves pluton; U-Pb age: ca. 599 Ma; and Brasilândia pluton, U-Pb age: ca. 581 Ma), followed by late granodioritic intrusions (e.g. Guarataia pluton, U-Pb age: ca. 576 Ma) (Noce et al., 2000; Tedeschi et al., 2016). Petitgirard et al. (2009) have dated leucocratic sills interlayered in the mylonites which indicate partial melting at 577 ± 9 Ma (U-Pb on zircon). These authors have also reported $^{40}\text{Ar}/^{39}\text{Ar}$ ages of ca. 501 and ca. 495 Ma for amphiboles, and ca. 477 and ca. 468 Ma for biotites from the WMU.

The Guarataia, Brasilândia, and Chaves plutons represent the widespread magma production in the Rio Doce magmatic arc (Tedeschi et al., 2016). These rocks have been mapped by Signorelli (2000) and Tedeschi (2013) in the studied region (Figure 14B). The Guarataia pluton (Figures 14B and 17A to C) comprises fine- to coarse-grained porphyritic epidote-biotite granodiorite to granite. Thin section observations show hipidiomorphic equigranular texture and presence or not of magmatic flow foliation. When present, the foliation is defined by biotite and less frequently by feldspar crystals. The primary mineralogy is composed of plagioclase, microcline, quartz, and biotite (Signorelli, 2000; Martins et al., 2004; Tedeschi et al., 2013). Noce et al. (2000) and Tedeschi (2013) reported a Pb-Pb in zircon crystallization age of 574 ± 2 Ma, and an U-Pb in zircon of 576 ± 9 Ma, respectively.

The Brasilândia pluton (Figures 14B and 17E) varies in composition from tonalites to granites with a fine- to medium-coarse grained texture. Foliation is commonly observed and marked by biotite crystals. Thin section petrography reveals that amphibole, biotite, microcline, K-feldspar, and plagioclase characterize the primary mineralogy and texture is lepidogranoblastic (Martins et al., 2004; Tedeschi, 2013). Noce et al. (2000) using Pb-Pb evaporation method in 3 zircon crystals reported a crystallization age of 595 ± 3 Ma. U-Pb in zircons revealed a crystallization age of 581 ± 11 Ma (Tedeschi, 2013). Signorelli (2000) described isolated enderbitic bodies and hypersthene-bearing rocks emplaced in the Brasilândia pluton domain. However, later studies performed by Afonseca et al. (2012),

Tedeschi et al. (2012), and Tedeschi (2013) subdivided this pluton in Brasilândia Tonalite to the west and Chaves Enderbite to the east.

The Chaves Enderbite (Figures 14B and 17D) is characterized by orthopyroxene-bearing rocks. The main rock type is a medium- to coarse-grained biotite-enderbite with lepidonematoblastic texture. Inequigranular hipidiomorphic texture is also common. The primary mineralogy is defined by plagioclase, biotite, quartz, orthopyroxene, and clinopyroxene, the latter altered to amphibole and/or biotite. Minor gabronorite, opdalite, charnockite, and biotite-monzogranite facies are also described. Contacts among those facies are transitional, marked by hybrid zones involving mixing of rocks from two or more facies. Seven spots (U-Pb in zircon) in the gabronorite facies yielded a crystallization age of 599 ± 15 Ma (Tedeschi, 2013; Tedeschi et al., 2016).

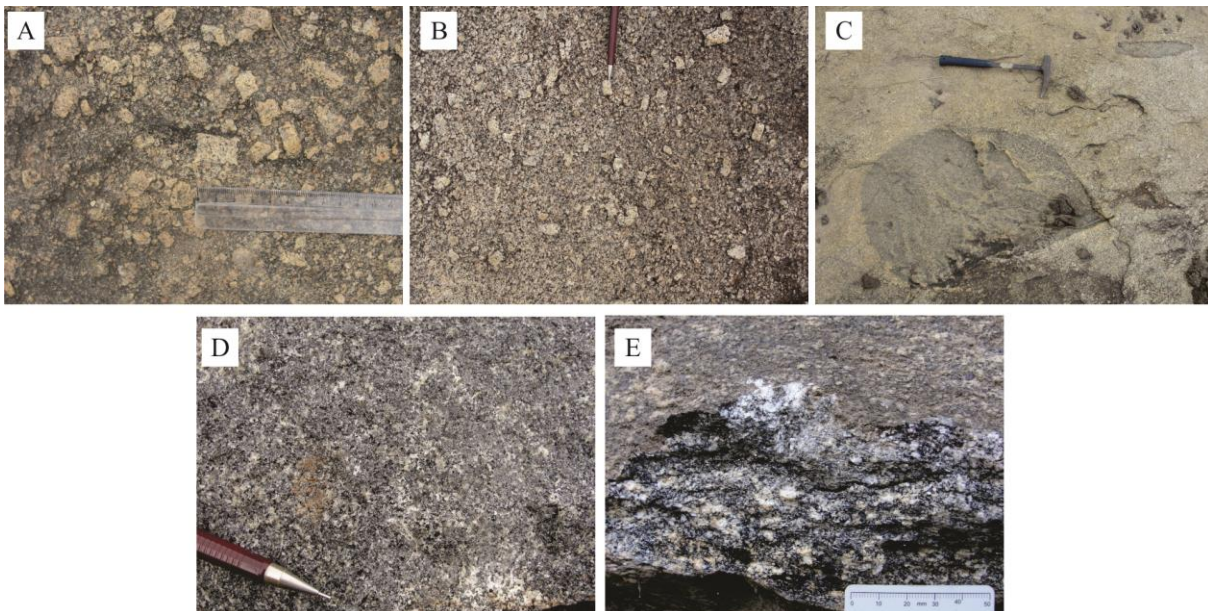


Figure 17 – Guarataia Granodiorite in the studied area showing porphyritic texture marked by larger feldspar crystals (A and B), and the presence of rounded enclaves with same composition of the host, but with a higher content of mafic minerals. D: fine-grained Chaves Enderbite sample. E: Brasilândia Tonalite with well-defined foliation marked by biotite crystals.

The plutonism in the CPU consists of tonalitic to granodioritic bodies (the “Galiléia” and “São Vitor”) emplaced during a magmatic event ca. 580 Ma and deformed at the magmatic state, coherently with their metasedimentary country rocks (Vauchez et al., 2007; Mondou et al., 2012). These bodies have calc-alkaline composition interpreted as representative of a magmatic arc, which would span from 630 to 585 or 580 Ma (e.g. Tedeschi et al., 2016). Several other ages were reported for subsidiary synkinematic

granitoids of the CPU close to the contact with the WMU. Zircon ages of ca. 592 Ma (Mondou et al., 2012) were obtained for tonalite sills ascribed to the Derribadinha suite, near Governador Valadares city (Figure 14A), similar to ages reported by the same authors for leucocratic veins interlayered with mylonitic metasediments. Gonçalves et al. (2014) obtained an age of ca. 597 Ma for a tonalite south of the previous locations and for the same suite. To the north of these studies, Noce et al. (2000) dated the Palmital and Wolff leucogranites, near Teófilo Otoni city (Figure 14A), which yielded ages of ca. 582 and 585 Ma, respectively. It is suggested that these leucogranites are derived from melting of peraluminous metapelites, contemporaneous to the formation of the tonalitic magmas.

The main magmatic bodies of the CPU in the study region are represented by the São Vitor and Galiléia tonalites (Figures 14B and 18), with blue-grey color, medium to coarse-grained and locally porphyritic (Signorelli, 2000). These bodies are biotite-hornblende bearing rocks, with primary mineralogy composed of quartz, plagioclase, minor microcline and orthoclase, and garnet. Composition varies from tonalites to granodiorites. The texture is typical of slow cooling rocks. Four U-Pb zircon ages of 585 ± 4 Ma (Mondou et al., 2010), 615 ± 6 Ma, 584 ± 8 Ma, 594 ± 5 Ma (Pinto, 2015) are reported for the São Vitor Tonalite in the study region (appendix B).



Figure 18 – Outcrops of the São Vitor Tonalite. A and B: well defined magmatic foliation marked by biotite and feldspar crystals. C: foliation marked by elongated mafic enclave.

The EAU is a large area dominated by anatectic rocks, formed by partial melting of the middle crust and deformed predominantly in the magmatic state (Cavalcante et al., 2013). It is dominated by anatexites (Carlos Chagas – e.g. Cavalcante et al., 2013, 2018), and anatectic granites (Ataléia Suite – e.g. Tuller, 2000; Gradim et al., 2014) associated with migmatitic granulite and kinzigite (e.g. Richter et al., 2015). Several of SHRIMP U-Pb ages are reported for the EAU anatexites (Vauchez et al., 2007; Cavalcante et al., 2018). A number of diatexites and anatectic granites yielded ages in the range ca. 597-593 Ma, and others in the

interval of 589 and 572 Ma. The age distribution suggests a younging from NW to SE and from WNW to ESE in the Carlos Chagas batholith (Cavalcante et al., 2018).

Investigations of Cavalcante et al. (2014, 2018) using Ti-in-quartz and the Zr-in-rutile geothermometers in anatexites documented temperatures of 780-800 °C for the EAU. Fe-Mg exchange geothermometers in kinzigites yielded pressures in the range of 650-700 Mpa, interpreted as P-T conditions under which crystallization of anatexites began during cooling. Munhá et al. (2005) and Richter et al. (2016) obtained similar P-T conditions for migmatitic kinzigites. Cavalcante et al. (2018) suggest that collision should have started before ca. 600 Ma and the middle crust remained partially molten over a period of at least ca. 25 Ma. Magmatic fabric in the EAU is marked by a magmatic foliation that dips gently in various directions due to open folds that affected an initially low-angle foliation (Cavalcante et al., 2013). In addition, magnetic foliations and lineations reveal a complex flow field, characterized by a western and an eastern domain. The western domain comprises gently dipping foliations bearing lineations that progressively rotate from SW in the south to NW in the north. The eastern domain is dominated by subvertical NS-trending foliations bearing subhorizontal orogen-parallel lineations. This pattern is interpreted as the result of the combination of convergence and gravity-driven forces that promoted a 'channel flow like' tectonic behavior.

The magmatic bodies in the EAU in the studied region were described by Tuller (2000). According to his work, the predominant lithotype of the kinzigites (Figure 14B) is a sillimanite-garnet-cordierite-biotite gneiss of fine- to medium-grained texture, frequently exhibiting compositional banding in which felsic layers are represented by a quartz-feldspathic association (and cordierite) and the mafic bands are composed of biotite (and sillimanite). Thin section investigations show that the main mineralogy is defined by quartz, plagioclase, microcline, cordierite, sillimanite, garnet, and biotite. Texture is granoblastic to lepidoblastic.

These kinzigites gradually pass to the Ataléia Granites (Figure 14B), which are represented mainly by garnet-biotite tonalites, with variations to granodiorites and granites, of medium- to coarse-grained texture, foliated to gneissic structures. Microscopic studies show the presence of quartz, orthoclase, microcline, plagioclase, biotite, garnet, cordierite, and sillimanite. Texture varies from hypidiomorphic granular to granoblastic. The Ataléia Granite hosts metasedimentary enclaves (Tuller, 2000; Gradim et al., 2014). Noce et al. (2000)

through Pb-Pb evaporation in zircon obtained a crystallization age of 591 ± 5 Ma (appendix B) for the Ataleia Granite, near the city of Ataleia (Figure 13A and B).

The Carlos Chagas leucogranite in the eastern border of the studied area (Figure 14B) is dominantly characterized by a fine- to coarse-grained leucogranite with biotite, garnet, and sillimanite, with a texture varying from lepidoblastic to granoblastic. The primary mineralogical composition is indicated by quartz, plagioclase, microcline, orthoclase, biotite, muscovite, sillimanite, and garnet. Porphyritic leucogranites with a fine- to medium coarse-grained matrix presenting feldspar megacrysts (> 5 cm) are subordinated to the main lithotype (Tuller, 2000; Cavalcante et al., 2013).

Charnockite and biotite-granite intruded the anatexites during late magmatic event recorded from ca. 540 to 480 Ma (Noce et al., 2000; Mondou et al., 2012; Toledo, 2015; Xavier, 2017). The Caladão Granite and Padre Paraíso Charnockite integrate the Aimorés Suite (Pinto et al., 1997). Tuller (2000) described the rocks of this suite in the studied region (Figure 19). The Caladão Granite (Figures 14B and 19A to C) is comprised mainly by a porphyritic biotite-granite, with predominantly euhedral K-feldspar megacrysts of ~6 centimeters in length. These megacrysts are commonly oriented. The matrix is medium to coarse-grained and weakly foliated, composed mainly by biotite crystals. Observations under petrographic microscope exhibit mineralogy composed of microcline, plagioclase, biotite, and allanite (rare), with a hypidiomorphic granular, porphyritic texture. The Padre Paraíso Charnockite (Figures 13B and 19D to F) is greenish gray in color, predominantly represented by a porphyritic charnockite, with euhedral feldspar megacrysts of 2 to 7 centimeters in length, generally randomly distributed in a medium coarse-grained matrix composed by weakly oriented biotite. The mineralogy under a petrographic microscope is characterized by the presence of quartz, plagioclase, orthoclase, microcline, hornblende, biotite, and hypersthene, composing a hypidiomorphic granular, porphyritic texture.

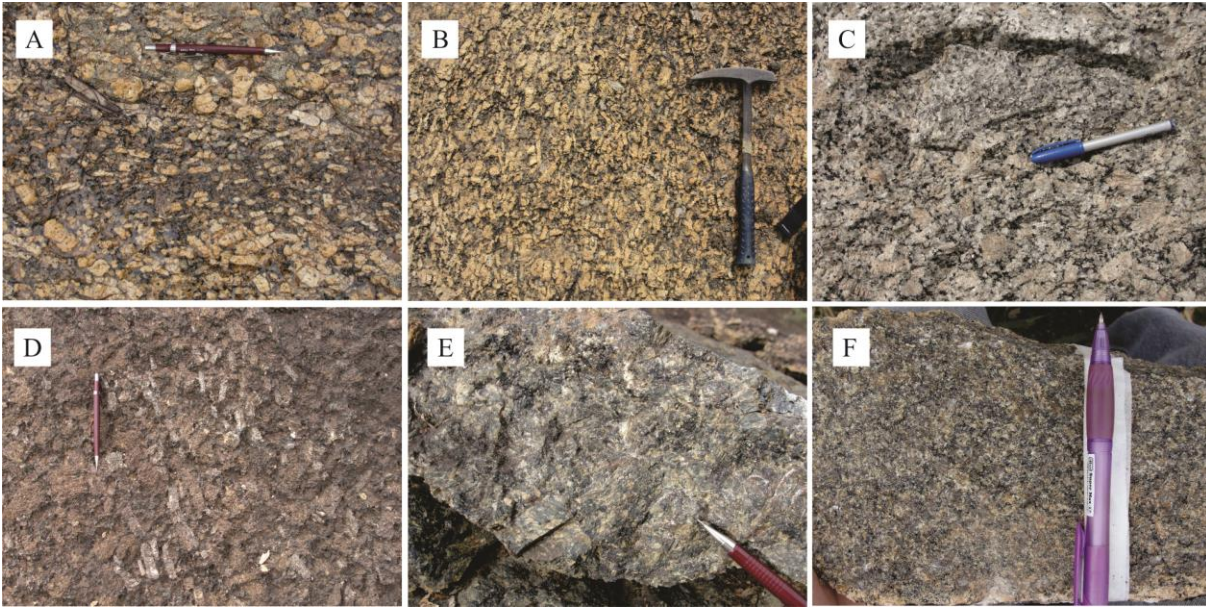


Figure 19 – A, B, and C: typical outcrops of the Caladão Granite, showing well defined magmatic fabric marked by feldspar crystals. Padre Paraíso Charnockite showing well defined magmatic fabric (D) and typical coarse- (E) and fine-grained (F) samples. Both feldspar and orthopyroxene tend to have a greenish or brown hue.

II.1.3.3 Tectonic evolution models of the Araçuaí orogen

The evolution models of the Neoproterozoic Araçuaí orogenic belt consider that together with its counterpart denominated West-Congo belt, formed between the São Francisco and Congo cratons, during the amalgamation of Western Gondwana (Hasui et al., 1975; Almeida, 1977; Trompette et al., 1992; Pedrosa-Soares et al., 2007).

The kinematic evolution of the Araçuaí - West Congo orogenic system has been discussed qualitatively by Alkmim et al. (2006), who presented the “nutcracker” model. At the time it formed, the Araçuaí – West Congo orogen was bounded on the west, north, and east by the São Francisco and Congo cratons, a crustal block that had a shape of a lopsided, upside-down ‘U’. Therefore, the orogen was partially confined during deformation. In their model, the orogenic system formed in response to the closure of the Macaúbas basin. This basin was partially underlain by oceanic crust. The closure occurred when the São Francisco craton rotated anticlockwise towards the Congo craton. The São Francisco and Congo cratons, like pincers of a nutcracker, and articulated along interior rifts (aulacogens), rotated against each other. The driven forces for the closure were triggered by collisions along the margins of the São Francisco and Congo Cratons during the final assembly of Western Gondwana.

Recent studies (Fossen et al., 2017; Cavalcante et al., 2018, 2019) show that this model is incompatible with the general orogenic evolution proposed in recent literature, which involves ca. 50 Ma of subduction of oceanic crust and associated arc formation, followed by collisional orogeny and crustal thickening. Cavalcante et al. (2019) suggest that oceanic crust was nonexistent or very limited in the Macaúbas basin.

Tonalitic and granodioritic bodies emplaced ca. 580 Ma in the plutonic unit (CPU in the internal domain), together with other plutons dated from 630 to 580 Ma (Tedeschi et al., 2016) have calc-alkaline composition and were interpreted as representative of a magmatic arc which would span from ca. 630 to 580 Ma, implying the consumption of oceanic crust for 45-50 Ma. Cavalcante et al. (2018) show that there is a very long time span (ca. 200 Ma) between the age of the possible ophiolite fragments (Pedrosa-Soares et al., 1998) and the early magmatism that is interpreted as arc magmatism and subduction initiation. age of the possible ophiolite fragment. This implies in a wide pre orogenic ocean in width to that of the Atlantic Ocean, since nearly all current oceanic crust is younger than 200 Ma. Subducting such a wide ocean over 50 Ma is not compatible in a confined system such as the Araçuaí-West Congo.

Quantitative considerations show that the “nutcracker” model is too rigid to explain the crustal thickening and they indicate that the São Francisco – Congo bridge was broken by a wide orogenic corridor (the Gabon corridor) along the current African Atlantic margin. This corridor was able to accommodate the shortening and it is an important element that “broke” the São Francisco-Congo bridge and provided increased flexibility during Neoproterozoic rifting and Brasiliano orogeny.

These authors also find strong support in currently available P-T, geochronologic, petrographic, and structural data (Vauchez et al., 2007; Mondou et al., 2012; Meira et al., 2015; Cavalcante et al., 2013, 2014, 2018) to explain the Araçuaí orogen as a hot intracontinental orogen. New radiometric and thermal data show that crystallization of the anatectic core of the orogen (EAU, Carlos Chagas anatectic domain) was going on already ca. 600 Ma, and that the middle crust at this point was already heated to >750 °C in a large area (Cavalcante et al., 2018). The achievement of such high temperatures and associated partial melting together with the transformation of a thinned crust to an over-thickened crust requires time (ca. 20 Ma; Horton et al., 2016). Thus, thickening could well have started at 630-620 Ma. This eliminates the model involving prolonged subduction of a vast oceanic crust. The heat production from radioactive elements (U, Th, K) sources could be sufficient for partial

melting of the thickened continental crust (Jamieson et al., 1988; Sandiford and McLaren, 2002; Faccenda et al., 2008). An illustration of such orogenic evolution is shown in Figure 20.

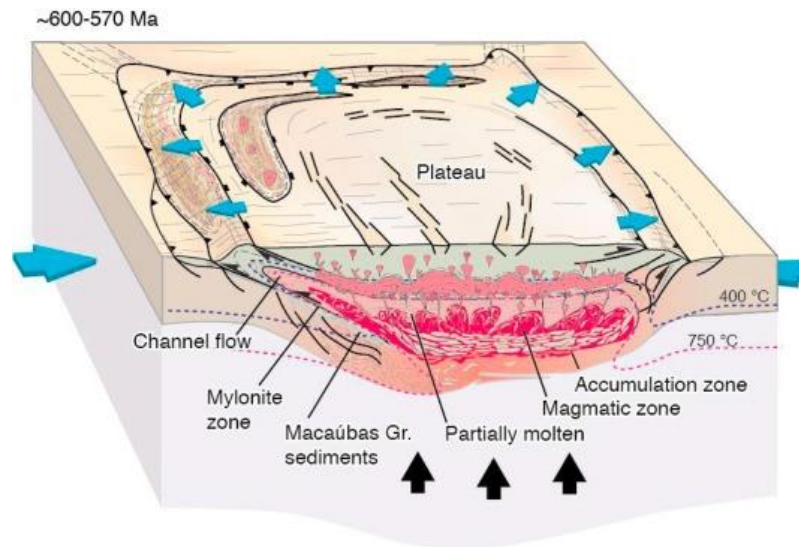


Figure 20 – Schematic illustration of the formation of a hot orogen showing widespread partial melting (Source: Cavalcante et al., 2019).

The Araçuaí belt displays evidence of high-temperature contractional deformation distributed almost homogeneously all over its internal domain (Vauchez et al., 2007). Pressure-temperature estimates consistently point to synkinematic conditions between ca. 750 °C / 500-600 Mpa and ≥ 800 °C / 600-700 Mpa (Petitgirard et al., 2009; Cavalcante et al., 2014; Moraes et al., 2015; Richter et al., 2016), supporting a temperature gradient of 30-35 °C/km down to 25 km depth at least. Cavalcante et al. (2018) also substantiated that anatexis was active in the core of the belt during ca. 30 Ma. Anisotropy of magnetic susceptibility (AMS) and microstructural investigations in the CPU and EAU reveal a magmatic-state complex middle-crust flow pattern. Mondou et al. (2012) mapped the São Vitor and Galileia tonalitic batholith in the CPU and suggest a 3D deformation of a slowly cooling, large magmatic body and its country rock (Rio Doce group metasedimentary rocks). These plutonic bodies display a consistent magmatic fabric that evolves eastwards from a gently eastward-dipping foliation bearing a dominantly EW-trending lineation that switches from subvertical to subhorizontal over an interval of a few tens of meters. In the easternmost part of the CPU (near the contact with the EAU), Mondou et al. (2012) have substantiated the presence of subhorizontal magmatic foliations bearing orogen-parallel NS trending magmatic lineation. These authors indicate that the development of the flow field was promoted by the low viscosity of the middle crust (e.g. Rosenberg and Handy, 2000) that turned gravitational force

as an active tectonic force combined with the convergence between the São Francisco and Congo cratons. Moreover, microstructural investigations and U-Pb dating showed that deformation occurred before crystallization.

Cavalcante et al. (2013) studied the strain distribution in the Carlos Chagas anatexite in the EAU and also found a complex 3D flow fabric generated due to the interplay of collision-driven and gravity-driven deformations. Correlation of U-Pb SHRIMP zircon crystallization ages and Ti-in-zircon average temperatures, assumed as the temperature range in which zircon was completely crystallized across the Carlos Chagas anatexite show a younging trend from the western (597 Ma) to the eastern (572 Ma), suggesting a “wave of crystallization” under nearly the same temperatures. This could be explained by a “channel flow model” in which the upper (western) part of the channel would have crystallized first (Cavalcante et al., 2013, 2018). Channel flow has been invoked to explain deformation of modern hot orogens such as the Hymalaian-Tibet system (e.g. Hodges et al., 1992).

CHAPTER IV

Midcrust deformation regime variations across the Neoproterozoic Araçuaí hot orogen (SE Brazil): insights from structural and magnetic fabric analyses

Article submitted to the Journal of Structural Geology on June 6th, 2019.

Tiago Valim ANGELO^{1,*}, Marcos EGYDIO-SILVA¹, Filipe Altoé TEMPORIM², Marina SERAINE Fernandes de Souza³

¹Universidade de São Paulo, Instituto de Geociências, R. do Lago, 562, 055080-080, São Paulo, SP, Brazil.

²Universidade de São Paulo, Instituto de Astronomia, Geofísica e Ciências Atmosféricas, R. do Matão, 1226, 05508-090, São Paulo, SP, Brazil.

³Universidade de Brasília, Instituto de Geociências, Asa Norte, 70297-400, Brasília, DF, Brazil.

*Corresponding author: valim206@gmail.com; +55 61 98314-9607

Keywords: magmatic flow, anisotropy of magnetic susceptibility, rock magnetism, Araçuaí belt, magnetic fabric, hot orogen

Abstract

The Neoproterozoic Araçuaí belt of eastern Brazil formed during the amalgamation of Western Gondwana and holds characteristics of a hot collisional belt; large volumes of magma, partial melting of the middle crust, and slow cooling rates. This work combines structural, magnetic, and geochronological study related to the flow of rocks, deformation history, and structural patterns associated with the history of this orogen. Microstructural observations support that deformation of the plutonic bodies occurred in the magmatic state, while the host metasedimentary and basement rocks deformed in the solid-state. A detailed structural mapping integrating field and anisotropy of magnetic susceptibility (AMS) revealed four domains with contrasting flow patterns. The structural patterns from W to E are characterized by: westward thrusting orthogonal to the belt (region 1), orogen-parallel tranpression induced strain partitioning (regions 2 and 3), and orogen-parallel flow and subsidiary eastward vergence magmatic flow (region 4). Anisotropy of anhysteretic remanent magnetization (AARM) and magnetic mineralogy investigations suggest that the main carriers

of the AMS are biotite and/or amphibole in dominantly paramagnetic samples (host metasediments and basement unit), and multi-domain (MD) or pseudo-single domain (PSD) magnetite grains in dominantly ferromagnetic samples (plutonic bodies). U-Pb dating of zircons from granitoids in the western arc border and central arc regions (structural regions 1, 2, and 3) reveal that magmatism occurred between 615-567 Ma, and deformation occurred before complete solidification. This magmatism is associated with the main tectono-metamorphic peak attained by the orogen. To the east (structural region 4), younger bodies were emplaced in a still thermally buffered environment, but after solidification of the anatectic country rock. This late magmatism (540-480 Ma) is associated with a minor tectono-metamorphic peak, and magmatic deformation affected these bodies during that time. In such context of protracted deformation under slow cooling conditions, the composite observed fabric results from the interplay of collision-driven (thrusting and transpression strain partitioning) and gravity-driven (orogen-parallel flow) deformations, induced by the East-West convergence between the São Francisco and Congo Cratons.

IV.1. INTRODUCTION

Collisional orogenic belts characterized by high temperatures, slow cooling rates, and excessive amount of melt in the hinterland (“hot orogens”) are characterized by thermally-weakened rock strength due to the effects of large volume of magma in the crust (Fossen et al., 2017; Jamieson et al., 2011). These aspects have important consequences on the forces that control the dynamic of these hot orogens. Previous studies demonstrate that crustal thickening induced by compression is accommodated by a transpressional regime in combination with orogen-parallel escape flow along sub-horizontal structures. This accommodation reflects the weakness of the hot lithosphere which would not be able to sustain the load of high topographies of the orogen (e.g., Beaumont et al., 2001; Rey et al., 2001; Chardon et al., 2009). In addition, under high geothermal conditions (>30 °C/km), partial melting is pervasive in the middle crust and strain repartition is less efficient, leading to homogeneous deformation of a large volume of rocks (Vauchez and Tommasi, 2003; Vauchez et al., 2007).

Anisotropy of magnetic susceptibility (AMS) has been extensively used for retrieving the mineral preferred orientation fabrics of plutons and metasedimentary rocks (e.g., Ellwood, 1982; Bouchez, 2000, Park et al., 2005; Egydio-Silva et al., 2005, Archanjo et al., 2008; Mondou et al., 2012; Maffione et al., 2015; Parsons et al., 2016) in order to access

information related to the flow of rocks in orogenic areas. The kinematic and geometric pattern of the fabric is required to understand how complex deformation regimes are accommodated as a reflex of tectonic regional stresses related to the crustal strain. To better constrain the imposed deformation and consequently the tectonic processes active during collision, we studied the strain distribution through AMS in the hinterland portion and adjacent areas of a segment of the Araçuaí belt, which experienced slow ($<5^{\circ}\text{C}/\text{My}$) regional cooling from synkinematic high temperature deformation ($\sim 750^{\circ}\text{C}$) and low pressure (600 MPa) conditions (Petitgirard et al., 2009). In addition, we performed rock magnetic studies in order to reveal the carriers of the magnetic anisotropies and zircon data from a syn-kinematic tonalitic body emplaced in arc-related metasedimentary rocks. The review of the literature regarding structural and geochronological data combined with new AMS measurements performed to obtain reliable structural maps, allow us to discuss the deformation history and structural patterns associated with the behavior of this orogenic setting.

IV.2. GEOLOGICAL SETTING

The Neoproterozoic Araçuaí belt is the northern segment of the Ribeira-Araçuaí orogenic system, formed during the Brasiliano/Pan-African Orogeny during the amalgamation of West Gondwana (Fig. 21A) (Almeida et al., 1977; Bento dos Santos et al., 2015). The Ribeira-Araçuaí system, from North to South, is characterized by a change in the deformation regime pattern and with the advancement of the investigations, the limit of the belts began to be discussed based on correlation and continuity of lithostratigraphic units, structural patterns, and geophysics (e.g. Egydio-Silva and Vauchez, 2011; Egydio-Silva et al., 2018). The Ribeira belt trends NE-SW and is characterized by a transpressional deformation regime (Trompette, 1994; Egydio-Silva et al., 2002; Egydio-Silva et al., 2018). To the North, the \sim N-S structural trend of the Araçuaí belt is a consequence of a contractional regime involving the westward thrust of allochthonous units onto the margin of the São Francisco craton (Cunningham et al., 1998; Oliveira et al., 2000; Vauchez et al., 2007; Egydio-Silva et al., 2018). These studies show that the transition between the belts is gradual and support that they are part of the same orogenic belt, but with different kinematics and tectonic style (Egydio-Silva et al., 2018). This variation is interpreted as a reflex of the rigid termination of the southern portion of the São Francisco craton (Vauchez et al., 1994; Egydio-Silva et al., 2005).

Oliveira et al. (2000) and Vauchez et al. (2007) highlight different lithologic and tectonic characteristics to describe and subdivide the Araçuaí belt in three main allochthonous

units. From west to east, these domains are the Western Mylonitic Unit (WMU), the Central Plutonic Unit (CPU), and the Eastern Anatectic Unit (EAU) (Fig. 21A).

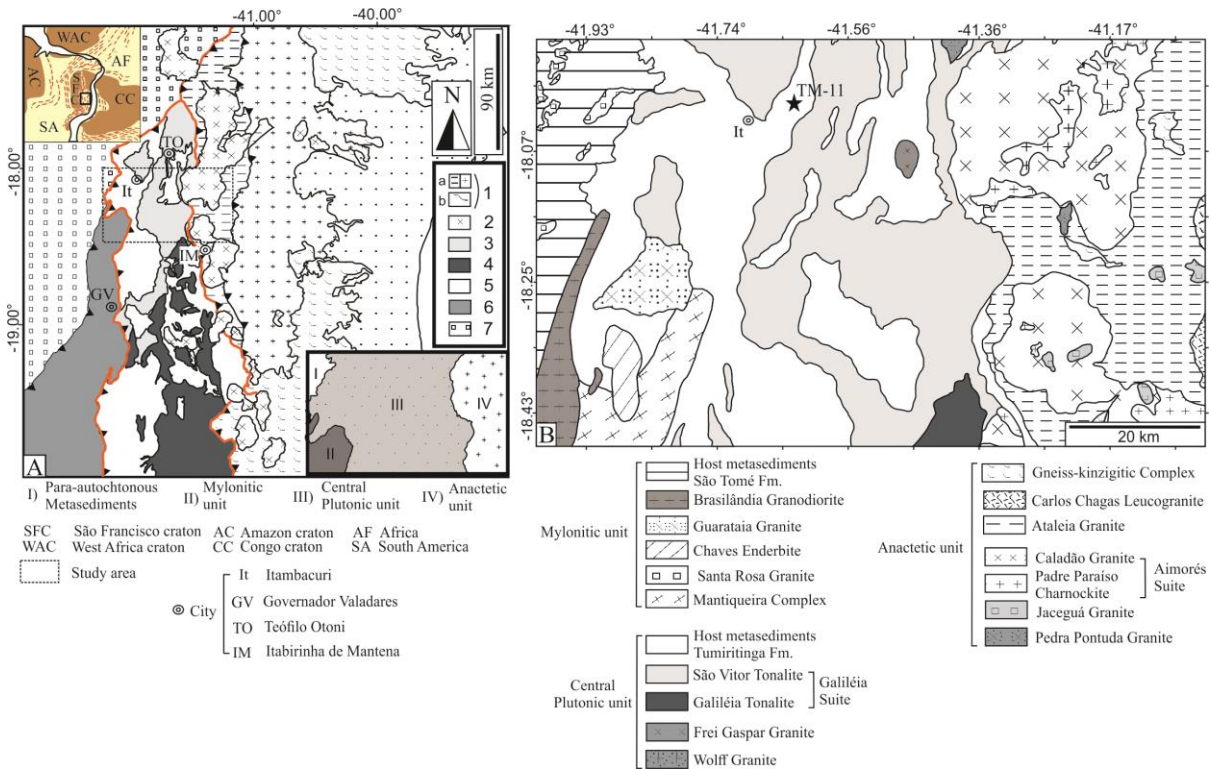


Fig. 21. A: Simplified map of the Araçuaí belt (after Vauchez et al., 2007) showing its main tectonic domains: (1) thick (> 10 km) layer of diatexites, metatexites, and anatectic granites (a) associated with migmatitic granulites and migmatitic kinzigite (b) intruded by late orogenic porphyritic granitoids associated with charnockites (2) characterizing the Eastern Anatectic Unit. The Central Plutonic Unit comprises the São Vitor Tonalite (3) and (4) Galiléia batholith intruding (5) high-T metasedimentary rocks. Metasedimentary and metaigneous mylonites from the Mylonitic Unit (6) thrust upon the para-autochthonous metasedimentary cover of the São Francisco craton (7). The orange line separates the limit between lithological domains. The dashed box shows the location of the study area, detailed in B. B: Schematic geological map showing the various rock types in the studied region. Zircon U-Pb dating was conducted in sample TM11 (São Vitor Tonalite), and details about the characteristics of the outcrop and sample are described in section “5.1” of this study.

The WMU (Fig. 21A) is an allochthonous unit thrust onto the para-autochthonous cover of the São Francisco craton (Oliveira et al., 2000). The WMU is comprised of HT-LP (ca. 750 °C, 0.6 Gpa) mylonites that display evidence of westward thrusting derived from metasedimentary protoliths. Signorelli (2000) describe the basement rocks of the Mantiqueira Complex, which are characterized by tonalitic to granodioritic composition migmatitic gneiss with a steeply dipping (ca. 70°) principal foliation oriented ~NNE (Duarte et al., 2004; Noce et al., 2007a; Noce et al., 2007b). A few zircon ages have been obtained for this unit. The magmatic evolution started with gabbro-dioritic and tonalitic plutons (e.g. Chaves pluton; U-Pb age: ca. 599 Ma; and Brasilândia pluton, U-Pb age: ca. 581 Ma), followed by late granodioritic intrusions (e.g. Guarataia pluton, U-Pb age: ca. 576 Ma) (Noce et al., 2000; Tedeschi et al., 2016). Petitgirard et al. (2009) have dated leucocratic sills interlayered in the

mylonites which indicate partial melting at 577 ± 9 Ma (U-Pb on zircon). These authors have also reported $^{40}\text{Ar}/^{39}\text{Ar}$ ages of ca. 501 and ca. 495 Ma for amphiboles, and ca. 477 and ca. 468 for biotites from the WMU.

The CPU (Fig. 21A) is composed of several tonalitic to granodioritic bodies hosted in the arc-related Rio-Doce metasediments. The metasedimentary rocks represented by the Rio-Doce Group (Vieira, 2007; Novo et al., 2018) encompasses four formations (from base to top): Palmital do Sul, Tumiritinga, São Tomé, and João Pinto Formations. The Palmital do Sul and Tumiritinga Formations mostly comprise pelitic schists to paragneisses, interbedded with metavolcanic and meta-volcaniclastic rocks. The São Tomé Formation is characterized by psammitic to pelitic meta-turbidites with lenses of calcsilicate rocks. The João Pinto Formation comprises sandstones. The magmatic crystallization ages of ca. 595 and ca. 584 Ma were obtained for the volcanic protoliths (U-Pb on zircon; Vieira, 2007; Novo et al., 2018). The Tumiritinga and São Tomé Formations are widely distributed throughout the studied area, the former included in the CPU, while the latter covers the para-autochthonous metasedimentary cover (Fig. 21A) of the São Francisco Craton (Fig. 20A).

The main magmatic bodies of the CPU at the eastern and central zones are the São Vitor and Galiléia tonalites, included in the Galiléia intrusive suite (Oliveira et al., 2000; Narduzzi et al., 2017). These syn-collisional tonalitic and granodioritic bodies were emplaced during a magmatic event from ca. 615 (± 6) to ca. 567 (± 4) Ma (U-Pb on zircon, Mondou et al., 2012; Pinto, 2015; Gonçalves et al., 2014; Nalini et al., 2000; Noce et al., 2000) in metasedimentary rocks that deformed coherently due to the parallelism between the fabric of the plutons and country-rock. Transpressional deformation regime is predominant in the CPU bearing steeply dipping foliations and coexistence of horizontal and vertical lineations. Mondou et al. (2012) reported a complex 3D strain pattern associated with belt normal thrusting and subsidiary belt-parallel transcurrent motions.

Several other ages were reported for subsidiary synkinematic granitoids of the CPU close to the contact with the WMU. Zircon ages of 581 (± 4) Ma and 583 (± 4) Ma (Mondou et al., 2012) were obtained for tonalite sills ascribed to the Derribadinha suite. Similar ages were reported by the same authors for leucocratic veins interlayered with mylonitic metasediments. Gonçalves et al. (2014) obtained an age of ca. 597 (± 4) Ma for a tonalite south of the previous locations and for the same suite. To the north of these studies, Noce et al. (2000) and Nalini et al. (2000) dated the Palmital and Wolff leucogranites, which yielded ages of 582 (± 5) Ma and

582 (± 5) Ma, respectively. It is suggested that these granites are derived from melting of peraluminous metapelites, contemporaneous to the formation of the tonalitic magmas.

The EAU (Fig.21A) is dominated by anatexites (Carlos Chagas unit – e.g. Cavalcante et al., 2013, 2018), and anatectic granite (Ataleia Granite – e.g. Tuller, 2000; Gradim et al., 2014) associated with migmatitic granulite and kinzigite originated from partial melting of metasediments. These kinzigite contain biotite, garnet, cordierite, sillimanite, but no staurolite or muscovite. Several of SHRIMP U-Pb ages are reported for the EAU anatexites (Vauchez et al., 2007; Cavalcante et al., 2018). A number of diatexites and anatectic granites yielded ages in the range ca. 597-593 Ma, and others in the interval of 589 and 572 Ma. The age distribution suggests a younging from NW to SE and from WNW to ESE. Charnockite and biotite-granite intruded the anatexites during late magmatic event recorded from ca. 540 to 480 Ma (Noce et al., 2000; Mondou et al., 2012; Toledo, 2015; Xavier, 2017). The Caladão Granite and Padre Paraíso Charnockite integrate the Aimorés Suite (Pinto et al., 1997) and represent late magmatic pulses in the studied region.

Investigations of Cavalcante et al. (2014, 2018) using the Ti-in-quartz and the Zr-in-rutile geothermometers in anatexites documented temperatures of 780-800 °C for the EAU. Fe-Mg exchange geothermobarometers in kinzigites yielded pressures in the range of 650-700 MPa, interpreted as P-T conditions under which crystallization of anatexites began during cooling. Munhá et al. (2005) and Richter et al. (2016) obtained similar P-T conditions for migmatitic kinzigites. Cavalcante et al. (2018) suggest that collision should have started before ca. 600 Ma, and the middle crust remained partially molten over a period of at least ca. 25 Ma.

Magmatic fabric in the EAU is marked by a magmatic foliation that dips gently in various directions due to open folds that affected an initially low-angle foliation (Cavalcante et al., 2013). In addition, magnetic foliations and lineations reveal a complex flow field, characterized by a western and an eastern domain. The western domain comprises gently dipping foliations bearing lineations that progressively rotate from SW in the south to NW in the north. The eastern domain is dominated by subvertical NS-trending foliations bearing subhorizontal orogen-parallel lineations. This pattern is interpreted as the result of the combination of convergence and gravity-driven forces that promoted a ‘channel flow like’ tectonic behavior (Cavalcante et al., 2018).

IV.3. THE CENTRAL PLUTONIC UNIT

IV.3.1. The imbricated synkinematic magmatic São Vitor Tonalite and metasedimentary host rock

The CPU involves huge volumes of magmatic rocks emplaced within metasediments. The main magmatic bodies of this domain in the studied area are represented by the São Vitor and Galiléia tonalites (Fig. 21B). The former is grey in color, medium to coarse-grained, exhibiting inequigranular phaneritic texture and magmatic foliation marked by the preferential alignment of biotite and feldspar. Elongate mafic enclaves that are parallel to the magmatic foliation are also observable (Fig. 22A). The primary mineralogy is composed of plagioclase, quartz, microcline, and biotite. Zircon is a common accessory, included in biotite crystals. Garnet, muscovite, chlorite, and epidote are present in small amounts. The composition varies from tonalite to granodiorite. Plagioclase is euhedral to subhedral and partially sericitized, biotite is well oriented (Fig. 23A) and the quartz interstitial. K-feldspar often shows myrmekite and do not display evidence of ductile deformation. In addition, the presence of large subhedral and anhedral quartz grains preserving an interstitial morphology (Fig. 23B) attest that the fabric is magmatic.

The Galiléia Tonalite outcrops in the southern portion of the study area (Fig. 21B) and consists predominantly of medium-grained tonalites, granodiorites, and subordinate granites, that are either granular or porphyritic. Amphibole and garnet are more abundant in the São Vitor than in the Galileia tonalite (Mondou et al., 2012; Narduzzi et al., 2017). Foliation is defined by the orientation of biotite and amphibole crystals and marked by stretched mafic enclaves. Previous studies by Mondou et al. (2012) and Oliveira et al. (2008) also confirm that the fabric is magmatic, attested by interstitial quartz morphology, and absence of solid-state deformation features.

The host metasediments (Fig. 22B) represented by the Tumiritinga Formation (Rio Doce Group) in the CPU (Fig. 21B) are chiefly biotite schists and feldspar-rich schists and gneisses with common intercalations of calc-silicate rocks. The texture is commonly granolepidoblastic marked by fine-grained quartz, feldspar, and biotite crystals. The mineralogy of the schists and gneisses is composed of quartz, plagioclase, biotite, garnet, sillimanite, K-feldspar, muscovite, and traces of zircon and apatite. A compositional banding marked by quartz-rich bands interlayered with mica-rich bands is commonly observed. The schists frequently present anastomosed foliation around garnet and feldspar porphyroblasts

and porphyroclasts. Medium coarse-grained euhedral to subhedral hornblende crystals defining a nematoblastic texture features in the calc-silicate lenses. Undulose extinction, formation of subgrains, and sharp contacts with stretched biotite (Fig. 23C and D) are common features observed in quartz crystals and indicate the solid-state fabric of the partially melted metasediments.

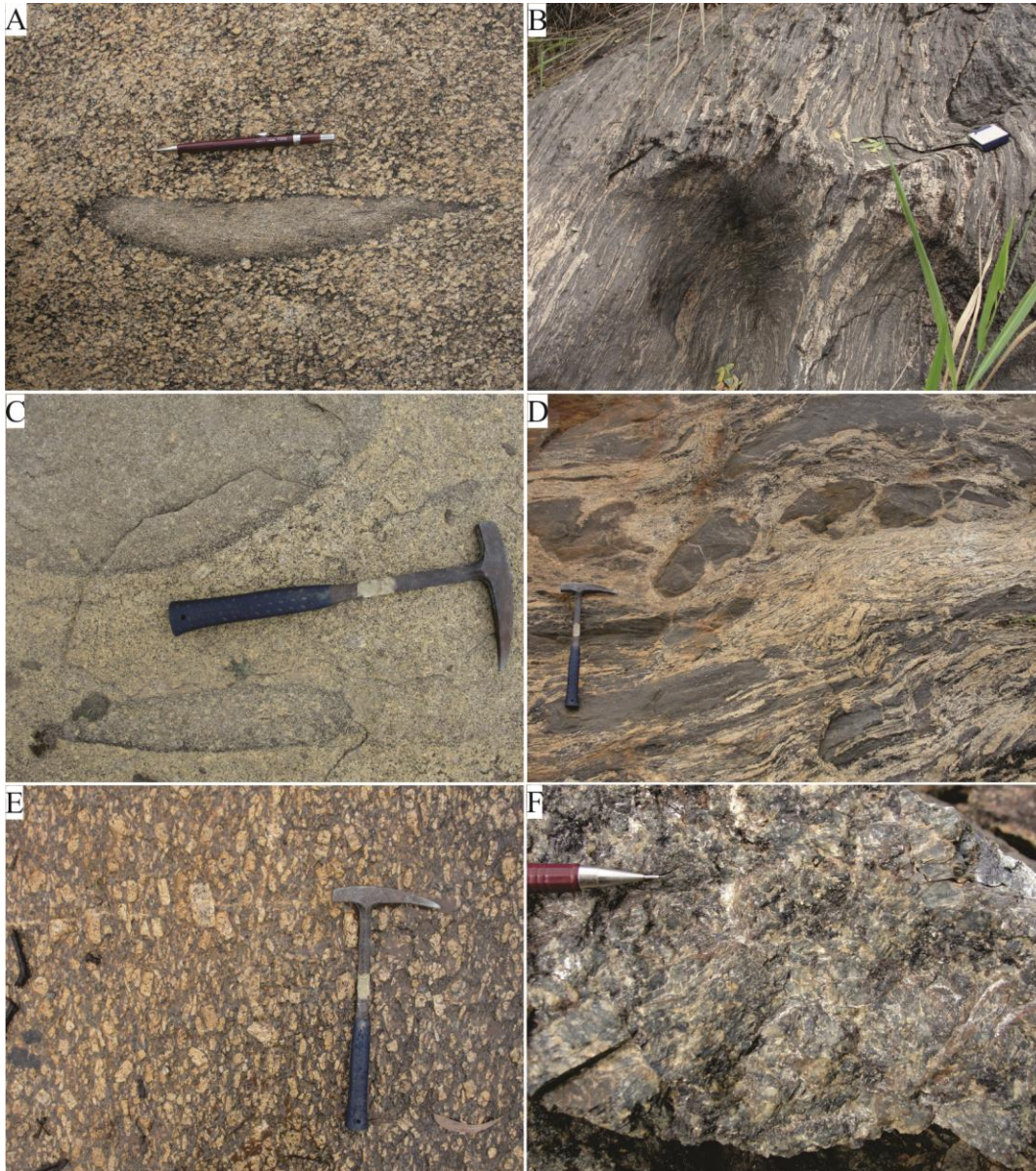


Fig. 22. Typical outcrops sampled in this study. A: typical outcrop of the São Vitor Tonalite displaying well-developed magmatic foliation marked by the preferred orientation of plagioclase and biotite and by elongated mafic enclave B: host metasediments of the Tumiritinga Formation displaying steeply-dipping foliation planes. C: magmatic fabric of the Guarataia Granodiorite marked by preferential alignment of K-feldspar and plagioclase and elongate enclaves of mafic magma. D: migmatite from the Mantiqueira Complex, showing gneissic foliation that is associated with melt extraction texture and schollen structure represented by large blocks of melanosome. E: magmatic flow evidenced by K-feldspar megacrysts, plagioclase, and biotite of the Caladão Granite F: Padre Paraíso Charnockite – nonfoliated, dominantly medium grained hornblende + hypersthene charnockite.

IV.3.2. Arc western border – The Guarataia, Brasilândia and Chaves plutons and the Mantiqueira Complex (Western Mylonitic Unit)

The Mantiqueira Complex occupies the SW of the studied area and is oriented in the NE direction. The predominant petrographic type of this unit consists of medium to coarse-grained banded biotite-amphibole orthogneiss. The dark bands are constituted of garnet-amphibole-biotite, and the light bands are composed of a quartzo-feldspathic association of tonalitic to granitic composition. The thickness of the alternating band varies in centimetric scale and schollen, schlieren, and folded structures are common (Fig. 22D). Primary mineralogy in thin section is defined by plagioclase, quartz, microcline, and biotite. The texture is commonly granolepidoblastic marked by medium to coarse-grained quartz, feldspar, and biotite crystals (Fig. 23F).

The Guarataia Granodiorite is located at the southwestern portion of the studied area, discordant with the regional structural trend, cutting across the Paleoproterozoic basement (Mantiqueira Complex), Neoproterozoic metasedimentary rocks (Tumiritinga Formation) and the São Vitor Tonalite. This plutonic body features grey color, inequigranular fine- to coarse-grained texture (Fig. 23E) and evidence of magmatic foliation (Fig. 23E) marked by oriented crystals of potassium feldspar, plagioclase, biotite and elongate mafic enclaves (Fig. 22C). Plagioclase, microcline, quartz, biotite, represent the primary mineralogy. Epidote, titanite, allanite, and zircon are also present in small amounts. The Guarataia intrusion is free of regional solid-state deformation features.

Petrographic and microstructural data on the Brasilândia and Chaves Plutons are based on present observations and previous data by Tedeschi et al. (2016). The Brasilândia pluton forms a NNE-trending elongated intrusion limited by the host metasediments and the Mantiqueira Complex. This unit varies in composition from tonalite to granite with medium to coarse-grained texture. Anastomosing foliation is formed by plagioclase countoured by biotite and amphibole crystals. Plagioclase commonly presents deformation twins but also preserved oscillatory zoning, typical for magmatic crystallization. The Chaves pluton forms a NS-trending elliptical body of a predominant enderbite facies, with minor gabbro-norite, opdalite, charnockite, and biotite monzogranite facies. Foliation is marked by biotite and amphibole crystals. The contacts among the facies are characterized by hybrid zones involving mixing of rocks from two or more facies.

IV.3.2. Arc eastern border - The Aimorés Suite (emplaced in the Eastern Anatectic Unit)

The EAU (Fig. 21A) is intruded by syn- to late orogenic granite and charnockite of the Aimorés Suite (Fig. 21B). The suite comprises the Caladão Granite and the Padre Paraíso Charnockite, that cut across the regional trend, shaping the regional foliation around them. Deformation in these plutons mostly occurred in the magmatic state as supported by the preservation of a well-oriented magmatic fabric and weak solid-state reworking.

The petrographic type of the Caladão Granite varies in composition from monzo- to sienogranites, featuring a coarse-grained porphyritic texture represented by orthoclase and minor plagioclase megacrysts (Fig. 22E), inserted in a fine to medium matrix of quartz, biotite, microcline, and garnet. Orthoclase is sometimes euhedral to subhedral; they often show myrmekite. Plagioclase occasionally presents slightly deformed twinning lamellae. Quartz grains occasionally display interstitial shapes and in some cases form chessboard-like patterns and undulose extinction (Fig. 23G). Biotite crystals are subhedral, euhedral and acicular, often showing a well-preferred orientation. Anhedral garnet crystals show evidence of poikilitic texture containing quartz, plagioclase, and biotite.

The Padre Paraíso Charnockite exhibits a gradational contact with the Caladão Granite, marked by the appearance of hypersthene. This lithotype is greyish green in color, medium to coarse-grained, presenting a porphyritic texture (Fig. 22F) represented by K-feldspar and plagioclase megacrysts in a matrix composed of quartz, biotite, hypersthene, and hornblende. Accessory minerals are apatite, zircon, chlorite, and carbonate. Interstitial quartz is a common feature in the charnockite, Pressure shadows or recrystallization tails are absent around feldspars, which present irregular boundaries. These features suggest magmatic state deformation (Fig. 23H).

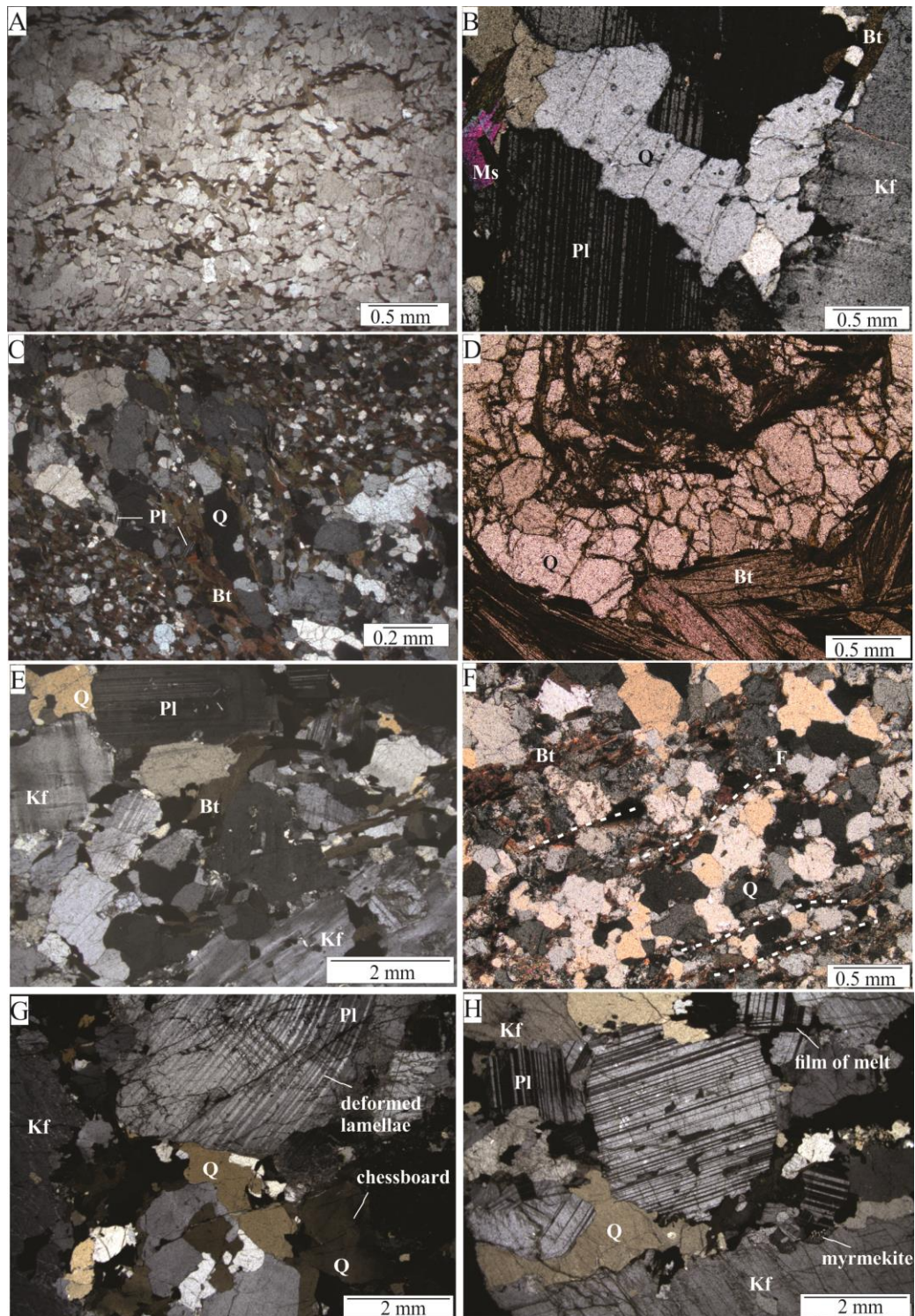


Fig. 23. Petrographic and microstructural aspects of the sampled lithological units. Well development of magmatic foliation with biotite alignments (A) and interstitial quartz grains with irregular and curved boundaries (B) of the São Vitor Tonalite. Solid-state deformation is observed in host metasediments of the Tumiritinga Formation. Anastomosed foliation (C) marked by quartz ribbons with wavy extinction and with sharp contacts with oriented biotite crystals and locally bent recrystallized quartz bands interlayered with lepidoblastic bands (D). Magmatic textures are observed in the Guarataia Granodiorite (E) showing interstitial quartz and magmatic flow marked by feldspars and biotite. Development of polycrystalline quartz ribbons (F) between foliation 'F' marked by biotite crystals in migmatite of the Mantiqueira Complex, evidencing solid-state deformation. Caladão Granite displaying local HT solid-state features with a chessboard-like pattern in quartz and deformation twins in plagioclase (G). Padre Padraiso Charnockite showing magmatic texture, myrmekite and melt films that crystallized to quartz along grain boundaries of feldspars (H).

IV.4. ANISOTROPY OF MAGNETIC SUSCEPTIBILITY (AMS)

AMS can be used to measure the petrofabric of rocks to determine the preferred orientation of magnetically-dominant minerals, and is commonly used as an effective approach for studying plutonic and metasedimentary rocks because it provides magmatic strain patterns in rocks where macroscopically visible planar and/or linear structures are difficult to characterize (Tarling and Hrouda; 1993; Martín-Hernández et al., 2004). The AMS can be described by a symmetrical second rank tensor (K_{ij}) that relates the intensity of the externally applied magnetic field (H_j) and an object's corresponding induced magnetization (M_i) through the equation $M_i = K_{ij} H_j$. The magnitude ellipsoid can be described by the minimum ($K_{\min} = K_3$), intermediate ($K_{\text{int}} = K_2$), and maximum ($K_{\max} = K_1$) axes of susceptibility, being their average, the mean susceptibility (K_m) (Hrouda, 1982; Borradaile and Jackson, 2010). The maximum susceptibility direction (K_1) is regarded as the magnetic mineral lineation, and the minimum susceptibility direction (K_3) is a proxy of the pole of the magnetic foliation.

When K_m is carried by Fe-bearing silicate paramagnetic matrix minerals the AMS is defined by the preferred mineral crystallographic orientations, described as magnetocrystalline anisotropy (Hrouda, 1982). On the other hand, when K_m is governed by cubic ferromagnetic minerals such as magnetite, the AMS is controlled by grain shape (Borradaile and Henry, 1997).

The magnitude of these principal axes is used to calculate different parameters (Jelinek, 1981; Tarling and Hrouda, 1993) that define the anisotropy of magnetic susceptibility. We used the mean susceptibility K_m , given by $(K_1 + K_2 + K_3)/3$; the degree of magnetic anisotropy ($P' = K_1/K_3$), the shape parameter T , where $T = [2 (\ln K_2 - \ln K_3)/(\ln K_1 - \ln K_3) - 1]$, F as the magnitude of the magnetic foliation ($F = (K_2 - K_3)/K_m$), and L of the lineation ($L = (K_1 - K_2)/K_m$). The parameter P' is a measure of the eccentricity of the AMS ellipsoid, where $P' = 1$ represents a sphere. The shape of the ellipsoid is represented by T . The value of T lies between -1 and +1; positive values indicate oblate, while negative ones prolate shapes.

The K_m is a simple measure of a fundamental magnetic response characteristic of a sample. Bulk susceptibility values below $5 \cdot 10^{-4}$ SI have a paramagnetic behavior; between $5 \cdot 10^{-4}$ and $50 \cdot 10^{-4}$ SI represent a mixed contribution of paramagnetic and ferromagnetic fractions; and above $50 \cdot 10^{-4}$ have a ferromagnetic behavior (Tarling and Hrouda, 1993).

However, according to Trindade et al. (1999), the correlation between bulk susceptibility and magnetic behavior must be considered with caution, since ferromagnetic and paramagnetic materials may both have low bulk susceptibility values.

In the present study, the low-field magnetic susceptibilities and its anisotropy were measured using a Kappabridge instrument (KLY-4S, Agico, Czech Republic) housed in the Paleomagnetism Laboratory of the University of São Paulo, Brazil. The AMS parameters were computed using Aniso software version 4.2 (Jelinek, 1978). Oriented samples were extracted at 19 sites (appendix A and D) using a portable gasoline-powered rock drill, among which 5 are in the Guarataia granodiorite, 1 in the São Vitor Tonalite, 6 in the Caladão granite, 5 in the Padre Paraíso Charnockite, 1 in the metasediments of the Tumiritinga Formation, and 1 in the Mantiqueira Complex between the metasediments and the Brasilândia tonalite (TM code). Between 4 to 9 oriented cores were drilled in each site. The cores were cut into cylindrical specimens with 2.5 cm in diameter and 2.2 cm in height, the standard for magnetic measurements. A total of 395 specimens were obtained. In addition, compiled data from previous studies (Portela, 2013; Sanchez, 2014; and Pinto, 2015; codes BP, TFE, and TFN, respectively) were also utilized in the present study. Oriented samples were obtained from 14 outcrops, 9 from the São Vitor tonalite and 6 from the Tumiritinga Formation. The drilling and preparation procedures also obeyed the standards for AMS measurements. Data from 205 specimens were collected from these previous studies, giving a total of 600 specimens for this present work (Table 1).

Table 1. Anisotropy of Magnetic Susceptibility database for the study area. Samples TFE, TFN, and BP are AMS measurements from previous studies (references in the text).

Site	UTM		Mean AMS Parameters				Mean eigenvectors				
	X (W)	Y (S)	Km x10 ⁴ (SI)	P'	T	dec/inc	e1/e2	dec/int	e1/e2	dec/inc	e1/e2
Guarataia Granodiorite											
TM01	204523	7976017	13	1.107	0.733	152.6/49.7	27.6/8.0	20.6/29.6	27.6/16.0	275.4/24.7	16.1/8.1
TM02	203472	7976338	6.9	1.104	0.327	77.9/42.4	30.2/10.7	172.7/5.2	30.9/14.8	268.4/47.1	17.0/11.1
TM03	202738	7976439	25.1	1.118	-0.230	76.3/46.8	19.2/17.1	174.1/7.3	25.5/18.2	270.7/42.3	25.2/17.5
TM04	200548	7975713	12.6	1.115	0.416	59.3/25.7	28.8/10.8	329.1/0.4	28.8/14.3	238.2/64.3	15.1/9.5
TM45	193464	7977203	27.1	1.279	0.553	81.3/23.0	28.3/5.0	351.1/0.4	28.3/4.5	260.1/67.0	5.2/4.5
Tumiritinga Formation											
TM47	189786	7980246	3.11	1.065	0.092	15.5/19.6	17.1/9.8	268.6/39.3	29.2/13.0	125.8/44.3	29.4/13.1
TFE01	213539	8004677	2.93	1.117	-0.625	204.9/26.5	8.1/2.8	296.8/3.9	22.7/7.0	34.7/63.2	22.4/3.1
TFE02	212728	8004932	5.34	1.108	-0.22	204.4/41.7	1.9/0.7	89.5/25.3	9.6/0.5	338.1/37.8	9.5/1.1
TFE06	206441	8005165	4.76	1.084	0.511	178.7/77.1	29.9/3.6	34.1/10.6	29.9/13.5	302.7/7.3	13.7/3.6
TFE07	201926	8006391	3.05	1.063	0.292	53.7/7.0	16.3/12.5	152.2/50.3	17.8/15.9	318.0/38.8	19.7/8.1
TFE11	211767	8001265	3.11	1.104	-0.444	190.0/28.6	6.6/3.5	92.5/13.5	8.8/6.0	340.0/57.8	9.3/2..8
TFE12	211279	8000461	3.97	1.093	0.392	178.8/27.5	24.5/7.0	292.0/37.1	24.5/10.8	62.3/40.6	11.8/5.9
Caladão Granite											
TM21	263148	7999926	1.53	1.052	0.720	255.8/1.1	29.3/8.7	165.4/22.2	28.8/7.8	348.5/67.8	10.9/7.3
TM22	265612	7998241	308	1.123	-0.291	292.5/19.3	20.2/7.4	174.6/53.2	22.2/14.5	34.2/30.0	18.6/8.3
TM31	269335	8014136	3.06	1.058	0.677	273.0/38.6	27.0/9.0	177.1/7.3	28.2/10.8	78.2/50.5	15.2/8.6
TM36	265512	8006815	4.44	1.038	0.149	245.3/14.1	28.1/18.2	344.2/31.7	27.9/27.5	134.7/54.7	29.2/16.1
TM40	265849	8006119	10.4	1.069	0.744	259.7/37.2	29.4/6.8	1.0/14.5	29.3/7.1	108.4/49.1	8.1/6.7
TM42	266091	8003275	3.18	1.033	0.104	273.1/52.3	30.0/15.1	115.6/35.4	30.0/11.1	17.7/11.0	15.6/11.6
Padre Paraíso Charnockite											
TM32	268359	8010619	7.96	1.033	0.187	213.0/47.3	29.2/15.0	313.1/9.2	29.3/20.5	51.3/41.2	23.5/9.2
TM37	264545	8006999	5.09	1.022	0.110	229.6/21.3	28.5/10.7	332.7/30.2	28.7/19.0	110.0/51.7	19.4/10.5
TM38	264294	8005048	22.1	1.057	0.019	246.8/34.8	20.3/17.3	339.8/4.3	30.0/19.3	76.0/54.9	30.4/17.6
TM39	262960	8004596	7.13	1.062	0.376	171.6/20.6	24.0/15.4	266.7/13.6	30.0/21.4	28.8/65.5	29.9/16.5
TM43	262350	8001471	73.5	1.110	0.527	235.9/13.5	18.3/7.5	326.9/4.1	17.8/4.8	73.4/75.9	9.0/4.5
São Vitor Tonalite											
TM11	222160	8007376	2.38	1.118	-0.149	211.7/6.6	10.6/2.9	334.5/78.0	4.6/2.8	120.5/10.0	10.8/3.8
BP01	214807	7973822	0.692	1.082	0.171	10.7/30.6	15.0/12.5	108.0/12.1	27.1/13.9	217.1/56.6	28.8/8.0
BP02	233013	7976944	2.76	1.043	-0.14	175.3/27.8	6.1/3.1	27.1/58.2	22.8/4.8	273.0/14.2	22.8/4.7
BP03	215223	7973833	1.35	1.13	0.656	155.4/3.9	28.0/10.4	62.9/32.5	29.6/10.1	251.5/57.2	15.8/10.7
BP04	227220	8003074	1.36	1.102	0.444	42.3/18.9	11.5/4.4	177.0/64.0	8.1/5.0	306.3/17.1	11.6/4.4
TFN04	228368	7996224	2.792	1.106	-0.134	197.2/18.6	13.9/6.7	103.3/11.6	23.3/13.6	343.0/67.8	23.2/6.8
TFN06	225096	7984445	3.13	1.07	0.04	360.0/2.8	27.0/8.9	91.4/27.8	21.1/16.0	264.8/62.1	25.0/19.6
TFN07	226997	7984502	3.62	1.038	0.375	93.5/22.1	27.9/14.8	191.4/18.7	27.9/18.1	318.0/60.4	20.6/0.9
TFN08	234955	7979634	0.894	1.114	0.507	180.0/29.9	22.9/9.6	307.7/46.8	23.5/7.6	72.3/28.0	10.7/9.7
TFN09	234816	7979676	1.12	1.107	0.518	163.7/8.1	28.8/13.9	264.3/52.2	28.8/11.8	67.6/36.6	16.8/11.6
Mantiqueira Complex											
TM25	191853	7967086	3.55	1.087	0.215	334.8/24.6	17.5/4.5	174.3/64.2	19.0/15.4	68.3/7.6	17.7/4.4

IV.4.1 The AMS and macrostructural fabrics

The site mean values of degree of anisotropy P' varies from 1.022 up to 1.279 (Fig. 23A and D), with an average value of 1.088. The shape parameter T differs from -0.625 up to 0.744 (Fig.18B), with an average of 0.224. The site mean anisotropy degree (P') versus site

mean shape parameter (T) plot shows that most sites are oblate ($T > 0$), indicating a well-defined foliation plane (Fig. 24B). The site mean magnetic susceptibility K_m changes between 0.692×10^{-4} and 3.08×10^{-2} SI (Fig. 24C), with twenty-one sites showing values lower than 5×10^{-4} SI (Fig. 24A and C) suggesting a dominant effect of paramagnetic minerals controlling the susceptibility and anisotropy of the samples. Two sites sampled in the Padre Paraíso Charnockite and Caladão Granite have K_m values higher than 50×10^{-4} SI (Fig. 24A and C), indicating that both susceptibility and anisotropy of these rocks are primarily carried by the ferromagnetic fraction. Both the paramagnetic and ferromagnetic fractions (mixed contribution) might exert the control on susceptibility and anisotropy in eleven sample sites (Figure 24A and C), which presented values of K_m in the range of 5×10^{-4} to 50×10^{-4} SI (Tarling and Hrouda, 1993).

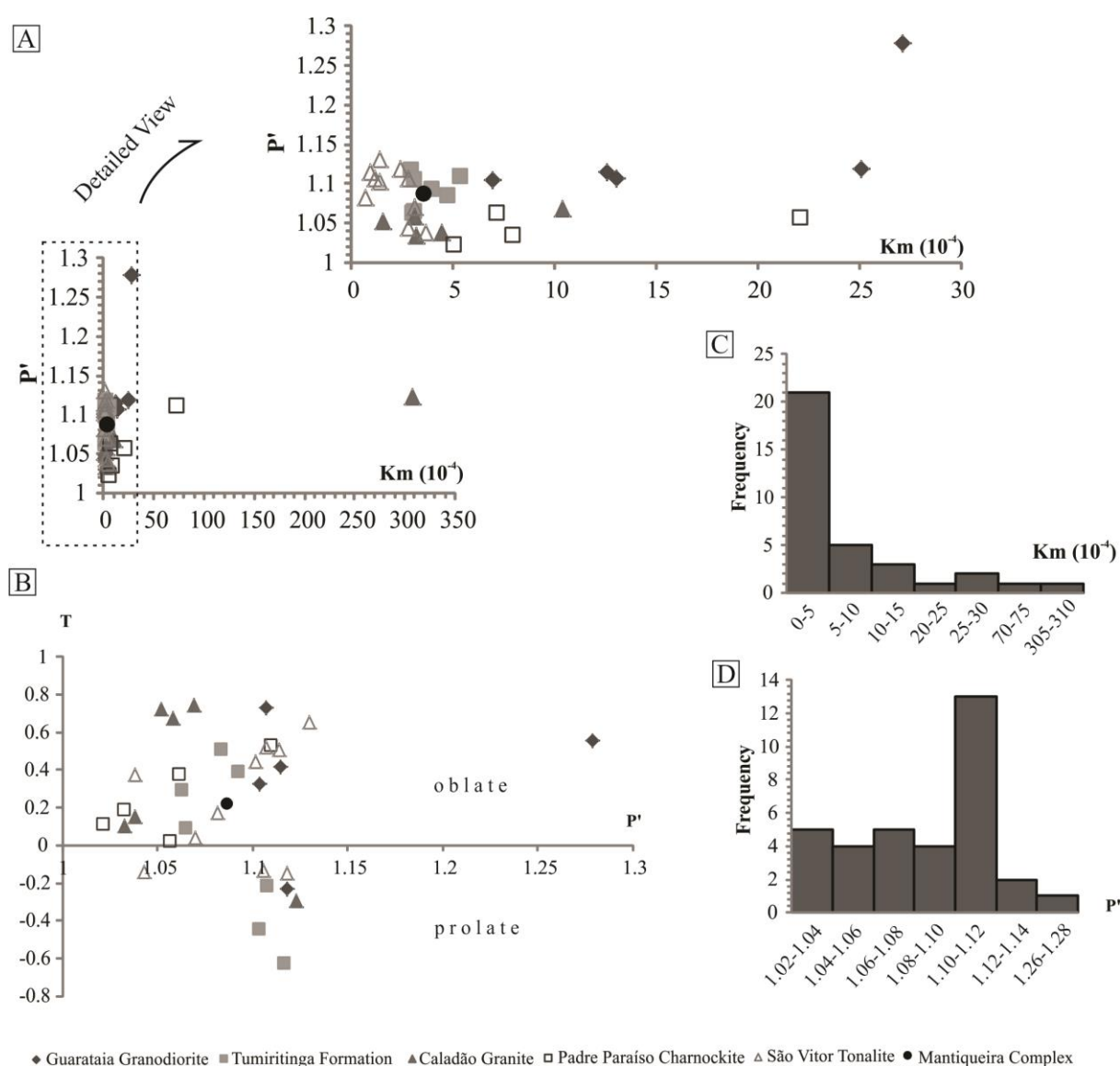


Fig. 23. Anisotropy of Magnetic Susceptibility scalar data of the samples collected for this study. A: Shape factor (T) versus P' . B: P' versus K_m plot. C: K_m frequency histogram. D: P' frequency histogram.

The studied area has been subdivided into four distinct structural regions according to the foliations and lineations deduced from the AMS (Table 1 and Fig. 25) and field measurements (Fig. 26), each of these representing a predominant tectonic regime.

Region 1 is localized in the westernmost part of the studied area, and it is characterized by a transition of tectonic regimes. The field measurements in the metasedimentary rocks of the São Tomé Formation (compiled from Oliveira et al., 2000) show an orogen-parallel ~NS foliation gently dipping eastward bearing a down-dip mineral lineation. Eastward, dip angles remain constant, but the foliation direction shifts to the northeastern direction and the associated lineation progressively becomes sub-horizontal and parallel to sub-parallel to the orogenic strike. AMS measurements for region 1 (Fig. 25A and 26) show eastward gently dipping foliation with a roughly NS strike direction bearing gently plunging lineations to the east, which shifts to sub-horizontal ~NS orientation.

Region 2 is predominantly marked by NNE-trending steeply-dipping foliation planes bearing a sub-horizontal lineation. The K_3 axes and the field foliation measurements are well grouped and thus define a well-constrained fabric (Fig. 25B and C). Magnetic and field foliation data in the host metasedimentary rocks of the Tumiritinga Formation are similar to the São Vítor Tonalite in this domain. The field lineation measurements, however, are more variable and commonly ranges from sub-vertical to sub-horizontal. On the other hand, the magnetic lineation is well defined, showing consistent NNE orientation with shallow plunges (Fig. 26).

Field measurements for region 3 are predominantly marked by steeply to gently dipping eastward NS-trending foliation, occasionally dipping westward. The field lineation is relatively scattered but one can observe a tendency in the NS orientation associated with shallow plunges that frequently shifts to sub-vertical (Fig. 26). Westward sub-vertical dipping NS-trending magnetic foliation (Fig. 26) dominates in region 3 and bears a NS-oriented sub-horizontal magnetic lineation (Fig. 25D and E). Eastward gently dipping magnetic foliations are also observed, but less frequently (Fig. 25E). All AMS measurements in this region are situated in the São Vitor Tonalite.

Region 4 is mainly characterized by westward gently dipping NE-trending magnetic foliation bearing down-dip magnetic lineation (Fig. 25F, G and H). The AMS measurements are chiefly situated in the Caladão Granite and the Padre Paraíso Charnockite in the northern portion of this sector. Field measurements (Fig. 26) are relatively scattered, showing a

concentration of gently dipping NE and NW-trending foliation planes. Dominantly sub-horizontal NS-trending field lineation sporadically variates orientation, trending NW and E-W, with a minority of measurements with sub-vertical plunges.

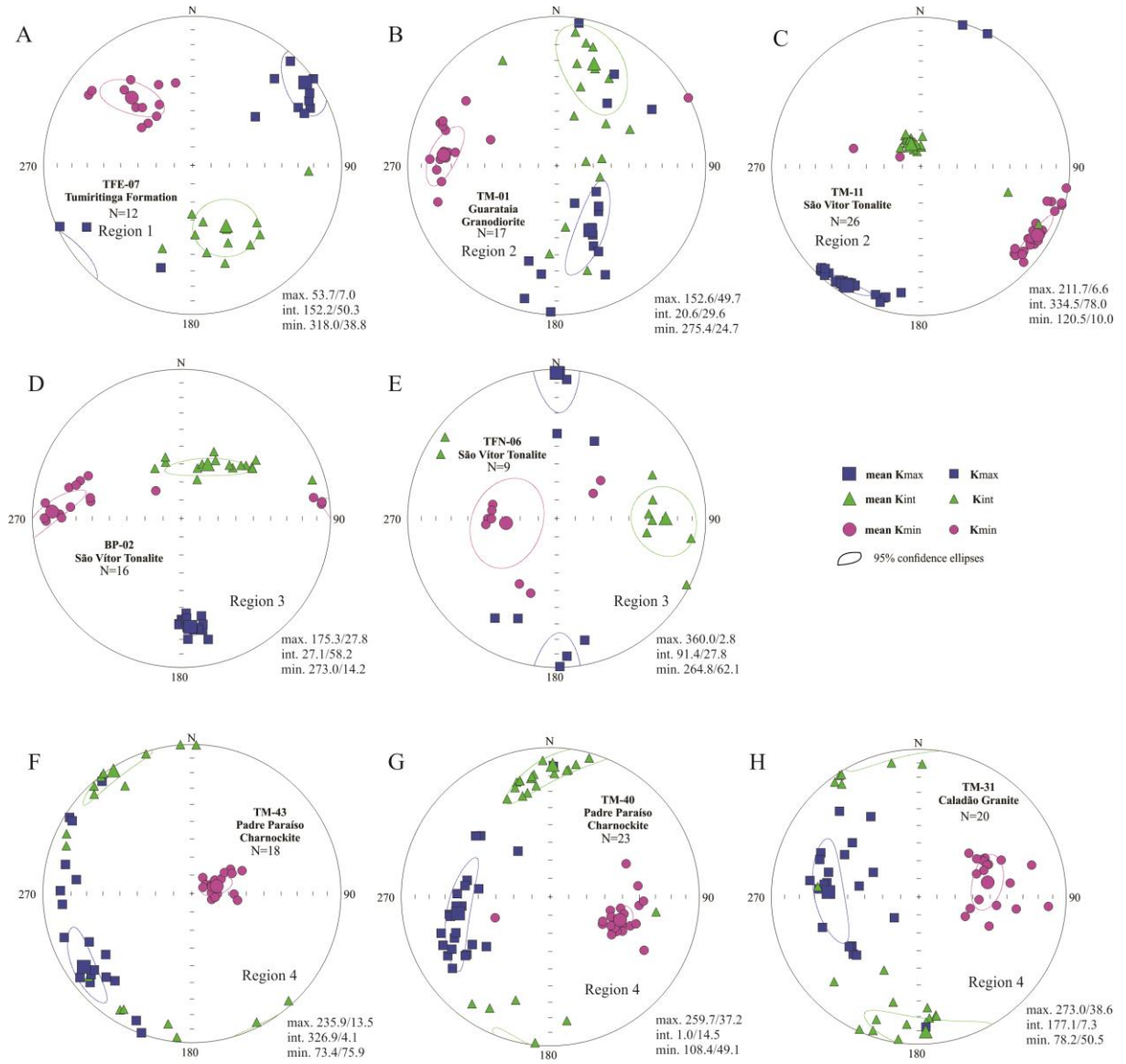


Fig. 25. Representative diagrams of the magnetic fabrics determined from AMS for the studied region. Plots are equal lower hemisphere, equal area projection. A (region 1): gently southeastward-dipping bearing a sub-horizontal lineation of the Tumiritinga Formation. B and C (region 2): sub-vertical orogen-parallel foliation with sub-horizontal to gently plunging lineation. D and E (region 3): São Vitor tonalite sites showing N-S vertical and shallow eastward dipping foliation with sub-horizontal lineation. F, G and H (region 4) show sub-horizontal foliation bearing a sub-horizontal to gently plunging-westward lineation.

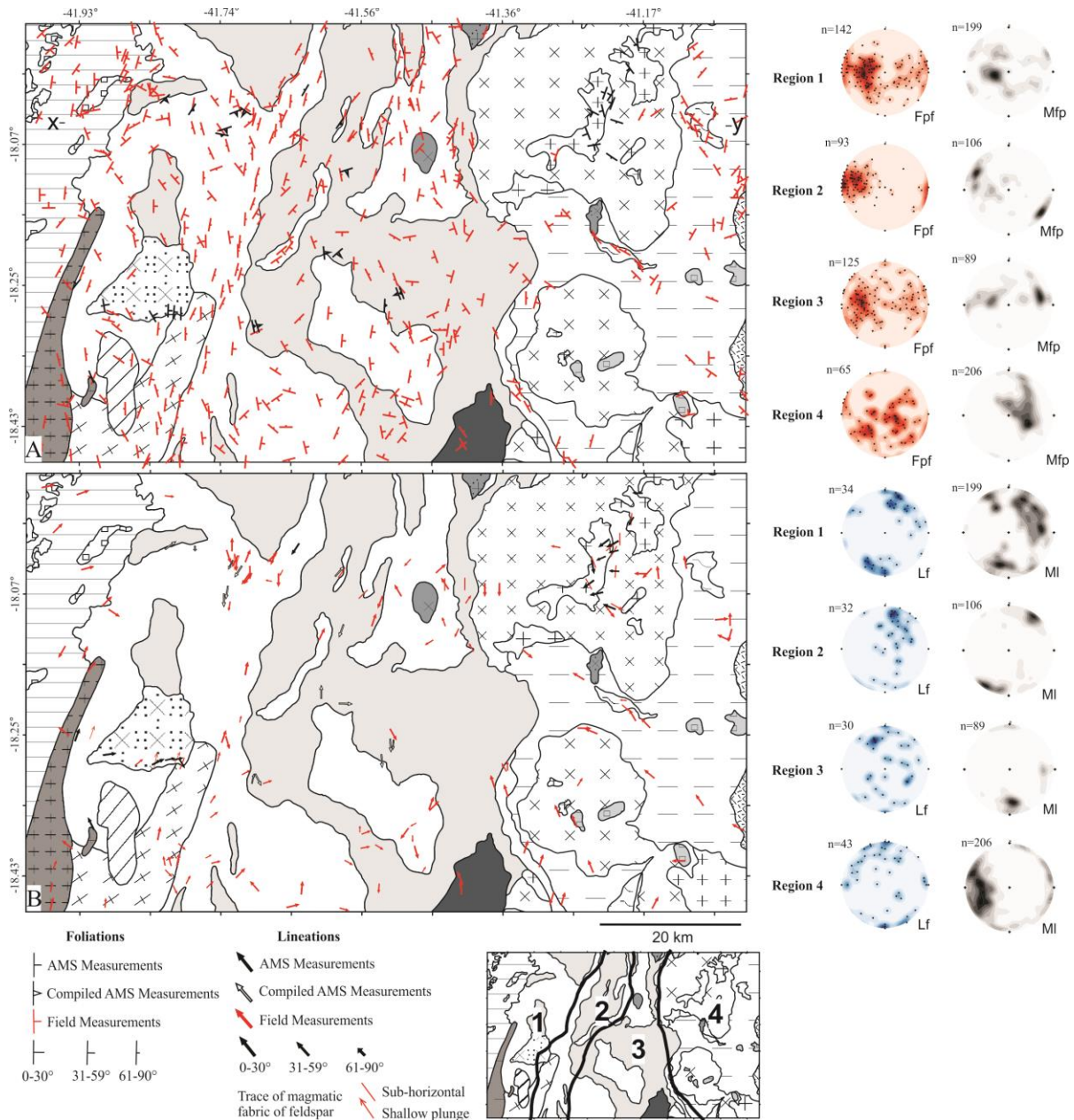


Fig. 26. Map showing AMS and field foliation and lineation measurements across the study area. The inset map in the inferior right corner shows the 4 structural regions of the study area defined by their foliation patterns. A: Foliations map and stereoplots for each structural region representing the foliation poles measured in the field (red stereoplots) and obtained from AMS measurements. B: Lineations map. The stereoplots for each structural region illustrate the lineations measured in the field (blue stereoplots) and obtained from AMS. Field measurements were obtained from this study (trace of magmatic fabric of feldspar) and compiled from Signorelli (2000), Paes (2000), Moreira (2000), and Tuller (2000). Compiled AMS measurements refer to Portela (2013), Sanchez (2014), and Pinto (2015). Fpf and Lf: foliation poles and lineations from the field measurements. Mfp and MI: magnetic foliation poles and magnetic lineations from the AMS measurements. X-Y = location of the cross section of Fig. 11.

IV.4.2 Magnetic mineralogy investigation

A detailed magnetic mineralogy study is necessary to determine the contribution of mineral phases to the magnetic susceptibility, in order to determine geological significance of the AMS results. Magnetic fabrics can be hosted by ferro-, ferri-, para-, or diamagnetic

phases. These classifications and the grain-size determine the significance of the observed fabric. Fabrics are also influenced by the domain state of some minerals (Ferré, 2002; Guerrero-Suarez and Martin-Hernández, 2016).

Magnetic domains in ferro- and ferrimagnetic phases cause the magnetic susceptibility to be shape and volume dependent: single-domain (SD) magnetite has an inverse magnetic fabric where the susceptibility axes are exchanged; however, this is not the case for multi-domain (MD) or pseudo-single domain (PSD) magnetite (and/or paramagnetic phases biotite and amphibole; Archanjo et al., 1995; Bouchez, 1997; Launeau and Cruden, 1998) which leads to direct magnetic fabrics. MD or PSD magnetite grains are larger enough for the AMS ellipsoid to correspond to the shape ellipsoid and can be interpreted as consistent with the petrofabric. Coexistence of SD (>20%) and MD magnetite particles within the rock might lead to intermediate fabrics, affecting potential interpretations (Stephenson et al., 1986; Hrouda and Ježek, 2017).

We performed magnetic mineralogy investigations using thermomagnetic curves (K-T curves, Fig. 27A), hysteresis loops (Fig. 27B), isothermal remanent magnetization (IRM) curves (Fig. 27C), and First-Order Reversal Curve diagrams (FORC, Fig. 28) on representative samples of the six different types of rock units of this study: São Vitor Tonalite, Guarataia Granodiorite, Caladão Granite, Tumiritinga Formation, Padre Paraíso Charnockite, and Mantiqueira Complex.

The low-field thermomagnetic curves were measured at low- and high-temperature using powdered samples in an Ar atmosphere CS-3 apparatus coupled to the KLY-3 bridge instrument. Each sample was submitted to continuous heating and cooling cycles from -200°C up to 700°C using a CS-L cryostat and CS-4 furnace coupled to a Kappabridge KLY-4S susceptibility meter (Agico) (Fig. 27A). Hysteresis loops, IRM acquisition curves, and FORC (Fig. 27B, C, and Fig. 28) were measured at the Oceanographic Institute of the University of São Paulo (Geoprocessing Laboratory – LabGeo) using a MicroMag 3900 (Princeton Measurements Corporation) vibrating sample magnetometer (VSM) at room temperature. The applied fields for the three methods were up to 1T (more details in Appendix C). Hysteresis loops allow determining saturation magnetization (M_s), saturation remanent magnetization (M_{rs}), and coercivity (H_c). The relationship between the induced magnetization (M) and the applied field (H) is S-shaped for ferromagnetic samples and linear for paramagnetic samples (Dunlop and Özdemir, 1997; 2009). The IRM curves provide information on the acquisition

capacity of magnetization remaining at room temperature of the ferromagnetic minerals and provide the coercivity of remanence (H_{cr}). Finally, the FORC measurements allow distinguishing between single-domain (SD), multi-domain (MD), or pseudo-single domain (PSD) magnetic grains.

Thermomagnetic K-T curves for the samples of the host metasediments represented by the Tumiritinga Formation (TM47A4), São Vitor Tonalite (TM11B2), and Mantiqueira Complex (TM25D2) show a constant drop of susceptibility with increasing temperature without any indication of Morin or Verwey transitions up to 700°C (Fig. 27A). This behavior suggests a strong contribution of the paramagnetic phases to the bulk magnetic susceptibility, probably due to Fe-bearing silicate minerals (e.g., biotite and amphibole). This is further supported by the linear relationship in the hysteresis loops (Fig. 27B) between the applied field and induced magnetic moment. The small concentration of ferromagnetic phases is supported by the acquisition of remanent magnetization showed in the S-shaped hysteresis curves in the inset graphics (paramagnetic corrected loops, Fig. 27B), and the rapid saturation of remanent magnetization between 0.1 and 0.3 T (Fig. 27C). The magnetic susceptibility of the host metasediments, Mantiqueira Complex, and São Vitor Tonalite are dominantly carried by paramagnetic minerals with a negligible contribution of ferromagnetic phases of low-coercivity, most likely magnetite. FORC diagrams for these samples do not show meaningful data since it is dominantly paramagnetic.

Thermomagnetic curves of the Guarataia Granodiorite (TM03E3), Caladão Granite (TM22G3) and Padre Paraíso Charnockite (TM38B2) samples display a characteristic Verwey transition at ca. -150°C and a strong drop of susceptibility close to the Curie temperature at 580°C (Fig. 27A). The high values of magnetic susceptibility at room temperature and its sharp increase and quick decline at the Curie temperature suggest the formation of a new mineral similar to magnetite. The lack of an extreme peak at the Curie temperature in the samples of the Guarataia Granodiorite might indicate the dominance of MD particles. A small peak at the Curie temperature is observed in the Padre Paraíso Charnockite and Caladão Granite samples before the drop of the susceptibility values and might correspond to the presence of SD or PSD domain grains (Orlický, 1990). The cooling curves exhibit a susceptibility higher than in the heating cycle revealing that new magnetic phases were produced by heating. Accordingly, magnetite grains are likely responsible for the AMS of the samples analyzed of the Caladão Granite (TM22G3), Padre Paraíso Charnockite (TM38B2), and Guarataia Granodiorite (TM03E3). This is further supported by the S-shaped

narrow hysteresis loops (Fig. 27B) indicating a ferromagnetic behavior carried by magnetite, and the steep initial slope of the IRM acquisition curves (Fig. 27C) revealing rapid acquisition of remanent magnetization that saturates between 0.1 and 0.3 T.

The FORC diagram for the Guarataia Granodiorite (Fig. 28A) shows low coercivity (B_c), vertically spread signal (B_u), and absence of a horizontally spread tail. These features all indicate MD behavior (Harrison et al., 2018). The diagrams for the Caladão Granite (Fig. 28B) and Padre Paraíso Charnockite (Fig. 28C) display an intense, closed-contour peak with broad vertical and horizontal spreading, and three weaker, less prominent lobes. These patterns indicate a PSD behavior and resemble the pseudo-single domain (“vortex”) end-member suggested by Harrison et al. (2018). Both MD and PSD behaviors of these samples are further supported by typical values in a M_{rs}/M_s versus H_{cr}/H_c (Fig. 27B) plot presented by Day et al. (1977).

Altogether, the mineralogy investigation shows that the magnetic fabric is hosted by MD and PSD magnetite, biotite, and amphibole, and the AMS data does not represent an inverse fabric. The Guarataia Granodiorite is magnetite-rich, and the AMS is preferentially controlled by MD magnetite. The magnetic fabric in the Padre Paraíso Charnockite and Caladão Granite are also dominated by magnetite, but with a magnetic behavior characterized by PSD grains. The Mantiqueira Complex, São Vitor Tonalite, and Tumiritinga Formation sites with lower values of K ($<30 \cdot 10^{-4}$ SI), display predominant paramagnetic carrier phases, where the AMS ellipsoid is controlled by biotite and amphibole crystals, present in an important amount in these rock samples.

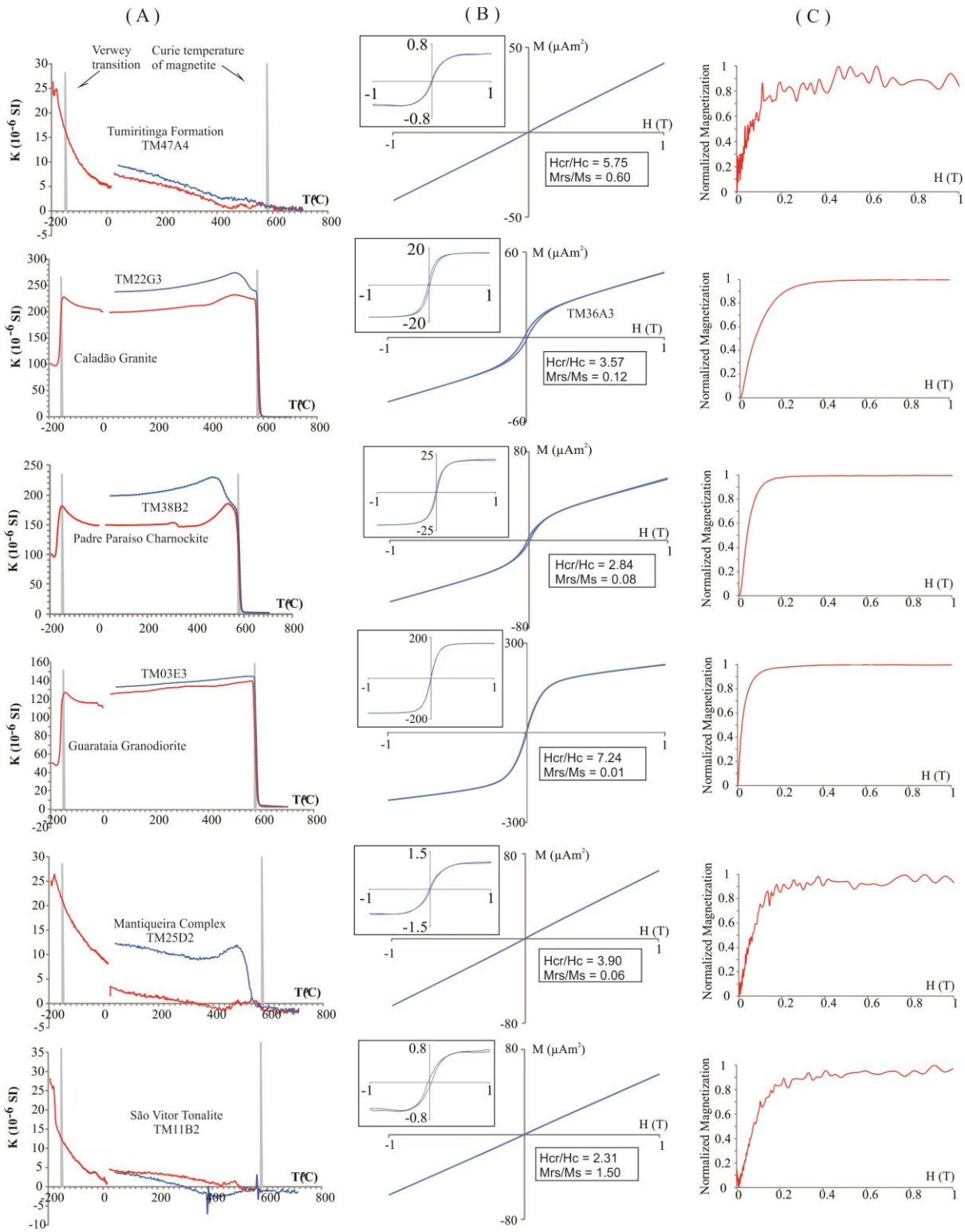


Fig. 27. Diagram showing the mineralogy investigation curves for the lithologies sampled in this study. A: Magnetic susceptibility (K) as a function of temperature (T); the interval between -200°C and 0°C corresponds to the low-temperature measurements. The solid red and blue lines in the interval between 0°C and 800°C correspond to the heating and cooling of high-temperature measurements, respectively. B: Hysteresis curves (uncorrected for paramagnetic susceptibility) and their corresponding values of saturation magnetization (M_s), saturation remanent magnetization (M_{rs}), coercivity (H_c), and coercivity of remanence (H_{cr}). Inset graphics show hysteresis loops corrected for paramagnetic susceptibility. C: Isothermal Remanence Magnetisation (IRM) curves showing the rapid increase in the acquisition of remanent magnetization that saturates in low applied fields ($H < 1T$) and detect the presence of magnetite in all samples.

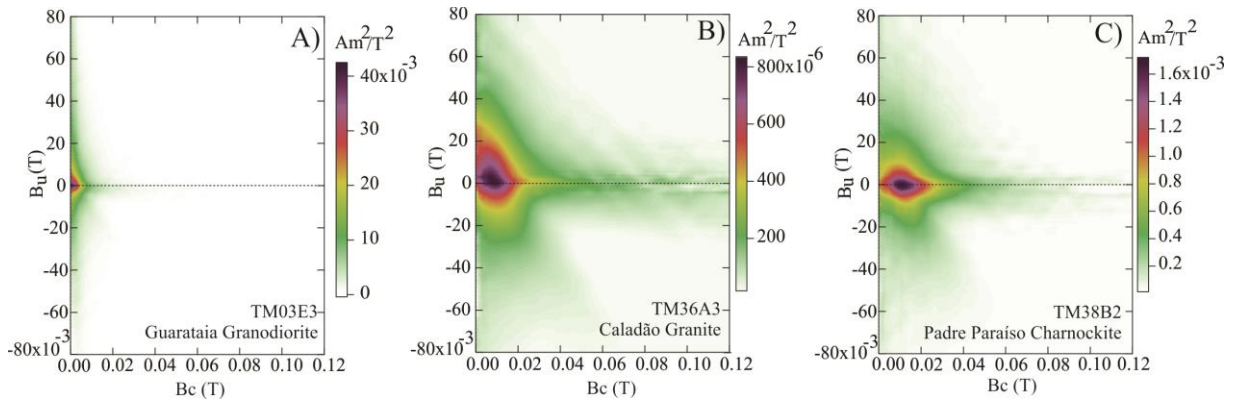


Fig. 28. First Order Reversal curves showing the predominance of multi-domain magnetite for the Guarataia Granodiorite (A); and pseudo-single domain for the Caladão Granite (B) and the Padre Paraíso Charnockite (C). The FORC diagrams of the other rock units (not shown here) contain no meaningful data since the mineralogy controlling the AMS is paramagnetic.

IV.4.3 Anisotropy of anhysteretic remanent magnetization (AARM)

Anisotropy of magnetic remanence (AMR) studies are applied as a complement to AMS measurements to evaluate whether the ferromagnetic and the matrix fabrics are coaxial (Raposo et al., 2006) isolating the contribution of remanence-bearing minerals from that of the paramagnetic and/or diamagnetic matrix (Jackson, 1991; Trindade et al., 2001; Raposo and Gastal, 2009). Moreover, remanence susceptibilities depend on grain size and this property is essentially the inverse of that of low-field susceptibility, with a maximum in the stable single-domain (SD) range, decreasing for larger multi-domain (MD) particles. One of the most common AMR methods to verify the contribution of remanence-bearing minerals to the AMS is the anisotropy of anhysteretic remanent magnetization (AARM). According to Jackson (1991), the AMR, like AMS, represents a summation over the tensors of each contributing mineral, and it is also a second-rank tensor expressed by its principal eigenvectors $A_{max} > A_{int} > A_{min}$ (respectively, K_{max} , K_{int} and K_{min}), where A_{max} corresponds to the magnetic lineation and the A_{min} is the magnetic foliation pole.

Normally, remanence anisotropy ellipsoids (AARM) are coaxial with AMS ellipsoids. However, exceptions occur where single-domain magnetite is present. Commonly, small fractions of SD magnetite reduce the symmetry and intensity of a remanence fabric dominated by larger magnetite or other remanence-bearing grains, resulting in a “blended” or perfect “inverse” fabrics if SD magnetite dominates (Ferré, 2002; Jackson, 1991; Borradaile and Henry, 1997; Borradaile and Gauthier, 2003; Raposo et al., 2006).

The AARM was determined in 6 specimens from one site of each studied lithology with AMS results (Guarataia Granodiorite, Mantiqueira Complex, Padre Paraíso Charnockite,

Caladão Granite, São Vitor Tonalite, and Tumiritinga Formation). The acquisition took place at the Paleomagnetism Laboratory at the Institute of Astronomy, Geophysics and Atmospheric Sciences of the University of São Paulo (IAG-USP), in a magnetic field-free room. Alternating field (AF) demagnetization and anhysteretic remanence acquisition were performed with a LDA-3A (Agico) demagnetizer / magnetizer and remanence was measured with a JR6-A magnetometer (Agico). To obtain the AARM tensor, the magnitude and orientation of the principal axes were obtained using a fifteen position scheme with a peak field of 80 mT and a biasing field of 100 μ T following the procedure described in Trindade et al. (2001). Before AARM measurements samples were AF demagnetized at a peak AF field of 100 mT to establish the base level. The results are presented in Fig. 29.

A good correlation between the AARM and AMS tensors is observed for the Guarataia Granodiorite (Fig. 29A), suggesting that the ferromagnetic contribution to AMS foliation and lineation is significant, also attested by the Verwey transition and the drop of susceptibility at the Curie Temperature in the thermomagnetic curve of Fig. 27A. The anisotropy carrier of this unit is MD magnetite, and the tensors are congruent, showing a steeply plunging magnetic foliation plane in the ~NS direction associated with a down-dip magnetic lineation.

The paramagnetic behavior of the São Vitor Tonalite, Tumiritinga Formation, Mantiqueira Complex (respectively in Fig. 29B, C and D) presumed in the mineralogy investigation curves (Fig 27) is also attested when comparing the principal axes of the AARM and AMS ellipsoids, which are relatively randomized. The partial correlation between the ellipsoids of these units may be due to the negligible amount of magnetite grains, supposed with the K-T and hysteresis curves (Fig. 27A and B, respectively).

The AARM fabric of the Caladão Granite and Padre Paraíso Charnockite (Fig. 29E and F) also displayed a predominant non-coaxial correlation with the AMS tensor. This non-parallelism cannot be due to the presence of single-domain magnetite since this phase was not detected in the FORC diagrams (Fig. 28B and C), which displayed the presence of PSD magnetite grains. Even though the magnetite grains in the Caladão Granite (Fig. 29E) dominate the bulk susceptibility (Fig. 27), it seems that it does not control the anisotropy of magnetic susceptibility (more details in the Discussion section). More anisotropic silicates may still express their preferred orientation through AMS fabric and PSD magnetite grains (attested in the FORC diagrams in Fig. 28B and C) are weakly oriented, and their contribution

to low-field susceptibility is not sufficiently anisotropic to deflect the AMS fabric (i.e. to become AMS parallel to AARM).

The AARM measurements of the Padre Paraíso Charnockite show a well-defined magnetic fabric (Fig. 29F), as opposed to the Caladão Granite ellipsoid. The magnetic lineation of the AARM (A_{max}) is oriented ~NS with sub-horizontal plunge. This is evidence that magnetite grains have rotated counter-clockwise from the K_{max} and the charnockite plane since K_{max} is oriented in the charnockite plane, which is oriented ~NS and gently dipping to the west.

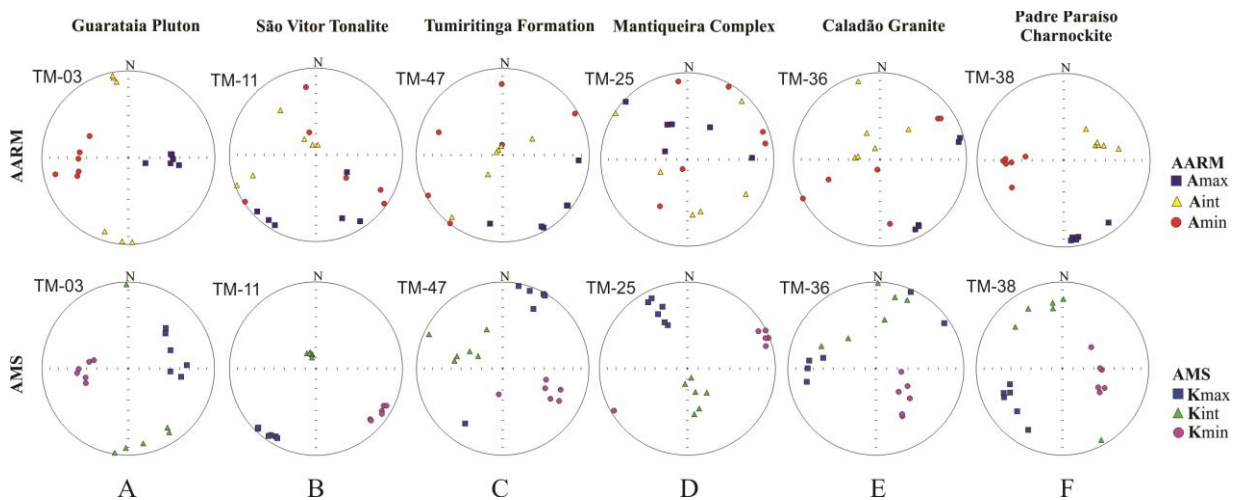


Fig. 29. Comparison of the AARM and the AMS ellipsoids. AARM ellipsoids are on the left side of each rectangle beside the AMS ellipsoids for comparison. A total of N=6 specimens of each site was measured for AARM acquisition.

IV.5. U-PB ZIRCON (LA-ICP-MS) GEOCHRONOLOGY

Integration of U-Pb age data with structural and isotopic data provides insights into a number of fundamental issues concerning batholith structure primary structure, emplacement mechanisms, and chronology and kinematics of regional deformation. The determination of whether a pluton was emplaced during a single magmatic event or resulted from multiple magmatic stages during batholith construction is important when dealing with kinematic interpretations and timing of the deformations characterized in the defined structural regions of the studied area. Thus, a new Laser Ablation Inductively Coupled Plasma Mass Spectrometry (LA-ICP-MS) U-Pb zircon age was obtained for the São Vitor Tonalite.

IV.5.1 Sampling and methods

The sample TM11 of the São Vitor Tonalite (see localization on Fig. 20B) occurs as an isolated body within the Tumiritinga Formation and due to the outcrop size ($\sim 350 \text{ m}^2$), it is too small to be shown at the scale of the map (Fig. 21B). The sample consists of medium-grained inequigranular tonalite, with plagioclase, quartz, microcline, and biotite. The zircon grains were handpicked after standard separation procedures at the Geochronological Research Center (CPGeo, Geosciences Institute, University of São Paulo, Brazil). We selected clear euhedral to subhedral grains that were mounted in epoxy. The mount was polished and the analysis of the U-Th-Pb of the zircons was conducted at the Geochronology Laboratory at the University of Brasília (UnB, Brazil), using a Finnigan Neptune couple with a Nd-YAG laser ablation system. The abundances of U, Th and Pb, and the Pb isotopic ratios were normalized using the GJ-1 zircon standard ($608.5 \pm 1.5 \text{ Ma}$; Jackson et al., 2004). More details on the instrumental operation procedures are described in Bühn et al. (2009). The data was then reduced using a spreadsheet known as Chronus (Oliveira et al., 2015), and the statistical assessments were calculated using Isoplot/Excel 3.0 (Ludwig, 2003). Finally, selected zircon grains (Fig. 30A) were imaged using back-scattered electron (BSE) using a scanning electron microscope. The results are presented in Table 2.

IV.5.2 Results

Zircon grains from the São Vitor Tonalite are long to short prisms (Fig. 30A) showing oscillatory zoning. $^{232}\text{Th}/^{238}\text{U}$ ratios vary from 0.067 to 0.899, with an average value of 0.306, indicating magmatic crystallization (Hoskins and Schaltegger, 2003; Xiang et al., 2011; Kirkland et al., 2015). From a total of 100 analyses, 33 spots more than 96% concordant yielded rather homogeneous results, as shown in the cluster on the Concordia curve (Fig. 30C), defining an upper intercept at $584 \pm 17 \text{ Ma}$ (MSWD = 0.43). However, the ages spread over the concordia for ca. 80 Ma (620-540 Ma). The weighted average $^{206}\text{Pb}/^{238}\text{U}$ calculated by Isoplot (Fig. 30B) is $567.6 \pm 4.8 \text{ Ma}$ (at 95% confidence) with a high MSWD (7.2). A total of 4 analyses with ages from ca. 891 to ca. 1977 Ma are interpreted as inherited zircons (Fig. 30A) and were not used in age calculations.

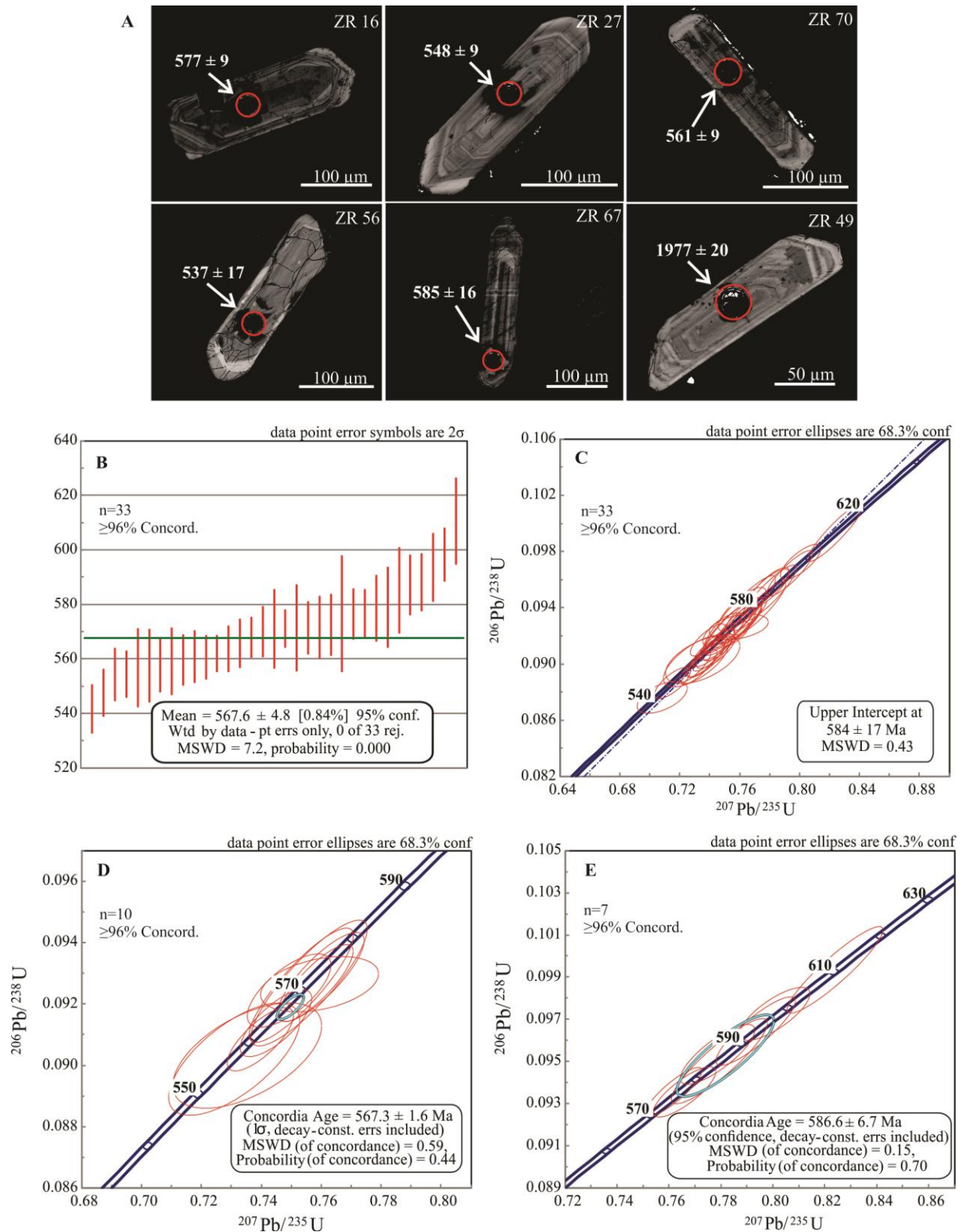


Fig. 30. A: Backscattered electron images of representative zircons from sample TM11. Oscillatory zoning typical of magmatic zircons is visible. B: Weighted average of $^{206}\text{Pb}/^{238}\text{U}$ of dated zircon spots with more than 96% concordance. C: Data of 33 spots with more than 96% concordance do not yield a Concordia age, but an upper intercept. D and E: Concordia ages with more than 96% concordance for the two discriminated age groups.

Use of an unmix routine discriminates two concordia age groups more than 96% concordant of 567.3 ± 1.6 Ma (ten samples – excluding two extreme “young” results: ca. 542 and ca. 548 Ma – Fig. 30D) and 586.6 ± 6.7 Ma (seven samples – Fig. 30E), with low MSWD values of 0.59 and 0.15, respectively. We support that the weighted average age is the best estimate of the magmatic crystallization age of these samples, in spite of the higher associated MSWD. This is supported because no clear age gap is observed when the whole set of data is considered and no textural contrast exists between the different spots. This result is consistent with zircon U-Pb ages reported in the literature for the São Vitor Tonalite and corresponds to the main episode of the Galileia Batholith construction (e.g. Noce et al., 2000; Mondou et al., 2012; Pinto, 2015).

Table 2. LA-ICP-MS U-Pb zircon data for the São Vitor Tonalite. Results in dark grey were not used in age calculations (inherited zircons or U-Pb discordance \leq 5%). Results \geq 10% U-Pb discordance are not shown here for their high discordance. Asterisk indicates inherited zircon.

TM11 São Vitor Tonalite – Localisation Lon -41.623849° Lat -18.004258°																						
Spot Id	206* (%)	204Pb cps	206Pb mV ¹	Th/U	206Pb/204Pb	1s %	207Pb/206Pb	1s %	207Pb/235U	1s %	206Pb/238U	1s %	Rho	207Pb/206Pb	2s abs	206Pb/238U	2s abs	207Pb/235U	2s abs	% U-Pb disc ⁵	Preferred age ⁶	2s abs
003-ZR1	0.0062	18	0.0061	0.457	252160	24.01	0.05918	0.54	0.780	1.13	0.0955	0.93	0.82	574	23	588	10	585	10	-2.49	588	10
005-ZR3	0.0120	14	0.0043	0.448	129335	19.75	0.05882	0.76	0.762	1.38	0.0939	1.09	0.79	560	33	579	12	575	12	-3.23	579	12
006-ZR4	0.0157	19	0.0060	0.857	99059	33.07	0.05966	0.50	0.793	1.27	0.0964	1.11	0.87	591	22	594	13	593	11	-0.39	594	13
020-ZR16	0.0166	14	0.0038	0.459	94075	26.45	0.05937	0.49	0.766	1.04	0.0936	0.84	0.81	581	21	577	9	577	9	0.73	577	9
022-ZR18*	0.0145	10	0.0030	0.426	106731	16.19	0.07138	0.77	1.551	1.26	0.1576	0.92	0.73	968	31	943	16	951	15	2.57	943	16
024-ZR20	0.0042	19	0.0184	0.206	371146	31.54	0.05877	1.40	0.731	1.98	0.0902	1.34	0.68	558	61	557	14	557	17	0.30	557	14
028-ZR22	0.0037	14	0.0144	0.232	424187	24.63	0.05905	0.53	0.740	0.99	0.0908	0.75	0.76	569	23	561	8	562	9	1.44	561	8
029-ZR23	0.0105	12	0.0052	0.172	147930	26.13	0.05843	0.55	0.739	1.06	0.0917	0.82	0.78	546	24	566	9	562	9	-3.62	566	9
030-ZR24	0.0120	10	0.0040	0.136	129541	18.44	0.05919	0.51	0.737	1.10	0.0903	0.90	0.82	574	22	558	10	561	9	2.91	558	10
031-ZR25	0.0030	14	0.0071	0.331	513942	52.90	0.05860	1.25	0.708	1.56	0.0876	0.86	0.55	552	54	542	9	544	13	1.96	542	9
033-ZR27	0.0113	51	0.0083	0.206	137978	31.88	0.05850	0.64	0.715	1.11	0.0887	0.83	0.75	548	28	548	9	548	9	0.15	548	9
036-ZR30	0.0065	19	0.0112	0.156	238488	28.25	0.05921	0.47	0.740	1.06	0.0907	0.87	0.83	575	20	560	9	563	9	2.66	560	9
042-ZR32	0.0052	51	0.0237	0.152	296981	41.72	0.05969	0.52	0.773	1.48	0.0940	1.34	0.90	592	23	579	15	582	13	2.29	579	15
047-ZR37	0.0050	56	0.0339	0.067	312534	41.51	0.05897	0.34	0.730	0.96	0.0898	0.81	0.85	566	15	554	9	557	8	2.06	554	9
049-ZR39	0.0034	24	0.0289	0.162	462611	28.59	0.05956	0.36	0.761	1.16	0.0927	1.04	0.90	588	16	572	11	575	10	2.73	572	11
055-ZR43	0.0213	22	0.0028	0.400	73193	21.09	0.05923	0.62	0.779	1.22	0.0953	0.98	0.81	576	27	587	11	585	11	-1.99	587	11
056-ZR44	0.0061	15	0.0091	0.264	255957	20.26	0.05905	0.29	0.762	0.95	0.0936	0.82	0.87	569	13	577	9	575	8	-1.37	577	9
060-ZR48	0.0019	19	0.0161	0.899	824219	55.65	0.05933	0.48	0.758	1.08	0.0927	0.89	0.83	579	21	571	10	573	9	1.35	571	10
065-ZR51	0.0052	24	0.0135	0.119	299722	29.56	0.06015	0.44	0.824	1.48	0.0993	1.36	0.92	609	19	611	16	610	14	-0.28	611	16
068-ZR54	0.0035	22	0.0204	0.108	450815	26.58	0.05922	0.63	0.740	1.36	0.0906	1.15	0.84	575	27	559	12	562	12	2.79	559	12
069-ZR55	0.0090	25	0.0123	0.337	173177	30.33	0.05904	1.81	0.735	2.23	0.0903	1.26	0.56	569	78	557	13	560	19	1.96	557	13
077-ZR61	0.0043	14	0.0124	0.300	365204	30.50	0.05915	0.78	0.756	1.70	0.0927	1.46	0.86	573	34	571	16	572	15	0.22	571	16

Table 2 - (continued)

078-ZR62	0.0039	16	0.0123	0.349	402836	22.84	0.05889	0.76	0.760	2.10	0.0936	1.93	0.92	563	33	577	21	574	18	-2.37	577	21
079-ZR63	0.0118	25	0.0093	0.170	131653	38.35	0.05899	0.65	0.753	1.52	0.0926	1.33	0.87	567	28	571	14	570	13	-0.75	571	14
083-ZR67	0.0079	19	0.0063	0.180	196801	20.06	0.05949	0.60	0.779	1.57	0.0950	1.40	0.89	585	26	585	16	585	14	-0.02	585	16
085-ZR69	0.0131	14	0.0035	0.232	118728	27.28	0.05878	0.81	0.749	1.23	0.0924	0.85	0.69	559	35	570	9	568	11	-1.95	570	9
086-ZR70	0.0024	16	0.0120	0.571	643768	49.54	0.05934	0.65	0.744	1.16	0.0909	0.88	0.76	580	28	561	9	565	10	3.24	561	9
089-ZR71	0.0046	14	0.0124	0.134	335878	24.64	0.05939	0.68	0.754	1.03	0.0921	0.69	0.67	582	29	568	7	571	9	2.35	568	7
091-ZR73	0.0102	23	0.0204	0.116	152788	43.42	0.05931	0.49	0.745	0.87	0.0911	0.62	0.71	579	21	562	7	565	8	2.88	562	7
096-ZR78	0.0073	17	0.0078	0.499	214642	25.33	0.05971	0.62	0.801	1.12	0.0973	0.85	0.76	593	27	598	10	597	10	-0.91	598	10
104-ZR84	0.0031	14	0.0111	0.526	496737	31.56	0.05921	0.42	0.733	1.07	0.0898	0.92	0.85	575	18	554	10	558	9	3.61	554	10
109-ZR89	0.0128	34	0.0074	0.344	122059	27.89	0.05933	0.62	0.760	1.26	0.0929	1.03	0.82	579	27	573	11	574	11	1.14	573	11
118-ZR96	0.0102	82	0.0287	0.179	153042	83.91	0.05945	1.54	0.759	1.71	0.0926	0.64	0.38	583	66	571	7	574	15	2.11	571	7
121-ZR99	0.0097	28	0.0073	0.326	159886	34.25	0.05912	0.60	0.745	1.06	0.0914	0.79	0.74	571	26	564	9	565	9	1.37	564	9
Data not used in age calculations due to high discordance ($\geq 4\%$ U-Pb Disc.)																						
007-ZR5	0.0089	52	0.0338	0.172	174101	70.57	0.05916	0.50	0.829	1.35	0.1017	1.19	0.89	573	22	624	14	613	12	-8.97		
009-ZR7	0.0104	29	0.0088	0.270	149539	39.49	0.05906	0.74	0.817	1.35	0.1004	1.06	0.79	569	32	616	12	606	12	-8.31		
010-ZR8	0.0096	15	0.0073	0.454	161980	22.79	0.05926	0.54	0.825	1.25	0.1010	1.07	0.85	577	23	620	13	611	11	-7.55		
011-ZR9	0.0210	19	0.0040	0.205	74142	33.55	0.05875	0.90	0.790	1.34	0.0975	0.93	0.69	558	39	600	11	591	12	-7.46		
012-ZR10	0.0111	12	0.0042	0.245	140535	18.93	0.05916	0.71	0.795	1.43	0.0974	1.19	0.83	573	31	599	14	594	13	-4.55		
015-ZR11	0.0081	8	0.0042	0.573	191228	11.96	0.05953	0.60	0.747	1.28	0.0910	1.08	0.84	586	26	561	12	566	11	4.26		
016-ZR12	0.0034	16	0.0136	0.132	455245	21.34	0.05887	1.24	0.705	2.10	0.0868	1.65	0.79	562	54	537	17	542	18	4.51		
018-ZR14	0.0166	16	0.0023	0.306	94020	31.05	0.05942	0.74	0.734	1.29	0.0895	0.99	0.77	583	32	553	10	559	11	5.10		
019-ZR15	0.0513	49	0.0059	0.359	30381	46.77	0.05989	0.53	0.762	1.24	0.0922	1.06	0.85	600	23	569	12	575	11	5.16		
021-ZR17	0.0054	14	0.0078	0.214	287874	22.89	0.05970	0.40	0.749	1.00	0.0910	0.84	0.84	593	17	561	9	568	9	5.27		
023-ZR19	0.0065	51	0.0369	0.163	240007	54.10	0.05998	0.33	0.765	0.87	0.0925	0.72	0.82	603	14	570	8	577	8	5.39		
032-ZR26	0.0091	28	0.0089	0.251	171875	32.35	0.05981	0.65	0.755	1.37	0.0915	1.15	0.84	597	28	564	12	571	12	5.43		
034-ZR28	0.0037	19	0.0162	0.101	426312	20.67	0.05954	0.55	0.734	1.03	0.0894	0.79	0.77	587	24	552	8	559	9	5.99		
035-ZR29	0.0054	23	0.0165	0.083	287306	30.93	0.06003	0.52	0.763	1.13	0.0922	0.93	0.83	605	22	568	10	576	10	6.01		
041-ZR31	0.0617	93	0.0158	0.264	25264	32.40	0.05940	0.82	0.724	1.45	0.0884	1.14	0.78	582	35	546	12	553	12	6.19		
043-ZR33	0.0250	64	0.0063	0.288	62214	37.84	0.05910	1.08	0.706	1.56	0.0866	1.06	0.68	571	47	535	11	542	13	6.20		
044-ZR34	0.0144	42	0.0286	0.227	108002	40.42	0.05959	0.45	0.735	0.90	0.0894	0.69	0.76	589	19	552	7	559	8	6.24		

Table 2 – (continued)

045-ZR35	0.0367	25	0.0017	0.585	42392	49.38	0.06023	1.48	0.771	2.04	0.0928	1.35	0.66	612	63	572	15	580	18	6.50
046-ZR36	0.0072	37	0.0185	0.453	216788	30.78	0.05980	0.41	0.745	1.47	0.0903	1.36	0.93	597	18	557	15	565	13	6.55
048-ZR38	0.0031	30	0.0361	0.117	498213	35.29	0.05968	0.41	0.737	0.87	0.0896	0.67	0.77	592	18	553	7	561	7	6.61
050-ZR40	0.0094	26	0.0073	0.251	165999	23.75	0.05991	0.50	0.750	0.95	0.0908	0.72	0.76	600	22	561	8	568	8	6.63
054-ZR42	0.0032	26	0.0156	0.178	487716	52.85	0.05990	0.35	0.749	0.96	0.0907	0.81	0.85	600	15	560	9	568	8	6.66
057-ZR45	0.0108	21	0.0068	0.819	144098	30.53	0.07298	0.68	1.584	0.99	0.1574	0.61	0.61	1013	28	942	11	964	12	7.00
058-ZR46	0.0055	37	0.0141	0.140	282569	25.44	0.05962	0.46	0.730	0.92	0.0887	0.70	0.76	590	20	548	7	556	8	7.09
059-ZR47	0.0078	16	0.0055	0.284	197980	23.06	0.07113	0.69	1.454	1.72	0.1482	1.53	0.89	961	28	891	25	912	21	7.30
061-ZR49	0.0102	18	0.0078	0.278	152354	29.02	0.06077	0.48	0.795	1.45	0.0949	1.32	0.91	631	20	584	15	594	13	7.43
066-ZR52	0.0028	9	0.0164	0.214	544494	21.97	0.12140	0.55	5.483	1.68	0.3275	1.54	0.92	1977	20	1826	49	1898	29	7.61
067-ZR53	0.0084	12	0.0055	0.244	184443	26.26	0.05944	0.61	0.712	1.38	0.0868	1.18	0.86	583	26	537	12	546	12	7.97
070-ZR56	0.0116	27	0.0082	0.381	134004	33.50	0.06026	0.54	0.755	0.86	0.0909	0.56	0.65	613	23	561	6	571	8	8.56
071-ZR57	0.0170	15	0.0033	0.431	91391	19.72	0.06003	0.61	0.740	1.33	0.0894	1.12	0.84	605	26	552	12	562	11	8.76
072-ZR58	0.0043	17	0.0112	0.964	365669	20.19	0.05970	0.61	0.720	1.16	0.0875	0.92	0.79	593	26	541	9	551	10	8.80
073-ZR59	0.0030	20	0.0167	0.167	511372	54.26	0.06006	0.38	0.736	0.91	0.0888	0.73	0.81	606	16	549	8	560	8	9.42
074-ZR60	0.0104	33	0.0164	0.108	149880	23.25	0.06027	0.56	0.748	1.00	0.0900	0.74	0.74	613	24	555	8	567	9	9.45
080-ZR64	0.0036	15	0.0151	0.404	433730	22.44	0.05997	0.63	0.687	1.09	0.0831	0.81	0.74	603	27	515	8	531	9	14.58
082-ZR66	0.0056	19	0.0130	0.720	276113	30.48	0.05974	0.63	0.710	1.02	0.0862	0.71	0.70	594	27	533	7	545	9	10.32
084-ZR68	0.0097	14	0.0037	0.406	160169	31.07	0.06021	0.81	0.690	1.19	0.0830	0.79	0.66	611	35	514	8	533	10	15.85
092-ZR74	0.0063	16	0.0072	0.290	245881	16.84	0.05997	0.58	0.722	1.02	0.0873	0.75	0.74	603	25	539	8	552	9	10.48
093-ZR75	0.0220	7	0.0018	0.220	70710	16.69	0.06777	1.57	0.818	3.30	0.0875	2.87	0.87	862	64	541	30	607	30	37.24
094-ZR76	0.0108	13	0.0041	0.471	144525	16.55	0.06124	0.52	0.749	1.30	0.0887	1.13	0.87	648	22	548	12	568	11	15.39
095-ZR77	0.0109	43	0.0081	0.128	142342	49.32	0.05726	1.07	0.757	2.22	0.0959	1.91	0.86	502	47	590	22	572	19	-17.68
097-ZR79	0.0212	7	0.0013	0.317	73372	31.93	0.06081	1.12	0.682	1.63	0.0814	1.12	0.69	632	48	504	11	528	13	20.24
098-ZR80	0.0097	12	0.0054	0.370	161439	19.87	0.06004	0.53	0.722	1.09	0.0872	0.87	0.80	605	23	539	9	552	9	10.96
101-ZR81	0.1025	214	0.0503	0.171	15200	4.66	0.06057	0.48	0.756	1.28	0.0905	1.12	0.88	624	21	558	12	572	11	10.49
102-ZR82	0.0101	61	0.0200	0.429	155014	39.31	0.06138	0.82	0.687	1.40	0.0812	1.08	0.77	653	35	503	10	531	12	22.88
103-ZR83	0.0333	165	0.0076	1.532	46791	81.83	0.06563	1.56	0.848	1.87	0.0937	0.97	0.52	795	65	577	11	623	17	27.38
105-ZR85	0.0083	21	0.0084	0.315	188352	32.78	0.06010	0.61	0.721	1.12	0.0870	0.86	0.77	607	26	538	9	551	10	11.39
106-ZR86	0.1507	80	0.0072	0.257	10324	18.67	0.08328	2.89	1.397	3.20	0.1217	1.32	0.41	1276	111	740	18	888	38	41.98

Table 2 – (continued)

107-ZR87	0.0468	99	0.0106	0.170	33293	53.09	0.06159	0.78	0.721	2.08	0.0849	1.89	0.91	660	33	525	19	551	18	20.39		
108-ZR88	0.0286	18	0.0025	0.353	54390	19.84	0.06099	0.71	0.778	1.31	0.0925	1.05	0.80	639	30	571	11	584	12	10.70		
110-ZR90	0.0145	25	0.0053	0.412	107399	32.97	0.06126	1.79	0.756	2.37	0.0895	1.52	0.64	648	76	553	16	572	21	14.73		
114-ZR92	0.0019	22	0.0363	0.134	812689	25.85	0.08859	2.29	2.277	2.96	0.1864	1.84	0.62	1395	86	1102	37	1205	41	21.04		
115-ZR93	0.0461	40	0.0073	0.093	33785	23.57	0.05872	1.55	0.884	2.22	0.1092	1.54	0.70	557	67	668	20	643	21	-19.98		
116-ZR94	0.0068	21	0.0070	0.313	228056	32.11	0.07199	1.84	1.117	2.40	0.1125	1.49	0.62	986	74	687	19	761	26	30.28		
117-ZR95	0.1481	292	0.0411	0.377	10517	11.17	0.06154	0.67	0.752	1.65	0.0886	1.46	0.88	658	29	547	15	569	14	16.86		
119-ZR97	0.0032	27	0.0294	0.152	483772	33.31	0.15114	1.97	4.665	2.45	0.2238	1.41	0.58	2359	66	1302	33	1761	41	44.80		
120-ZR98	0.0425	57	0.0054	0.409	36614	33.88	0.06122	0.88	0.747	1.26	0.0885	0.83	0.66	647	37	546	9	566	11	15.54		
122-ZR100	0.0106	25	0.0088	0.243	147652	29.26	0.06007	0.46	0.728	1.03	0.0880	0.84	0.82	606	20	543	9	556	9	10.32		
Data not used in age calculations due to high analytical error																						
004-ZR2	0.0163	68	0.0045	0.416	95612	35.83	0.05414	4.13	0.687	4.23	0.0920	0.85	0.20	377	181	567	9	531	35	-50.48		
008-ZR6	0.0051	13	0.0119	0.241	303535	25.77	0.05203	7.29	0.466	13.73	0.0650	11.63	0.85	287	317	406	91	388	87	-41.56		
017-ZR13	0.0833	161	0.0022	0.408	18689	54.05	0.08735	9.93	1.091	10.01	0.0906	1.21	0.12	1368	360	559	13	749	103	59.14		
027-ZR21	0.0182	18	0.0024	0.201	85782	44.00	0.05669	3.11	0.783	7.42	0.1002	6.72	0.91	480	135	615	79	587	65	-28.29		
053-ZR41	0.2859	323	0.0050	0.250	5444	47.32	0.07627	10.75	1.151	10.91	0.1094	1.83	0.17	1102	402	669	23	778	115	39.28		
062-ZR50	0.0055	17	0.0100	0.667	281121	24.91	0.10814	3.65	3.413	6.40	0.2289	5.25	0.82	1768	130	1329	125	1507	98	24.86		
081-ZR65	0.4240	494	0.0017	0.665	3674	95.19	0.10331	14.92	1.279	15.01	0.0898	1.54	0.10	1684	505	554	16	836	164	67.10		
090-ZR72	0.0047	14	0.0121	0.101	311258	32.90	0.21427	4.32	16.613	6.52	0.5623	4.88	0.75	2938	136	2876	224	2913	121	2.11		
113-ZR91	0.0623	136	0.0034	0.354	24999	40.64	0.05192	3.93	0.612	4.11	0.0855	1.12	0.27	282	175	529	11	485	31	-87.74		

Notes: ¹Conversion factor from mV to CPS is 62500000. ²Concentration uncertainty c.20%. ³Data not corrected for common-Pb. ⁴Not corrected for common-Pb.

⁵Discordance calculated as $(1 - ({}^{206}\text{Pb}/{}^{238}\text{U age}) / ({}^{207}\text{Pb}/{}^{206}\text{Pb age})) * 100$. ⁶Preferred age: ${}^{207}\text{Pb}/{}^{206}\text{Pb}$ (Ages > 1.0 Ga) and ${}^{206}\text{Pb}/{}^{238}\text{U}$ (Ages < 1.0 Ga).

IV.6. DISCUSSION

IV.6.1. Significance of magnetic fabrics

The integrated magnetic susceptibility measurements and magnetic mineralogy investigations revealed that the magnetic susceptibility on sample from the host metasedimentary rocks of the Tumiritinga Formation, São Vitor Tonalite, and Mantiqueira Complex, with K_m values of $\sim 5 \cdot 10^{-4}$ SI is dominantly paramagnetic, further confirmed by the constant drop of susceptibility with increasing temperature in the K-T curve acquisition. Small amounts of magnetite were however detected in the hysteresis and IRM curves, Although this mineral does not exert the dominant control on the magnetic fabric. Moreover, the comparison between the AMS and AARM ellipsoids shows different orientations, suggesting that the ferromagnetic fabric remains subsidiary. Therefore, we consider that biotite and amphibole are the main contributors to the AMS fabric of these units. Previous studies conducted in the São Vitor Tonalite also attest that the AMS results indicate a paramagnetic behavior for this unit (Mondou et al., 2012; Portela, 2013).

Magnetic investigations showed that the Guarataia Granodiorite displays a ferromagnetic behavior. The dominance of magnetite as the main AMS carrier is supported by the thermomagnetic, hysteresis and IRM curves, which indicate the Curie temperature and Verwey transitions, S-shaped hysteresis curve, and saturation of remanent magnetization below 0.2 T. In addition, the FORC diagram displayed a pattern demonstrating that MD magnetite is the main ferromagnetic mineral. AARM and AMS ellipsoids showed a coaxial relationship, displaying a correspondence between the remanence-bearing minerals, identified as MD magnetite, and the paramagnetic fraction. Consequently, the AMS fabric carrier of the Guarataia Granodiorite is governed by MD magnetite.

The Caladão Granite and the Padre Paraíso Charnockite report a Curie temperature at c. 580°C, well defined Verwey transition at -160°C, and rapid acquisition of IRM in applied field below 0.2 T, indicating the presence of magnetite crystals controlling the AMS. The predominant ferromagnetic fraction of these units reports a typical PSD behavior in the FORC diagrams, displaying a broad vertical and horizontal spreading, and three weaker, less prominent lobes. Accordingly, PSD magnetite grains may be responsible for the AMS axes. However, the AMS and AARM tensors do not show a correspondence. It seems that dominant PSD magnetite grains of the Caladão Granite are weakly oriented, and their contribution to low-field susceptibility is not significant anisotropic to deflect the AMS fabric

(i.e. to become AMS parallel to AARM). The weaker anisotropy of the oxide ferromagnetic sub-fabric fails to conceal the AMS signature from the other components.

The Padre Paraíso Charnockite presents a well-defined magnetic fabric in the AARM measurements. The difference between A_{\max} and K_{\max} in the charnockite suggests that magnetite grains have been anticlockwise rotated approximately $\sim 90^\circ$ from the charnockite plane since AARM fabrics are due magnetite grains, whereas K_{\max} is oriented in the charnockite plane. To explain the rotation of the magnetite grains, we suggest that these different fabrics may reflect a transpression-induced strain partitioning. The AMS fabric formed by the paramagnetic fraction might have accommodated the compressive component, as illustrated by the east-verging magnetic foliation bearing a down-dip magnetic lineation (K_{\max} , Fig. 25G and Fig. 29F). On the other hand, the AARM fabric accommodated the horizontal component of the transpressive deformation, suggested by the sub-horizontal \sim NS magnetic lineation (A_{\max}) of the ferromagnetic fraction (Fig. 29F). More details regarding the deformation partitioning are discussed further on this section.

This non-parallelism relationship between both tensors has also been reported in previous studies. Borradaile and Gauthier (2003, 2006) described anomalous magnetic fabrics in ophiolite dikes from the Troodos ophiolite of Cyprus. Raposo and Berquó (2008) and Raposo (2017) also obtained non-coaxial tensors and suggested that magnetite grains rotated from the dike plane for dike swarms of Salvador (Bahia State, NE Brazil) and on beaches of NE São Paulo State coastline.

In paramagnetic rocks which have biotite and amphibole as the main AMS carriers (abundant minerals in the Tumiritinga Formation, Mantiqueira Complex and São Vitor Tonalite), the magnetic fabric is given by the magneto-crystalline anisotropy. Biotite has K_{\min} parallel to the pole of the basal plane, which tends to parallel the flow plane (foliation) (Bouchez, 1997; Arbaret et al., 1997; Bouchez, 2000). The elongated prism in amphibole is parallel to K_{\max} , which tends to parallel the flow direction, and it is a good proxy for the magnetic lineation (Parry, 1971; Wagner et al., 1981; Hrouda, 1982). Consequently, the magnetic fabric given by the AMS ellipsoid can be used as a good proxy for petrofabric in these rocks, and can be related to the strain that the magma was submitted before crystallization. For specimens with higher magnetic susceptibility, the contribution of the shape anisotropy of ferromagnetic minerals to the bulk susceptibility becomes important. The Guarataia Granodiorite, the Caladão Granite and the Padre Paraíso Charnockite have a

dominant ferromagnetic behavior and the AMS is controlled by grain shape (Borradaile and Henry, 1997) rather than crystallographic structure (as in the paramagnetic minerals). Shape anisotropy is important in minerals that crystallize in isotropic system such as magnetite. Both MD and PSD magnetite grains can yield the shape anisotropy (Ferre et al, 2002), in which K_{\max} is parallel to the long axis of the particle.

Altogether, the AMS resulting from the magnetocrystalline anisotropy of biotite and amphibole, and shape anisotropy of PSD and MD magnetite grains can be related to the strain the magma was submitted before crystallization of the plutonic bodies and during pervasive melting of the host metasedimentary rocks. In addition, the comparison of the magnetic fabric and the field measurements shows a good consistency (Fig. 25), and this supports that the AMS can be used as a reliable proxy of the tectonic fabric.

IV.6.2. Microstructures

Direct examination in the field and microscope examination of the sampled rocks of the study area were analyzed to determine magmatic versus solid-state deformation, in order to compare with the AMS study. Magmatic rocks tend to crystallize gradually passing through a transitional stage between the liquid and the solid state (Passchier and Trouw, 2005). Two types of microstructures of the igneous rocks (São Vitor Tonalite, Guarataia Granodiorite, Padre Paraíso Charnockite, and Caladão Granite) of the studied area were observed: the magmatic and the sub-magmatic types. (i) the magmatic type, characterized by large quantities of interstitial quartz, and no evidences of solid-state deformation features (e.g. intracrystalline deformation or recrystallization); and (ii) the sub-magmatic type, demonstrated if there is evidence for crystal deformation and contemporaneous presence of melt, represented in the studied samples by less frequent interstitial quartz, locally with undulose extinction and subgrains, deformation twins in plagioclase, and undulose extinction in K-feldspar.

According to Vernon (2000), interactions between crystals when the proportion of crystals in suspension is large may trigger locally solid-state deformation features, such as quartz with undulose extinction and subgrains, and/or plagioclase with deformation twins. The progressive cooling of a magmatic body results in the increase of the crystal fraction and consequently, in the reduction of the amount of melt available, characterizing a transition of rheological state between suspension to grain-supported flow (e.g. Cavalcante et al., 2013). Rosenberg and Handy (2005) argue that the strength of magmas deforming during

crystallization remains low until they reach a proportion of solid-phases of ~90%. The coexistence of these two types of microstructures in the igneous rocks sampled in this study suggests that the plutonic bodies were deformed under high temperatures in a magmatic state by suspension or grain-supported flow depending on the proportion of liquid-crystals (Vigneresse et al., 1996; Barboza and Bergantz, 1998; Rosenberg and Handy, 2000).

The syn- to late plutons of the studied area, corresponding to the main and final deformational periods of the Araçuaí belt, show evidence of pervasive deformation in the magmatic state, and only scarce samples display solid-state deformation features, that might represent the late stages of solidification (Blumenfeld and Bouchez, 1988). Such characteristics likely indicate that deformation occurred before these rocks reached solid state.

A third microstructural type is described in the host partially melted metasedimentary rocks of the Tumiritinga Formation and in the basement unit represented by the Mantiqueira Complex, evidencing predominant (iii) high-temperature solid-state deformation features. Internal deformation of quartz is often visible as undulose extinction, formation of subgrains and recrystallization into smaller grains. Sharp contacts of quartz crystals with stretched biotite are also common. The solid-state deformation fabric attained by these rocks is consistent with the magmatic fabrics of the plutons, and this parallelism is a result of the simultaneity or slightly diachronous deformation affecting the crust and the emplaced magmas.

IV.6.3. Geochronology

Five U-Pb zircon ages of 585 ± 4 (Mondou et al., 2012), 615 ± 6 Ma, 584 ± 8 Ma, 594 ± 5 Ma (Pinto et al., 2015), and 567 ± 5 Ma (this study) come from the São Vitor Tonalite within the defined study area in the CPU, near the city of Itambacuri (Fig. 21A). To the south of the study area near the city of Governador Valadares (Fig. 20A), Mondou et al. (2012) obtained other seven U-Pb zircon ages for the São Vitor and Galiléia tonalites (Galiléia Batholith), and the results are around ca. 580 Ma. To the north of the study area near Teófilo Otoni city (Fig. 21A), the São Vitor Tonalite zircon grains yielded a mean crystallization age of 576 ± 4 Ma (Noce et al., 2000; Pb-Pb evaporation method). These data suggest that huge volumes of granodioritic/tonalitic magmas were emplaced in the CPU between ca. 615 and ca. 570 Ma. This is coeval with the U-Pb age spectra reported for the Carlos Chagas Batholith (ca. 597 – 572 Ma) in the EAU, where Cavalcante et al. (2018) indicate that collision was initiated before ca. 600 Ma triggering a pervasive partial melting event of the middle crust

that formed the anatectic core of the Araçuaí belt. This partial melting event remained over a period of at least ~25 Ma, which is in agreement with the defined period of zircon crystallization between ca. 586 – 567 Ma (~19 Ma), represented by the two concordia ages obtained in this study for the São Vitor Tonalite. However, a zircon crystallization age interval of ca. 45 Ma is defined when comparing the oldest and youngest ages obtained for the São Vitor Tonalite. This long range of zircon crystallization without age gaps might have been favored by slow cooling conditions caused by the partial melting of the middle crust.

In such context of protracted deformation, we suggest that the São Vitor Tonalite emplaced over a succession of episodic intrusions (e.g. Coleman et al., 2004; Glazner et al., 2004; Salazar et al., 2016), and was deformed before complete crystallization, since no evidence of solid-state deformation was observed in the microstructural analyses. Moreover, this emplacement occurred under high-temperature conditions triggered by the partial melting event of the middle crust, favouring a large crystallization range of the zircon crystals due to the slow cooling behavior of the orogen.

IV.6.4. Structural setting

In the study area, the plutonic bodies and host metasedimentary rocks presented contrasted fabric, however, the various fabrics formed and evolved for a long time before the magma reached solid-state, in a thermally buffered environment. Since cooling rate in this segment of the orogen was relatively slow (<5°C/My, U-Pb and Ar-Ar) (Petitgirard et al., 2009), the synkinematic plutons were emplaced with respect to the regional fabrics of an already deforming crust, and the shape of the plutons reflect the symmetry of the regional fabric pattern. Complex shapes discordant to the regional fabrics may be attained by late kinematic plutons (Chardon et al., 2009). The Araçuaí orogen represents a case of weak lithosphere (Vauchez et al., 2007), involving an abnormally hot crust containing a large amount of melt due to magmatism over long periods (630-480 Ma) (Pedrosa-Soares et al., 2011; Gonçalves et al., 2014), remaining hot and therefore mechanically weak and with low viscosity over protracted periods of deformation (e.g. Rosenberg and Handy, 2005; Chardon et al., 2009). The compression of weak lithospheres results in distributed deformation and lack of strain localization along major thrusts (e.g. Gaspais et al., 2009).

The composite observed fabric of the studied rocks results from the interplay of belt-normal thrusting and subsidiary belt-parallel transcurrent flow, induced by horizontal, orogen-normal shortening resulting from the convergence between the São Francisco and Congo

Cratons. The structural continuity between the three domains deformed in solid or magmatic state, the incipient strain partitioning along the contacts between them, and the coherence of the kinematics, favors this interpretation.

Furthermore, the simultaneity of the deformation in the different structural domains is supported by similar U/Pb ages. Remarkably consistent ages have been reported for the granodioritic/tonalitic magmas from the CPU and neighboring units (mostly between 567 – 615 Ma), represented by the Guarataia, Brasilândia, São Vitor, Galileia plutons in the CPU and WMU and the Carlos Chagas batholith in the EAU. The magmatic fabrics of these rocks are coeval to the solid-state fabrics of their host metasedimentary rocks (Tumiritinga and São Tomé formations) and the basement rocks of the Mantiqueira Complex. Younger ages obtained in the late- and post-collisional granitic magmas represented by the Caladão Granite and Padre Paraíso Charnockite indicate that magmatic pulses occurred until at least ca. 480 Ma.

Field observations and the AMS fabrics obtained in the plutonic bodies and host metasediments allowed us to individualize four different structural regions. Region 1 is characterized by an orogen-parallel foliation gently dipping eastward bearing a predominantly horizontal lineation to the east (transitioning to the CPU) and a down-dip lineation to the east (in the WMU). This region includes the transition from the WMU and the CPU, marked by westward thrust tectonics (Fig. 31), previously observed by Vauchez et al. (2007), Petitgirard et al. (2009), and Mondou et al. (2012). This structural pattern was probably favoured by the continuation of the cratonic lithosphere beneath the allochthonous units.

Transitioning from eastern portion of region 1 to region 2 in the CPU, horizontal lineations associated with steeply dipping to vertical foliation planes predominate, suggesting a transpression tectonic regime (Fig. 31). Fabric type of region 3 is mostly marked by gently dipping westward NS-trending foliation associated with shallow plunging lineations that frequently shifts to sub-vertical (Fig. 31), interpreted also as a transpression-induced strain partitioning. This pattern is in agreement with the fabric types 1 and 2 described by Mondou et al. (2012), where the transition between the WMU to the westernmost part of the CPU is progressive, since the dip of the foliation progressively steepen, becoming sub-vertical, both in the plutonic bodies and host metasedimentary rocks, suggesting the continuity of the structural pattern.

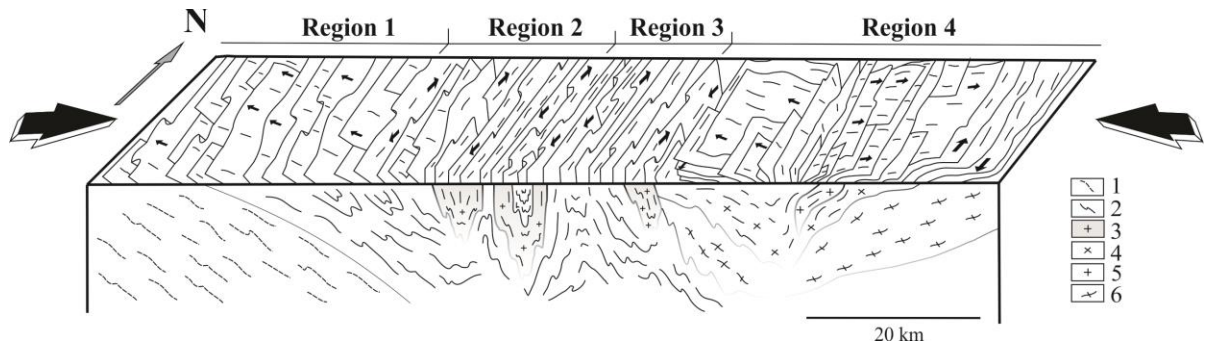


Fig. 31. Schematic cross section showing the structural pattern of the studied area, constructed using the structural data from Fig. 6. The main flow directions are represented by small black arrows. From W to E: the western and central regions 1, 2, and 3 involving metasedimentary rocks of the São Tomé (1) and Tumiritinga (2) formations, and syn-collisional intrusive São Vitor Tonalite (3); the eastern region 4, comprising late-porphyrific granites associated with charnockites (5) intruding dominant anatexites (6).

Under high temperature and low cooling rates in the middle and lower crust, a large amount of melt resulting both from magmatism and anatexis is present, and temperature is almost homogenous over large volumes. Consequently, transitions between orogenic domains are continuous since rheological contrasts between different rock types are minimized. In addition, strain repartition is less efficient, leading to homogeneous deformation (Vanderhaeghe and Teyssier, 2001; Vauchez and Tommasi, 2003). The transpression-induced tectonic regime interpreted for the structural region 2 and 3 might have been favored by the low viscosity of the tonalitic/granodioritic magmas, triggered by the widespread partial melting that underwent in the middle/lower crust (e.g. Rosenberg and Handy, 2005; Beaumont et al., 2006; Rosenberg et al., 2007; Cavalcante et al., 2014).

The field measurements of region 4 obtained from the late-collisional body Caladão granite and in host anatexites (Ataleia suite) of the EAU are characterized by flat-lying foliation planes bearing sub-horizontal ~NS-trending lineations. This sector displays a sharp transition from steep foliations in the central domain to flat/gently dipping foliations within the eastern domain. The AMS measurements performed in the late- to post-collisional Padre Paraíso Charnockite present NE-trending gently dipping westward magnetic foliation bearing down-dip magnetic lineation. These late magmatic bodies were emplaced after solidification of the anatectic country rock. Magmatic fabric in the EAU, specifically in the Carlos Chagas anatectic domain, intruded in partially molten metasediments, is characterized by a complex flow field. Such behavior represents an orogenic region in which long-lived and pervasive partially molten middle crust might have favored the combination of convergence and gravity-driven forces that promoted a “channel flow like” tectonic behavior (Cavalcante et al., 2013; 2018).

Because of the still regionally high thermal conditions during the emplacement of these younger bodies, the interference between the late- to post-collisional granites (540-480 Ma) and associated host rocks may express poorly defined internal fabrics. However, AMS fabric pattern mapped by Xavier (2017) of the Aimorés Suite south of the studied area near Itabirinha de Mantena city (Fig. 21A), show a predominant magnetic foliation oriented NNE, with subsidiary NW directions. Magnetic lineations show an obliquity in relation to magnetic foliation. This structural pattern suggests a compressive component as a result of the still active deformation during that time. Our data show an eastern tectonic vergence generated by compressive stress. The magmatic event responsible for the formation of the Aimorés Suite is coeval to the high-grade metamorphism and main deformation events affecting the rocks of the West Congo belt (ca. 540 Ma), in the African counterpart of the Araçuaí-Ribeira orogenic system in Angola (Monié et al., 2012), and of the Cabo Frio Tectonic Domain, where metamorphic peak ages are between 525-520 Ma (Schmitt et al., 2004). This collisional setting might have triggered a limited reactivation of the Araçuaí belt in response to the final collision of South America and Africa continents during the final welding of the Gondwana supercontinent.

In this context, we hypothesize that this complex flow field represented by the variability of the tectonics fabric at the scale of the studied area results from the combination of convergence and gravity-driven tectonics, influenced by the contribution of the high-temperature gradient and the low cooling rate that is described in this segment of the orogen.

IV.7. CONCLUSIONS

Detailed structural mapping using field and AMS measurements across an imbricated synkinematic tonalitic batholith and subsidiary granites and host metasedimentary rocks, and late magmatic bodies intruded in anatexites revealed contrasted strain distribution formed before solidification in the northern portion of the Neoproterozoic Araçuaí-Ribeira orogenic system. This study revealed that AMS results from the magnetocrystalline anisotropy of biotite and/or amphibole and the shape anisotropy of MD or PSD magnetite grains, and therefore, AMS can be used as a proxy of the petrofabric. Field and AMS foliation and lineation measurements allowed us to define 4 main structural regions with contrasted fabrics that resulted from the interplay of belt-normal thrusting (regions 1 and 4) and transpression induced tectonics (region 2 and 3) caused by the convergence of the São Francisco and Congo Cratons.

The structural continuity between the domains, the incipient strain partitioning along the contacts between them, the parallelism between the magmatic fabric of the plutonic bodies and the solid-state deformation fabric attained by the host metasediments and basement unit, and the partial melting of the middle crust support emplacement of the magmas during deformation resulted from the collision.

U-Pb zircon ages from the magmatic bodies of the studied area support that magmatic pulses occurred over more than 100 Ma (ca. 615-480 Ma). Following the first metamorphic peak associated with the convergence of the São Francisco and Congo cratons, granodioritic/tonalitic magmas were emplaced in the CPU between ca. 615-567 Ma, slightly coeval with the estimated age of deformation due to the emplacement of synkinematic leucocratic veins around 580 Ma, and with the pervasive melting of the middle/lower crust that formed the anatectic core of the Araçuaí belt (597-572 Ma). Plutonic bodies of younger ages (ca. 540-480 Ma) are probably related to a minor metamorphic peak associated to a reactivation of the orogen around 540-530 Ma during the final welding of the Gondwana supercontinent.

Microstructural investigations revealed that the huge amounts of magmas involved were deformed at magmatic state, following some kinematics described in 'hot orogens'. The structures developed at the scale of the studied area within the viscous magmas and host metasedimentary rocks and basement unit resulted in a complex strain pattern that is consistent with the kinematics at orogen-scale. Considering the huge volume of melt that intruded the pervasively molten middle crust and the associated high thermal gradient, the observed fabrics and structural patterns are most likely a result of combined tangential tectonics induced by the compression, and gravitational forces arising from the load of the overlying crust. The described flow patterns were permitted by the weakness of the middle/lower crust, accommodating the shortening and thickening of the belt.

CHAPTER V

V.1. SYNTHESIS AND CONCLUSIONS

The combined structural analyses, rock magnetism investigations, and geochronological studies conducted throughout this research allowed to elucidate questions concerning the deformation framework in the defined segment of the Araçuaí orogenic belt in response to the convergence of the São Francisco and Congo cratons.

Magnetic mineralogy investigations in six rock types of the study area revealed that AMS results from the magnetocrystalline anisotropy of biotite and/or amphibole and the shape anisotropy of MD and/or PSD magnetite grains, and consequently, AMS could be used as a proxy of the petrofabric. The AMS together with the field measurements allowed to characterize a complex strain distribution pattern across the allochthonous domains. Four main structural regions with contrasting fabrics were defined and indicate an interplay of belt-normal thrusting, transpression induced tectonics, and horizontal flow generated due to the collision of the São Francisco and Congo cratons. Microstructural investigations showed that the magmatic bodies within the study area were deformed at magmatic state, while the host metasediments and basement unit under solid-state conditions. The parallelism between the magmatic and solid-state fabrics, together with the continuity and incipient strain partitioning between the structural regions, and partial melting of the middle crust support that the magmatic bodies were subjected to deformation before complete crystallization.

Geochronological studies and data from previous works show that magmatic pulses occurred over more than 100 Ma (ca. 615-480 Ma), promoting a deformation of magmas in viscous state. Following the first metamorphic peak associated with the convergence of the São Francisco and Congo cratons, granodioritic/tonalitic magmas (such as the São Vitor Tonalite, Guarataia, and Brasilândia plutons) were emplaced in the CPU and WMU between ca. 615-567 Ma, slightly coeval with the estimated age of deformation due to the emplacement of synkinematic leucocratic veins around 580 Ma, and with the pervasive melting of the middle/lower crust that formed the anatectic core of the Araçuaí belt (597-572 Ma). Plutonic bodies of younger ages (ca. 540-480 Ma), such as the Caladão and Padre Paraíso plutons, emplaced in the EAU, are probably related to a minor metamorphic peak associated to a reactivation of the orogen around 540-530 Ma during the final welding of the Gondwana supercontinent. Such a long period of time characterized by the huge volume of melt that intruded the pervasively molten middle crust, and the associated high thermal

gradient, follow some characteristics described in hot orogenic settings. Under these circumstances, the observed fabrics and structural patterns are most likely a result of combined tangential tectonics induced by the compression, and gravitational forces arising from the load of the overlying crust. The described flow patterns were permitted by the weakness of the middle/lower crust, accommodating the shortening and thickening of the belt.

REFERENCES

- Afonseca B.D., D'ávila D., Tensol I., Silva V.M. 2011. Individualização faciológica em escala 1:50.000 das Suítes Brasilândia e Guarataia, Faixa Araçuaí – MG. Trabalho de graduação, Universidade Federal de Minas Gerais, 92p.
- Ahrens, L. H., 1955. Implications of the Rhodesia age pattern. *Geochimica et Cosmochimica Acta*, 8(1-2), 1-15.
- Alkmim, F.F., Marshak, S., Pedrosa-Soares, A.C., Peres, G.G., Cruz, S.C.P., Whittington, A., 2006. Kinematic evolution of the Araçuaí - West Congo orogen in Brazil and Africa: nutcracker tectonics during the Neoproterozoic assembly of Gondwana. *Precambrian Res.* 149, 43- 64
- Alkmim, F. F., Marshak, S., 1998. Transamazonian orogeny in the Southern Sao Francisco craton region, Minas Gerais, Brazil: evidence for Paleoproterozoic collision and collapse in the Quadrilátero Ferrífero. *Precambrian Research*, 90(1-2), 29-58.
- Almeida, F.F.M., Brito Neves, B.B., Carneiro, C.D.R., 2000. Origin and evolution of the South American Platform. *Earth Sci. Rev.* 50, 77–111.
- Almeida, F.F.M., Hasui, Y., Brito Neves, B.B., Fuck, R.A., 1981. Brazilian structural provinces: an introduction. *Earth Sci. Rev.* 17, 1–29.
- Almeida, F. F. M., 1977. O cráton do São Francisco. *Revista Brasileira de geociências*, 7(4), 349-364.
- Alsdorf, D., Nelson, D., 1999. Tibetan satellite magnetic low: Evidence for widespread melt in the Tibetan crust?. *Geology*, 27(10), 943-946.
- Arbaret, L., Diot, H., Bouchez, J.L., Lespinasse, P., Saint-Blanquat, M., 1997. Analogue 3D simple-shear experiments of magmatic biotite subfabrics. In: Bouchez, J.-L., Hutton, D., Stephens, W.E. (Eds.), *Granite: from Segregation of Melt to Emplacement Fabrics, Petrology and Structural Geology Book Series*, vol. 8, pp. 129-143.
- Archanjo, C. J., Hollanda, M. H. B., Rodrigues, S. W., Neves, B. B., Armstrong, R., 2008. Fabrics of pre-and syntectonic granite plutons and chronology of shear zones in the Eastern Borborema Province, NE Brazil. *Journal of Structural Geology*, 30(3), 310-326.
- Archanjo, C. J., 2003. Anisotropia de suscetibilidade magnética aplicada às rochas ígneas máficas intrusivas [Tese de Livre Docência]: Instituto de Geociências, Universidade de São Paulo, São Paulo.
- Archanjo, C. J., Launeau, P., Bouchez, J. L., 1995. Magnetic fabric vs. magnetite and biotite shape fabrics of the magnetite-bearing granite pluton of Gameleiras (Northeast Brazil). *Physics of the Earth and Planetary Interiors*, 89(1-2), 63-75.
- Babinski, M., Pedrosa-Soares, A. C., Martins, M., Liu, D., Noce, C. M., Karfunkel, J., 2007. U–Pb SHRIMP dating of detrital zircons from the Macaúbas Group, southeast Brazil: Implications on the depositional age and provenance of pre-glacial and glaciogenic sediments. In *Symposium on Neoproterozoic-Early Palaeozoic Events in SW Gondwana* (Vol. 3, pp. 3-5).
- Babinski, M., Gradim, R. J., Pedrosa-Soares, A. C., de Alkmim, F. F., Noce, C. M., Liu, D., 2016. Geocronologia U-Pb (SHRIMP) e Sm-Nd de xistos verdes basálticos do Orógeno Araçuaí: implicações para a idade do Grupo Macaúbas. *Revista Brasileira de Geociências*, 35(4 sup), 77-81.

- Barboza, S. A., Bergantz, G. W., 1998. Rheological transitions and the progress of melting of crustal rocks. *Earth and Planetary Science Letters*, 158(1-2), 19-29.
- Beaumont, C., Nguyen, M. H., Jamieson, R. A., Ellis, S., 2006. Crustal flow modes in large hot orogens. *Geological Society, London, Special Publications*, 268(1), 91-145.
- Beaumont, C., Jamieson, R. A., Nguyen, M. H., Lee, B., 2001. Himalayan tectonics explained by extrusion of a low-viscosity crustal channel coupled to focused surface denudation. *Nature*, 414(6865), 738.
- Bento dos Santos, T. M., Tassinari, C. C., Fonseca, P. E., 2015. Diachronic collision, slab break-off and long-term high thermal flux in the Brasiliano–Pan-African orogeny: Implications for the geodynamic evolution of the Mantiqueira Province. *Precambrian Research*, 260, 1-22.
- Blumenfeld, P. and Bouchez, J.-L., 1988. Shear criteria in granite and migmatite deformed in the magmatic and solid states. *Journal of Structural Geology* 10, 361-372.
- Borradaile, G., Jackson, M., 2010. Structural geology, petrofabrics and magnetic fabrics (AMS, AARM, AIRM). *Journal of Structural Geology* 32, 1519-1551.
- Borradaile, G. J., Gauthier, D., 2003. Interpreting anomalous magnetic fabrics in ophiolite dikes. *Journal of Structural Geology*, 25(2), 171-182.
- Borradaile, G. J., Gauthier, D., 2006. Magnetic studies of magma-supply and sea-floor metamorphism: Troodos ophiolite dikes. *Tectonophysics*, 418(1-2), 75-92.
- Borradaile, G. J., Henry, B., 1997. Tectonic applications of magnetic susceptibility and its anisotropy. *Earth-Science Reviews*, 42(1-2), 49-93.
- Bouchez, J. L., 1997. Granite is never isotropic: an introduction to AMS studies of granitic rocks. In Bouchez, J. L., Hutton, D. H. W., Stepens, W.E. (Eds.), *Granite: from segregation of melt to emplacement fabrics. Petrology and Structural Geology*, vol. 8. Kluwer Academic Publishers, Dordrecht, pp. 95-112.
- Bouchez, J.L., 2000. Anisotropie de susceptibilité magnétique et fabriques des granites. *Comptes Rendus de L'Academie de Science* 330, 1–14.
- Brito Neves, B.B., Campos Neto, M.C., Fuck, R., 1999. From Rodinia to Western Gondwana: an approach to the Brasiliano/Pan-African cycle and orogenic collage. *Episodes* 22, 155–199.
- Brito Neves, B.B., Sá, J.M., Nilson, A.A., Botelho, N.F., 1996. A tafrogênese estateriana nos blocos paleoproterozóicos da América do Sul e processos subsequentes. *Geonomos* 3, 1–21
- Brito Neves, B. B., Cordani, U. G., 1991. Tectonic evolution of South America during the late Proterozoic. *Precambrian Research*, 53(1-2), 23-40.
- Brown, L. D., Zhao, W., Nelson, K. D., Hauck, M., Alsdorf, D., Ross, A., Cogan, M., Clark M., Liu X., Che, J., 1996. Bright spots, structure, and magmatism in southern Tibet from INDEPTH seismic reflection profiling. *Science*, 274(5293), 1688-1690.
- Bühn, B., Pimentel, M. M., Matteini, M., and Dantas, E. L., 2009. High spatial resolution analysis of Pb and U isotopes for geochronology by laser ablation multi-collector inductively coupled plasma mass spectrometry (LA-MC-ICP-MS). *Anais da Academia Brasileira de Ciências*, 81(1), 99-114.

- Butler, R.F., 1992. *Paleomagnetism: Magnetic Domains to Geologic Terranes*. Blackwell Scientific Publications, Boston. 319pp.
- Cagnard, F., Durrieu, N., Gapais, D., Brun, J. P., Ehlers, C., 2006. Crustal thickening and lateral flow during compression of hot lithospheres, with particular reference to Precambrian times. *Terra Nova*, 18(1), 72-78.
- Cavalcante, C., Fossen, H., de Almeida, R. P., Hollanda, M. H. B., Egydio-Silva, M., 2019. Reviewing the puzzling intracontinental termination of the Araçuaí-West Congo orogenic belt and its implications for orogenic development. *Precambrian Research*, 322, 85-98.
- Cavalcante, C., Hollanda, M. H., Vauchez, A., Kawata, M., 2018. How long can the middle crust remain partially molten during orogeny?. *Geology*, 46(10), 839-842.
- Cavalcante, G. C. G., Vauchez, A., Merlet, C., Egydio-Silva, M., Holanda, M. H., B., M., Boyer, B., 2014. Thermal conditions during deformation of partially molten crust from TitanQ geothermometry: rheological implications for the anatectic domain of the Araçuaí belt, eastern Brazil. *Solid Earth*, v. 5, 1223 - 1242.
- Cavalcante, G. C., Egydio-Silva, M., Vauchez, A., Camps, P., Oliveira, E., 2013. Strain distribution across a partially molten middle crust: insights from the AMS mapping of the Carlos Chagas Anatexite, Araçuaí belt (East Brazil). *Journal of Structural Geology*, 55, 79-100.
- Chardon, D., Gapais, D., Cagnard, F., 2009. Flow of ultra-hot orogens: a view from the Precambrian, clues for the Phanerozoic. *Tectonophysics*, 477(3-4), 105-118.
- Coleman, D. S., Gray, W., Glazner, A. F., 2004. Rethinking the emplacement and evolution of zoned plutons: Geochronologic evidence for incremental assembly of the Tuolumne Intrusive Suite, California. *Geology*, 32(5), 433-436.
- Cordani, U. G., D'Agrella-Filho, M. S., Brito-Neves, B. B. D., Trindade, R. I. F., 2003. Tearing up Rodinia: the Neoproterozoic palaeogeography of South American cratonic fragments. *Terra Nova*, 15(5), 350-359.
- Cruz, S. C., Alkmim, F. F., 2006. The tectonic interaction between the Paramirim Aulacogen and the Araçuaí belt, São Francisco craton region, Eastern Brazil. *Anais da Academia Brasileira de Ciências*, 78(1), 151-173.
- Cunningham, D., Alkmim, F. F., Marshak, S., 1998. A structural transect across the coastal mobile belt in the Brazilian Highlands (latitude 20 S): the roots of a Precambrian transpressional orogen. *Precambrian Research*, 92(3), 251-275.
- Day, R., Fuller, M., Schmidt, V. A., 1977. Hysteresis properties of titanomagnetites: grain-size and compositional dependence. *Physics of the Earth and planetary interiors*, 13(4), 260-267.
- Djama, L. M., Leterrier, J., Michard, A., 1992. Pb, Sr and Nd isotope study of the basement of the Mayumbian belt (Guena gneisses and Mfoubou granite, Congo): implications for crustal evolution in Central Africa. *Journal of African Earth Sciences (and the Middle East)*, 14(2), 227-237.
- Duarte, B. P., Valente, S. C., Heilbron, M., Neto, M. C., 2004. Petrogenesis of the orthogneisses of the Mantiqueira Complex, Central Ribeira Belt, SE Brazil: an Archaean to Palaeoproterozoic basement unit reworked during the Pan-African Orogeny. *Gondwana Research*, 7(2), 437-450.

- Duclaux, G., Rey, P., Guillot, S., Ménot, R.P., 2007. Orogen-parallel flow during continental convergence: numerical experiments and archaic field examples. *Geology*, 35, 715–718.
- Dunlop, D.J., Özdemir, O., 1997. *Rock Magnetism, Fundamentals and Frontiers*. Cambridge University Press, United Kingdom, p. 573.
- Dunlop, D.J., Özdemir, Ö., 2009. Magnetizations in rocks and minerals. In: Kono, M. (Ed.), *Treatise of Geophysics. Geomagnetism*, vol. 5. Elsevier, Amsterdam, 277–336 pp.
- Dussin, I. A., Dussin, T. M., 1995. Supergrupo Espinhaço: modelo de evolução geodinâmica. *Revista Geonomos*, 3(1).
- Egydio-Silva, M., Vauchez, A., Fossen, H., Cavalcante, G. C. G., Xavier, B. C., 2018. Connecting the Araçuaí and Ribeira belts (SE–Brazil): Progressive transition from contractional to transpressive strain regime during the Brasiliano orogeny. *Journal of South American Earth Sciences*.
- Egydio-Silva, M., Vouchez, A., 2011. Connecting the Araçuaí and Ribeira Belts (SE Brasil): Progressive Transition from Contractional to Transpressive Strain Regime During the Brasiliano Orogeny. In: *GONDWANA 14, Búzios*. Abstract v. 1 p. 120 – 120.
- Egydio-Silva, M., Vauchez, A., Raposo, M.I.B., Bascou, J., Uhlein, A., 2005. Deformation regime variations in an arcuate transpressional orogen (Ribeira belt, SE Brazil) imaged by anisotropy of magnetic susceptibility in granulites. *Journal of Structural Geology* 27, 1750-1764.
- Egydio-Silva, M., Vauchez, A., Bascou, J., Hippertt, J., 2002. High-temperature deformation in the Neoproterozoic transpressional Ribeira belt, southeast Brazil. *Tectonophysics*, 352(1-2), 203-224.
- Ellwood, B.B., 1982. Estimates of flow direction for calc-alkaline welded tuffs and paleomagnetic data reliability from anisotropy of magnetic susceptibility measurements; central San Juan Mountains, Southwest Colorado. *Earth and Planetary Science Letters* 59, 303–314.
- Faccenda, M., Gerya, T.V., Chakraborty, S., 2008. Styles of post subduction collisional orogeny: influence of convergence velocity, crustal rheology and radiogenic heat production. *Lithos* 103 (1–2), 257–287.
- Faure, G., Mensing, T. M., 2005. *Isotopes: principles and applications*. Wiley-Blackwell.
- Faria, L. D., 1997. Controle e tipologia de mineralizações de grafita flake do nordeste de Minas Gerais e sul da Bahia: uma abordagem regional [Dissertação de Mestrado]: Instituto de Geociências, Universidade Federal de Minas Gerais, 112p.
- Ferré, E. C., 2002. Theoretical models of intermediate and inverse AMS fabrics. *Geophysical Research Letters*, 29(7), 31-1.
- Figueiredo, M.C.H., Teixeira, W. 1996. The Mantiqueira Metamorphic Complex, eastern Minas Gerais State: preliminary geochronological and geochemical results. *Anais da Academia Brasileira de Ciências*, 68, 223–246.
- Fischel, D.P., 1998. Geologia e dados isotópicos Sm-Nd do Complexo Mantiqueira e do Cinturão Ribeira na região de Abre Campo, Minas Gerais [Dissertação de Mestrado]: Universidade de Brasília, Brazil.
- Fossen, H., Cavalcante, G., Almeida, R. P., 2017. Hot Versus Cold Orogenic Behavior: Comparing the Araçuaí–West Congo and the Caledonian Orogens. *Tectonics*, 36(10), 2159-2178.

- Gapais, D., Cagnard, F., Gueydan, F., Barbey, P., Ballevre, M., 2009. Mountain building and exhumation processes through time: inferences from nature and models. *Terra Nova*, 21(3), 188-194.
- Glazner, A. F., Bartley, J. M., Coleman, D. S., Gray, W., Taylor, R. Z., 2004. Are plutons assembled over millions of years by amalgamation from small magma chambers?. *GSA today*, 14(4/5), 4-12.
- Gonçalves, L., Alkmim, F. F., Pedrosa-Soares, A. C., Dussin, I. A., Valeriano, C. D. M., Lana, C., Tedeschi, M., 2015. Granites of the intracontinental termination of a magmatic arc: an example from the Ediacaran Araçuaí orogen, southeastern Brazil. *Gondwana Research*, 36, 439-458.
- Gonçalves, L., Farina, F., Lana, C., Pedrosa-Soares, A. C., Alkmim, F., Nalini, H. A., 2014. New U–Pb ages and lithochemical attributes of the Ediacaran Rio Doce magmatic arc, Araçuaí confined orogen, southeastern Brazil. *Journal of South American Earth Sciences*, 52, 129-148.
- Gradim, C., Roncato, J., Pedrosa-Soares, A. C., Cordani, U., Dussin, I., Alkmim, F. F., Queiroga, G., Jacobsohn, T., da Silva, L. C., Babinski, M., 2014. The hot back-arc zone of the Araçuaí orogen, Eastern Brazil: from sedimentation to granite generation. *Brazilian Journal of Geology*, 44(1), 155-180.
- Gradim, R.J., Alkmim, F.F., Pedrosa-Soares, A.C., Babinski, M., Noce, C.M. 2005. Xistos Verdes do Alto Araçuaí, Minas Gerais: Vulcanismo Básico do Rife Neoproterozóico Macaúbas. *Revista Brasileira de Geociências*, 35 (4-suplemento): 59-69.
- Guerrero-Suarez, S., Martín-Hernández, F., 2016. Haematite natural crystals: non-linear initial susceptibility at low temperature. *Geophysical Journal International*, 205(3), 1886-1899.
- Harrison, R. J., Muraszko, J., Heslop, D., Lascu, I., Muxworthy, A. R., Roberts, A. P., 2018. An improved algorithm for unmixing first-order reversal curve diagrams using principal component analysis. *Geochemistry, Geophysics, Geosystems*, 19(5), 1595-1610.
- Harrison, R. J., Feinberg, J. M., 2008. FORCinel: An improved algorithm for calculating first-order reversal curve distributions using locally weighted regression smoothing. *Geochemistry, Geophysics, Geosystems*, 9(5).
- Hasui, Y., Carneiro, C.D.R., Coimbra, A.M., 1975. The Ribeira Folded Belt. *Rev. Bras Geoc.*, (São Paulo), 5(4): 257-266.
- Heilbron, M., Pedrosa-Soares, A.C., Neto, M., da Silva, L., Trouw, R., Janasi, V. 2004. Brasiliano Orogens in Southeast and South Brazil. In: Wienberg, R., Trouw, R., and Hackspacher, P. (Eds.), *The 750–550 Ma Brasiliano Event of South America*. *J. Virtual Explorer. Electronic Edition* 17, Paper 4.
- Heilbron, M., Machado, N., 2003. Timing of terrane accretion in the Neoproterozoic–Eopaleozoic Ribeira orogen (SE Brazil). *Precambrian Research*, 125(1-2), 87-112.
- Hodges, K.V., Parrish, R.R., and Searle, M.P., 1996. Tectonic evolution of the central Annapurna Range: Nepalese Himalaya: *Tectonics*, v. 15, p. 1264–1291.
- Horton, F., Hacker, B., Kylander-Clark, A., Holder, R., Jöns, N., 2016. Focused radiogenic heating of middle crust caused ultrahigh temperatures in southern Madagascar. *Tectonics* 35, 293–314.

- Hoskin, P. W., Schaltegger, U., 2003. The composition of zircon and igneous and metamorphic petrogenesis. *Reviews in mineralogy and geochemistry*, 53(1), 27-62.
- Hrouda, F., Ježek, J., 2017. Role of single-domain magnetic particles in creation of inverse magnetic fabrics in volcanic rocks: A mathematical model study. *Studia Geophysica et Geodaetica*, 61(1), 145-161.
- Hrouda, F., 1982. Magnetic-anisotropy of rocks and its application in geology and geophysics. *Geophysical Surveys* 5 (1), 37-82.
- Jackson S.E., Pearson N.J., Griffin W.L., Belousova E.A., 2004. The application of laser ablation inductively coupled plasma mass spectrometry to in situ U-Pb zircon geochronology. *Chem Geol* 211: 47–69
- Jackson, S. E., Pearson, N. J., Griffin, W. L., Belousova, E. A., 2004. The application of laser ablation-inductively coupled plasma-mass spectrometry to in situ U–Pb zircon geochronology. *Chemical Geology*, 211(1-2), 47-69.
- Jackson, M., 1991. Anisotropy of magnetic remanence: a brief review of mineralogical sources, physical origins, and geological applications, and comparison with susceptibility anisotropy. *Pure and Applied Geophysics*, 136(1), 1-28.
- Jamieson, R. A., Unsworth, M. J., Harris, N. B., Rosenberg, C. L., Schulmann, K., 2011. Crustal melting and the flow of mountains. *Elements*, 7(4), 253-260.
- Jamieson, R.A., Beaumont, C., Fullsack, P., Lee, B., 1998. Barrovian regional metamorphism: where 's the heat? *Geological Society Special Publications* 138, 23 –51.
- Jelinek, V., 1978. Statistical processing of anisotropy of magnetic susceptibility measured on groups of specimens. *Studia Geophysica et Geodaetica* 22.
- Jelinek, V., 1981. Characterization of the magnetic fabric of rocks. *Tectonophysics* 79, T63-T67.
- Kawata, M. T., 2014. Geocronologia de zircão na suite granítica Carlos Chagas, Faixa Araçuaí [Trabalho de Formatura]: Instituto de Geociências da Universidade de São Paulo, 33 pp.
- Kirkland, C. L., Smithies, R. H., Taylor, R. J. M., Evans, N., McDonald, B., 2015. Zircon Th/U ratios in magmatic environs. *Lithos*, 212, 397-414.
- Launeau, P., Cruden, A. R., 1998. Magmatic fabric acquisition mechanisms in a syenite: results of a combined anisotropy of magnetic susceptibility and image analysis study. *Journal of Geophysical Research: Solid Earth*, 103(B3), 5067-5089.
- Lima, S. A. A., Martins-Neto, M. A., Pedrosa-Soares, A. C., Cordani, U. G., Nutman, A., 2016. A Formação Salinas na área-tipo, NE de Minas Gerais: Uma proposta de revisão da estratigrafia da Faixa Araçuaí com base em evidências sedimentares, metamórficas e idades U-Pb SHRIMP. *Revista Brasileira de Geociências*, 32(4), 491-500.
- Lowrie, W., 1997. *Fundamentals of geophysics*. Cambridge university press, Cambridge, New York.
- Ludwig, K. R., 2003. User's manual for isoplot 3.00, a geochronological toolkit for microsoft excel. *Berkeley Geochronl. Cent. Spec. Publ.*, 4, 25-32.
- Machado, N., Schrank, A., Abreu, F.R., Knauer, L.G., Almeida-Abreu, P.A., 1989. Resultados preliminares da geocronologia UPb na Serra do Espinhaço Meridional. *Boletim do Núcleo Minas Gerais-Sociedade Brasileira de Geologia*, 10: 171-174.

- Maffione, M., Hernandez-Moreno, C., Ghiglione, M. C., Speranza, F., van Hinsbergen, D. J., Lodolo, E., 2015. Constraints on deformation of the Southern Andes since the Cretaceous from anisotropy of magnetic susceptibility. *Tectonophysics*, 665, 236-250.
- Martins V.T.S., Teixeira W., Noce C.M., Pedrosa-Soares A.C., 2004. Sr and Nd characteristics of Brasiliano-Pan African granitoid plutons of the Araçuaí orogen, southeastern Brazil: Tectonic implications. *Gondwana Research*, 7: 75-89.
- Martins-Neto, M. A., 2000. Tectonics and sedimentation in a paleo/mesoproterozoic rift-sag basin (Espinhaço basin, southeastern Brazil). *Precambrian Research*, 103(3-4), 147-173.
- Martín-Hernández, F., Lüneburg, C. M., Aubourg, C., Jackson, M., 2004. Magnetic fabric: methods and applications - an introduction. Geological Society, London, Special Publications, 238(1), 1-7.
- Meira, V. T., García-Casco, A., Juliani, C., Almeida, R. P., Schorscher, J. H. D., 2015. The role of intracontinental deformation in supercontinent assembly: insights from the Ribeira Belt, Southeastern Brazil (Neoproterozoic West Gondwana). *Terra Nova*, 27(3), 206-217.
- Mondou, M., Egydio-Silva, M., Vauchez, A., Raposo, M. I. B., Bruguier, O., Oliveira, A. F., 2012. Complex, 3D strain patterns in a synkinematic tonalite batholith from the Araçuaí Neoproterozoic orogen (Eastern Brazil): evidence from combined magnetic and isotopic chronology studies. *Journal of Structural Geology*, 39, 158-179.
- Mondou, M., 2010. Evolução estrutural e térmica de um batólito sin-cinematismo no orógeno Neoproterozóico Araçuaí (leste do Brasil) [Tese de Doutorado]: Instituto de Geociências, Universidade de São Paulo, São Paulo.
- Monié, P., Bosch, D., Bruguier, O., Vauchez, A., Rolland, Y., Nsungani, P. and Buta Neto, A., 2012. The Late Neoproterozoic/Early Palaeozoic evolution of the West Congo Belt of NW Angola: geochronological (U-Pb and Ar-Ar) and petrostructural constraints. *Terra Nova* 24, 238-247.
- Moraes, R., Nicollet, C., Barbosa, J. S. F., Fuck, R. A., Sampaio, A. R., 2015. Applications and limitations of thermobarometry in migmatites and granulites using as an example rocks of the Araçuaí Orogen in southern Bahia, including a discussion on the tectonic meaning of the current results. *Brazilian Journal of Geology*, 45(4), 517-539.
- Moreira, M. D., 2000. Mapa Geológico da Folha Mucuri, SE.24-V-C-V, Escala 1:1000.000. Projeto Leste-MG. SEME/COMIG/CPRM, Belo Horizonte, Brazil.
- Munhá, J. M., Cordani, U. G., Tassinari, C. C., Palácios, T., 2005. Petrologia e termocronologia de gnaisses migmatíticos da Faixa de Dobramentos Araçuaí (Espírito Santo, Brasil). *Revista Brasileira de Geociências*, 35(1), 123-134.
- Nalini, H.A., Bilal, E. and Correia Neves, J.M., 2000. Syn-collisional peraluminous magmatism in the Rio Doce region: mineralogy, geochemistry and isotopic data of the neoproterozoic Urucum suite (eastern Minas Gerais state, Brazil). *Revista Brasileira de Geociências* 30, 120-125.
- Narduzzi, F., Farina, F., Stevens, G., Lana, C., Nalini, H. A., 2017. Magmatic garnet in the Cordilleran-type Galiléia granitoids of the Araçuaí belt (Brazil): Evidence for crystallization in the lower crust. *Lithos*, 282, 82-97.
- Nédélec, A., Bouchez, J. L., 2015. *Granites: petrology, structure, geological setting, and metallogeny*. OUP Oxford.

- Nelson, K.D., Wenjin Zhao, Brown, L.D., Kuo, J., Jinkai Che, Xianwen Liu, Klemperer, S.L., Makovsky, Y., Melssner, R., Mechie, J., Kind, R., Wenzel, F., Ni, J., Nabele, J., Chen Leshou, Handong Tan, Wenbo Wie, Jones, A.G., Booker, J., Unsworth, M., Kidd, W.S.F., Hauck, M., Alsdorf, D., Ross, A., Cogan, M., Changde Wu, Sandvol, E., Edwards, M., 1996. Partially molten middle crust beneath Southern Tibet Synthesis of project INDEPTH results. *Science*, 74:1684 - 1688.
- Noce, C. M., Soares, A. C. P., Silva, L. C. D., Alkmim, F. F. D., 2007a. O embasamento arqueano e paleoproterozóico do orógeno Araçuaí. *Geonomos.*, 15(1), 17-23.
- Noce, C. M., Pedrosa-Soares, A. C., da Silva, L. C., Armstrong, R., Piuzana, D., 2007b. Evolution of polycyclic basement complexes in the Araçuaí Orogen, based on U–Pb SHRIMP data: Implications for Brazil–Africa links in Paleoproterozoic time. *Precambrian Research*, 159(1-2), 60-78.
- Noce, C. M., Macambira, M. J. B., Pedrosa-Soares, A. C., 2000. Chronology of Neoproterozoic-Cambrian granitic magmatism in the Araçuaí Belt, Eastern Brazil, based on single zircon evaporation dating. *Revista Brasileira de Geociências*, 30(1), 025-029.
- Noce, C.M., Pedrosa-Soares, A.C., Grossi-Sad, J.H., Baars, F.J., Guimarães, M.V., Mourão, M.A.A., Oliveira, M.J.R., Roque, N.C., 1997. Nova Subdivisão Estratigráfica Regional do Grupo Macaúbas na Faixa Araçuaí: O Registro de uma Bacia Neoproterozóica. *Boletim do Núcleo Minas Gerais-Sociedade Brasileira de Geologia*, 14: 29-31.
- Novo, T. A., Pedrosa-Soares, A., Vieira, V. S., Dussin, I., da Silva, L. C., 2018. The Rio Doce Group revisited: An Ediacaran arc-related volcano-sedimentary basin, Araçuaí orogen (SE Brazil). *Journal of South American Earth Sciences*, 85, 345-361.
- Oliveira, F. V. D., 2015. Chronus: um novo suplemento para a redução de dados U-Pb obtidos por LA-MC-ICPMS [Dissertação de Mestrado]: Instituto de Geociências, Universidade de Brasília, 108 pp.
- Oliveira, A. F., 2008. Tonalitos Galiléia e São Vitor: uma abordagem predominantemente estrutural através da anisotropia de susceptibilidade magnética (ASM) [Trabalho de Formatura]: Instituto de Geociências da Universidade de São Paulo, 53 pp.
- Oliveira, M. J. R., Pinto, C. P., Féboli, W. L., dos Santos, A., 2000. Projeto Leste - Relatório mapa integrado 1: 500.000 - Geologia estrutural e tectônica. CPRM—COMIG, Belo Horizonte.
- Orlický, O., 1990. Detection of magnetic carriers in rocks: results of susceptibility changes in powdered rock samples induced by temperature. *Physics of the Earth and Planetary Interiors*, 63(1-2), 66-70.
- Paes, V. J. C., 2000. Mapa Geológico da Folha Teófilo Otoni, SE.24-V-C-IV, Escala 1:1000.000. Projeto Leste-MG. SEME/COMIG/CPRM, Belo Horizonte, Brazil.
- Park, Y. H., Doh, S. J., Kim, W., Suk, D., 2005. Deformation history inferred from magnetic fabric in the southwestern Okcheon metamorphic belt, Korea. *Tectonophysics*, 405(1-4), 169-190.
- Parry, G. R., 1971. The magnetic anisotropy of some deformed rocks. Doctoral dissertation. University of Birmingham, 218 pp.
- Parsons, A. J., Ferré, E. C., Law, R. D., Lloyd, G. E., Phillips, R. J., Searle, M. P., 2016. Orogen-parallel deformation of the Himalayan midcrust: Insights from structural and magnetic fabric analyses of the Greater Himalayan Sequence, Annapurna-Dhaulagiri Himalaya, central Nepal. *Tectonics*, 35(11), 2515-2537.

- Partzsch, G. M., Schilling, F. R., Arndt, J., 2000. The influence of partial melting on the electrical behavior of crustal rocks: laboratory examinations, model calculations and geological interpretations. *Tectonophysics*, 317(3-4), 189-203.
- Passchier, C. W., Trouw, R. A., 2005. *Microtectonics* (Vol. 1). Springer Science & Business Media.
- Pedrosa-Soares, A. C., de Campos, C. P., Noce, C., Silva, L. C., Novo, T., Roncato, J., Medeiros, S., Castañeda, C., Queiroga, G., Dantas, E., Dussin, I., Alkmim, F., 2011. Late Neoproterozoic-Cambrian granitic magmatism in the Araçuaí orogen (Brazil), the Eastern Brazilian Pegmatite Province and related mineral resources. Geological Society, London, Special Publications, 350(1), 25-51.
- Pedrosa-Soares, A. C., Alkmim, F. F., Tack, L., Noce, C. M., Babinski, M., Silva, L. C. D., Martins-Neto, M. A., 2008. Similarities and differences between the Brazilian and African counterparts of the Neoproterozoic Araçuaí-West Congo orogen. Geological Society, London, Special Publications, 294(1), 153-172.
- Pedrosa-Soares, A. C., Noce, C. M. et al. 2007. Orógeno Araçuaí: síntese do conhecimento 30 anos após Almeida 1977. *Geonomos*, 15, 1–16.
- Pedrosa-Soares, A. C., Noce, C. M., Wiedemann, C. M., Pinto, C. P., 2001. The Araçuaí-West-Congo Orogen in Brazil: an overview of a confined orogen formed during Gondwanaland assembly. *Precambrian research*, 110(1-4), 307-323.
- Pedrosa-Soares, A. C., Wiedemann-Leonardos, C. M., 2000. Evolution of the Araçuaí Belt and its connection to the Ribeira Belt, Eastern Brazil. *Tectonic Evolution of South America*, 31, 265-310.
- Pedrosa-Soares, A.C., Cordani, U., Nutman, A., 2000. Constraining the age of Neoproterozoic glaciation in eastern Brazil: First U-Pb SHRIMP data from detrital zircons. *Revista Brasileira de Geociências*, 30: 58-61.
- Pedrosa-Soares, A.C., Vidal, P., Leonardos, O. H., Brito Neves, B. B., 1998. Neoproterozoic oceanic remnants in eastern Brazil: further evidence and refutation of an exclusively ensialic evolution for the Araçuaí–West Congo Orogen. *Geology*, 26(6), 519-522.
- Pedrosa-Soares, A.C., Noce, C.M., 1998. Where is the suture zone of the Neoproterozoic Araçuaí-West-Congo orogen? In: Conference on Basement Tectonics, 14, Ouro Preto. UFOP, Extended Abstracts, p. 35-37
- Pedrosa-Soares, A. C., Noce, C. M., Vidal, P., Monteiro, R. L. B. P., Leonardos, O. H., 1992. Toward a new tectonic model for the late proterozoic Araçuaí (SE Brazil)-West Congolian (SW Africa) belt. *Journal of South American Earth Sciences*, 6(1-2), 33-47.
- Petitgirard, S., Vauchez, A., Egydio-Silva, M., Bruguier, O., Camps, P., Monié, P., Babinsky, M., Mondou, M., 2009. Conflicting structural and geochronological data from the Ibituruna quartz-syenite (SE Brazil): Effect of protracted “hot” orogeny and slow cooling rate?. *Tectonophysics*, 477(3-4), 174-196.
- Pinto, C. P., Drumond, J. B. V., Feboli, W. L., 1997. Projeto Leste: Geologia-Nota Explicativa do Mapa Geológico Integrado, escala 1:500.000. Etapa I. SEME/COMIG/UFMG. Belo Horizonte, 161 pp.
- Pinto, N. S., 2015. Caracterização estrutural e geocronológica do Tonalito São Vitor, nas proximidades de Campanário –MG, através de Anisotropia de Suscetibilidade Magnética e U-Pb em zircão [Trabalho de Formatura]: Instituto de Geociências da Universidade de São Paulo, 64 pp.

- Portela, B. V., 2013. O Tonalito São Vitor nos arredores de Teófilo Otoni (MG): uma abordagem petrográfica e estrutural por ASM [Trabalho de Formatura]: Instituto de Geociências da Universidade de São Paulo, 44 pp.
- Potter, D. K., Stephenson, A., 1988. Single-domain particles in rocks and magnetic fabric analysis. *Geophysical Research Letters*, 15(10), 1097-1100.
- Pous, J., Munoz, J. A., Ledo, J. J., Liesa, M., 1995. Partial melting of subducted continental lower crust in the Pyrenees. *Journal of the Geological Society*, 152(2), 217-220.
- Putnis, A., 1992. *An introduction to mineral sciences*. Cambridge University Press.
- Queiroga, G. N., Pedrosa-Soares, A. C., Noce, C. M., Alkmim, F. F., Pimentel, M. M., Dantas, E., Martins, M., Castañeda, C., Suíta, M.T.F., Prichard, H., 2007. Age of the Ribeirão da Folia Ophiolite, Araçuaí Orogen: the U-Pb zircon (LA-ICPMS) dating of a plagiogranite. *Geonomos*, 15(1), 61-65.
- Queiroga, G.N., Pedrosa-Soares, A.C., Quéméneur, J., Castañeda, C., 2006. A unidade metassedimentar do ofiolito de Ribeirão da Folha, Orógeno Araçuaí, Minas Gerais: petrografia, geotermobarometria e calcografia. *Geonomos*, 14 (1): 25-35.
- Raposo, M. I. B., 2017. Magnetic fabrics of the Cretaceous dike swarms from São Paulo coastline (SE Brazil): its relationship with South Atlantic Ocean opening. *Tectonophysics*, 721, 395-414.
- Raposo, M. I. B., Gastal, M. C. P., 2009. Emplacement mechanism of the main granite pluton of the Lavras do Sul intrusive complex, South Brazil, determined by magnetic anisotropies. *Tectonophysics*, 466(1-2), 18-31.
- Raposo, M. I. B., Berquó, T. S., 2008. Tectonic fabric revealed by AARM of the proterozoic mafic dike swarm in the Salvador city (Bahia State): São Francisco Craton, NE Brazil. *Physics of the Earth and Planetary Interiors*, 167(3-4), 179-194.
- Raposo, M. I. B., McReath, I., D'Agrella-Filho, M. S., 2006. Magnetic fabrics, rock magnetism, cathodoluminescence and petrography of apparently undeformed Bambuí carbonates from São Francisco Basin (Minas Gerais State, SE Brazil): An integrated study. *Tectonophysics*, 418(1-2), 111-130.
- Rey, P., Vanderhaeghe, O., Teyssier, C., 2001. Gravitational collapse of the continental crust: definition, regimes and modes. *Tectonophysics*, 342(3-4), 435-449.
- Richter, F., Lana, C., Stevens, G., Buick, I., Pedrosa-Soares, A. C., Alkmim, F. F., Cutts, K., 2016. Sedimentation, metamorphism and granite generation in a back-arc region: Records from the Ediacaran Nova Venécia Complex (Araçuaí Orogen, Southeastern Brazil). *Precambrian Research*, 272, 78-100.
- Rochette, P., Jackson, M., Aubourg, C., 1992. Rock magnetism and the interpretation of anisotropy of magnetic susceptibility. *Reviews of Geophysics*, 30(3), 209-226.
- Roncato, J.G., 2009. As suítes graníticas tipo-S do norte do Espírito Santo na região das folhas Ecoporanga, Mantena, Montanha e Nova Venécia [Dissertação de Mestrado]: Universidade Federal de Minas Gerais, Belo Horizonte, 102p.
- Rosenberg, C.L., Medvedev, S. and Handy, M.R., 2007. On the effects of melting on continental deformation and faulting. In: M. Handy, G. Hirth and N. Hovius (Editors), *Tectonic Faults: Agents of Change on a Dynamic Earth*. Dahlem Workshop Report, MIT Press, pp. 357-402.

- Rosenberg, C. L., Handy, M. R., 2005. Experimental deformation of partially melted granite revisited: implications for the continental crust. *Journal of metamorphic Geology*, 23(1), 19-28.
- Rosenberg, C. L., Handy, M. R., 2000. Syntectonic melt pathways during simple shearing of a partially molten rock analogue (Norcamphor-Benzamide). *Journal of Geophysical Research: Solid Earth*, 105(B2), 3135-3149.
- Sandiford, M., McLaren, S., 2002. Tectonic feedback and the ordering of heat producing elements within the continental lithosphere. *Earth Planet. Sci. Lett.* 204, 133 –150.
- Salazar, C. A., Bustamante, C., Archanjo, C. J., 2016. Magnetic fabric (AMS, AAR) of the Santa Marta batholith (northern Colombia) and the shear deformation along the Caribbean Plate margin. *Journal of South American Earth Sciences*, 70, 55-68.
- Sanchez, E. S., 2014. Contribuição estrutural e geocronológica aos metassedimentos da Formação Tumiritinga entre os municípios de Itambacuri e Frei Serafim, MG. [Trabalho de Formatura]: Instituto de Geociências da Universidade de São Paulo, 63 pp.
- Schmitt, R.S., Trouw, R.A.J., Van Schmus, W.R. and Pimentel, M.M., 2004. Late amalgamation in the central part of West Gondwana: new geochronological data and the characterization of a Cambrian collisional orogeny in the Ribeira Belt (SE Brazil). *Precambrian Research* 133, 29–61.
- Seidensticker, U., Wiedemann, C. M., 1992. Geochemistry and origin of lower crustal granulite facies rocks in the Serra do Caparaó region, Espírito Santo/Minas Gerais, Brazil. *Journal of South American earth sciences*, 6(4), 289-298.
- Siga Jr., O., 1986. A evolução geotectônica da porção nordeste de Minas Gerais, com base em interpretações geocronológicas [Dissertação de Mestrado]: Universidade de São Paulo. 155p.
- Signorelli, N., 2000. Mapa Geológico da Folha Itambacuri, SE-24-Y-A-I, Escala 1:100.000. Programa Levantamentos Geológicos Básicos do Brasil. DNPM/CPRM, Belo Horizonte, Brazil.
- Silva, L. D., Pedrosa-Soares, A. C., Teixeira, L. R., Armstrong, R., 2008. Tonian rift-related, A-type continental plutonism in the Araçuaí Orogen, eastern Brazil: new evidence for the breakup stage of the São Francisco–Congo Paleococontinent. *Gondwana Research*, 13(4), 527-537.
- Silva, L. C., McNaughton, N. J., Armstrong, R., Hartmann, L. A., Fletcher, I. R., 2005. The Neoproterozoic Mantiqueira Province and its African connections: a zircon-based U–Pb geochronologic subdivision for the Brasiliano/Pan-African systems of orogens. *Precambrian Research*, 136(3-4), 203-240.
- Stephenson, A., Sadikun, S. T., Potter, D. K., 1986. A theoretical and experimental comparison of the anisotropies of magnetic susceptibility and remanence in rocks and minerals. *Geophysical Journal International*, 84(1), 185-200.
- Tack, L., Wingate, M.T.D., Liégois, J.-P., Fernandez-Alonso, M., Deblond, A., 2001. Early Neoproterozoic magmatism (1000 –910 Ma) of the Zadinian and Mayumbian Groups (Bas-Congo): onset of Rodinia rifting at the western edge of the Congo craton. *Precamb. Res.* 110 (1 –4), 277 –306. [https://doi.org/10.1016/S0301-9268\(01\)00192-9](https://doi.org/10.1016/S0301-9268(01)00192-9).
- Tarling, D.H., Hrouda, F., 1993. *The Magnetic Anisotropy of Rocks*. Chapman and Hall, London. 217 p.

- Tedeschi, M., Novo, T., Pedrosa-Soares, A. C., Dussin, I., Tassinari, C., Silva, L. C., Gonçalves, L., Alkmim, F., Lana, C., Figueiredo, C., Dantas, E., Medeiros, S., Campos, C., Corrales, F., Heilbron, M., 2016. The Ediacaran Rio Doce magmatic arc revisited (Araçuaí-Ribeira orogenic system, SE Brazil). *Journal of South American Earth Sciences*, 68, 167-186.
- Tedeschi, M., 2013. Caracterização do arco magmático do Orógeno Araçuaí entre Frei Inocência e Itambacuri, Minas Gerais [Dissertação de Mestrado]: Universidade Federal de Minas Gerais, Belo Horizonte, Brasil, 126p.
- Tedeschi M., Pedrosa-Soares A.C., Piuzana D., Noce C., 2012. Caracterização do Arco Magmático do Orógeno Araçuaí entre Frei Inocência e Itambacuri, MG. In: 46 Congresso Brasileiro de Geologia, 2012, Santos, SP. Anais. São Paulo: Sociedade Brasileira de Geologia, 2012.
- Toledo, A. P., 2015. Anisotropia de Suscetibilidade Magnética e Geocronologia do charnoquito na região de Barra de São Francisco – ES [Trabalho de Formatura]: Instituto de Geociências da Universidade de São Paulo, 29 pp.
- Trindade, R. I., Bouchez, J. L., Bolle, O., Nédélec, A., Peschler, A., Poitrasson, F., 2001. Secondary fabrics revealed by remanence anisotropy: methodological study and examples from plutonic rocks. *Geophysical Journal International*, 147(2), 310-318.
- Trindade, R. I., Raposo, M. I. B., Ernesto, M., Siqueira, R., 1999. Magnetic susceptibility and partial anhysteretic remanence anisotropies in the magnetite-bearing granite pluton of Tourao, NE Brazil. *Tectonophysics*, 314(4), 443-468.
- Trompette, R., 1997. Neoproterozoic (~ 600 Ma) aggregation of Western Gondwana: a tentative scenario. *Precambrian Research*, 82(1-2), 101-112.
- Trompette, R., 1994. *Geology of Western Gondwana (2000–500 Ma)*. Balkema, Rotterdam, 350.
- Trompette, R., Uhlein, A., Da Silva, M. E., Karmann, I., 1992. The Brasiliano São Francisco craton revisited (central Brazil). *Journal of South American Earth Sciences*, 6(1-2), 49-57.
- Tuller, M.P., 2000. Mapa Geológico da Folha Ataléia, SE.24-Y-A-II, Escala 1:100.000. Projeto Leste-MG. SEME/COMIG/CPRM, Belo Horizonte, Brazil.
- Uhlein, A., Trompette, R. R., Egydio-Silva, M., Vauchez, A., 2007. A glaciação sturtiana (~ 750 Ma), a estrutura do rifte Macaúbas-Santo Onofre ea estratigrafia do Grupo Macaúbas, Faixa Araçuaí. *Revista Geonomos*, 15(1).
- Uhlein, A., Trompette, R. R., Egydio-Silva, M., 1998. Proterozoic rifting and closure, SE border of the São Francisco Craton, Brazil. *Journal of South American Earth Sciences*, 11(2), 191-203.
- Vanderhaeghe, O., Teyssier, C., 2001. Partial melting and flow of orogens. *Tectonophysics*, 342(3-4), 451-472.
- Vauchez, A., Tommasi, A., 2003. Wrench faults down to the asthenosphere: Geological and geophysical evidence and thermomechanical effects. Geological Society, London, Special Publications, 210(1), 15-34.
- Vauchez, A., Egydio-Silva, M., Babinski, M., Tommasi, A., Uhlein, A., Liu, D., 2007. Deformation of a pervasively molten middle crust: insights from the neoproterozoic Ribeira-Araçuaí orogen (SE Brazil). *Terra Nova*, 19(4), 278-286.

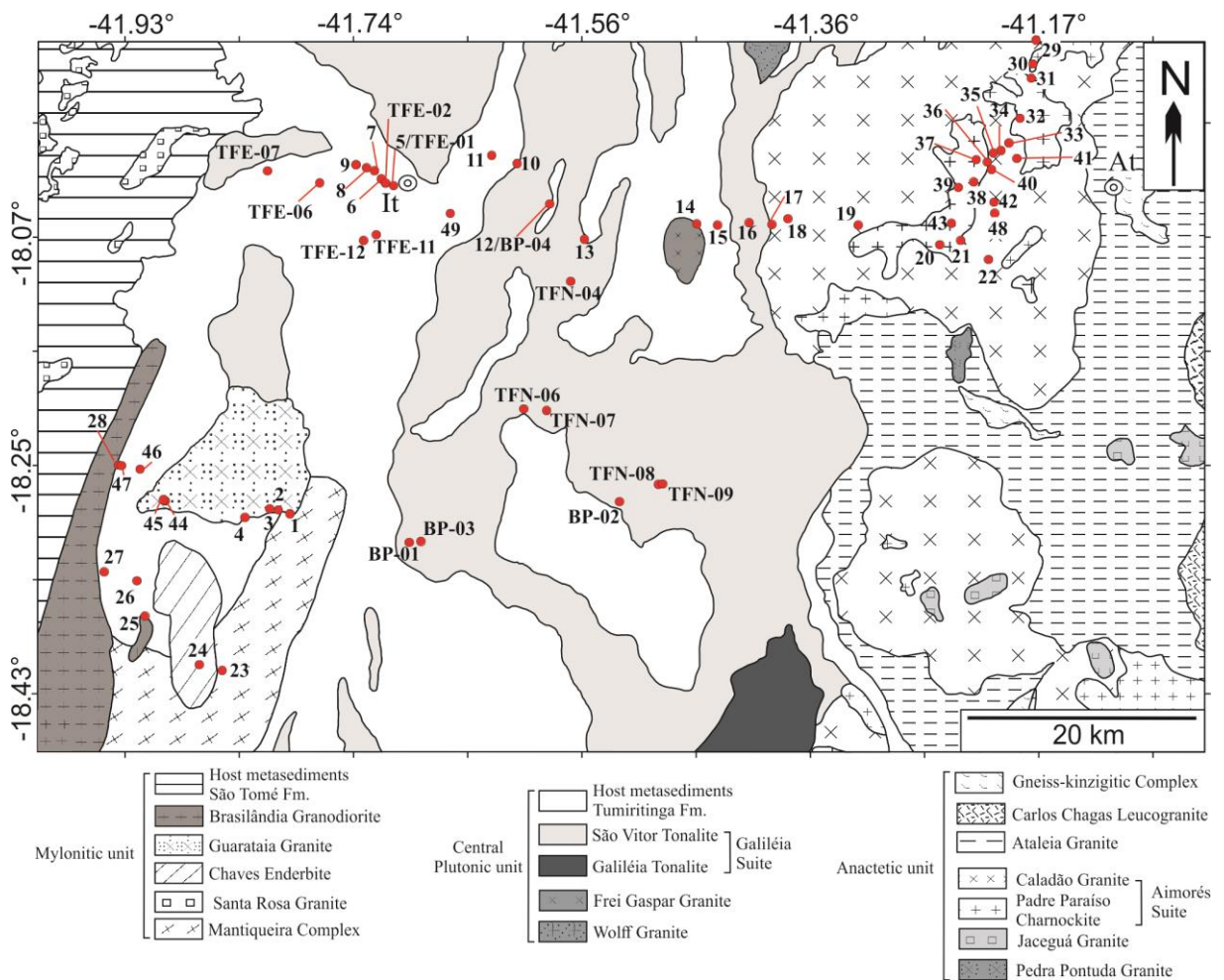
- Vaucher, A., Tommasi, A., Egydio-Silva, M., 1994. Self-indentation of a heterogeneous continental lithosphere. *Geology*, 22(11), 967-970.
- Vernon, R. H., 2000. Review of microstructural evidence of magmatic and solid-state flow. *Visual Geosciences*, 5(2), 1-23.
- Vieira, V. S., 2007. Significado do grupo Rio Doce no contexto do Orógeno Araçuaí [Tese de Doutorado]: Instituto de Geociências da Universidade Federal de Minas Gerais, 117 pp.
- Vigneresse, J. L., Barbey, P., Cuney, M., 1996. Rheological transitions during partial melting and crystallization with application to felsic magma segregation and transfer. *Journal of Petrology*, 37(6), 1579-1600.
- Xavier, B. C., 2017. Relações tectônicas no Central da Faixa Araçuaí: Análise estrutural por ASM e geocronologia U/Pb e Lu/Hf [Dissertação de Mestrado]: Instituto de Geociências da Universidade de São Paulo, 123 pp.
- Xiang, W., Griffin, W. L., Jie, C., Pinyun, H., Xiang, L. I., 2011. U and Th contents and Th/U ratios of zircon in felsic and mafic magmatic rocks: Improved zircon-melt distribution coefficients. *Acta Geologica Sinica-English Edition*, 85(1), 164-174.
- Wagner, J. J., Hedley, I. G., Steen, D., Tinkler, C., and Vuagnat, M., 1981. Magnetic anisotropy and fabric of some progressively deformed ophiolitic gabbros. *Journal of Geophysical Research: Solid Earth*, 86(B1), 307-315.
- Wetherill, G. W., 1956. An interpretation of the Rhodesia and Witwatersrand age patterns. *Geochimica et Cosmochimica Acta*, 9(5-6), 290-292.

APPENDIX

APPENDIX A – Location of the visited points in the study area and compiled measurements.

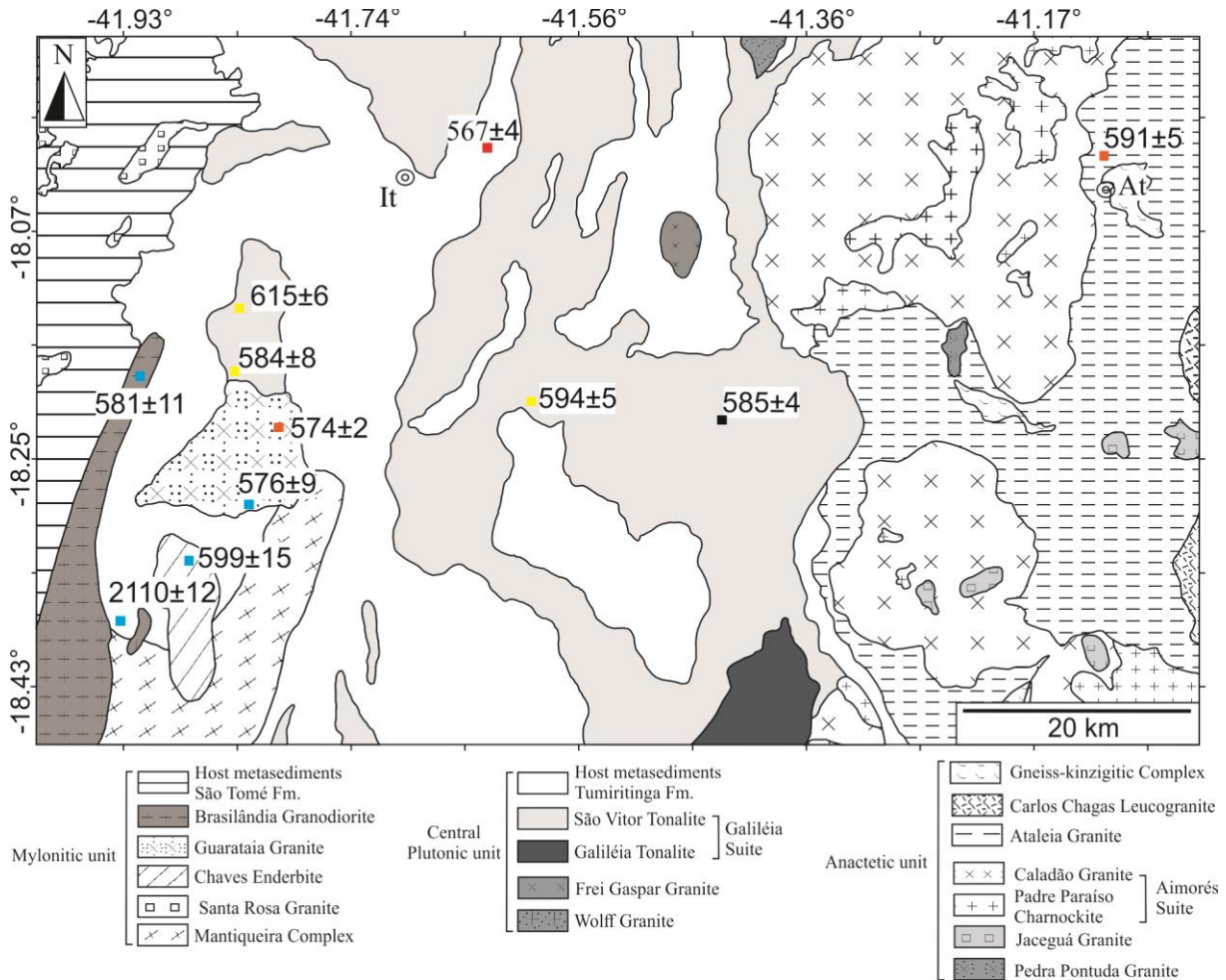
The numbers correspond to the localization of the sampled sites. The samples were named with a “TM” code before the corresponding number. Compiled samples are with the code before the numbers.

TM – this work; TFE – Sanchez (2014); BP – Portela (2013); TFN – (Pinto, 2015) – See references in the “Results” section.



APPENDIX B – Ages obtained in the study region

The ages are reported in million years (Ma). Blue, Yellow, Orange, Black, and Red dots correspond to: Tedeschi et al. (2016); Pinto (2015); Noce et al. (2000); Mondou (2010); and this work, respectively. Cities are represented by It (Itambacuri) and At (Ataléia).



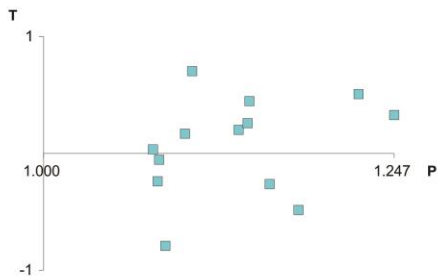
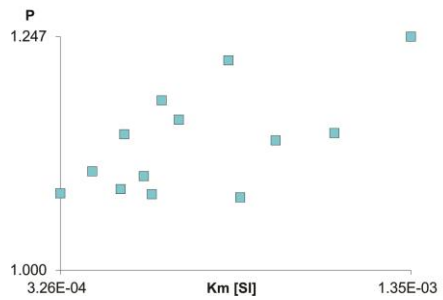
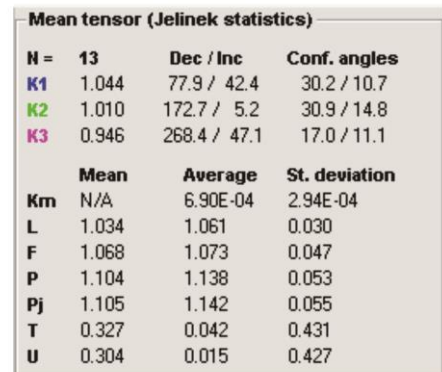
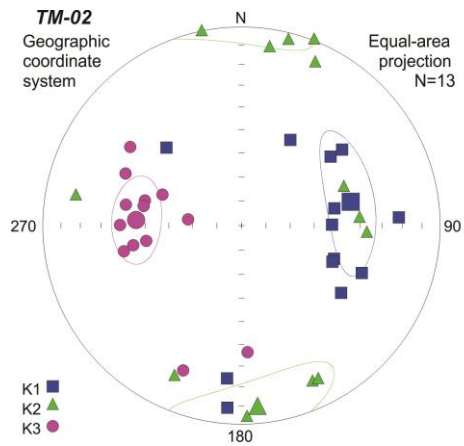
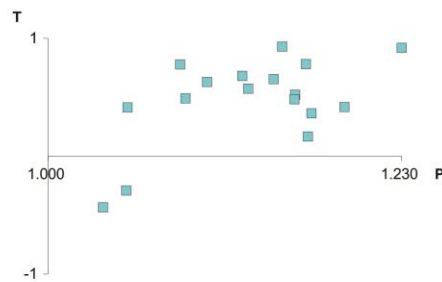
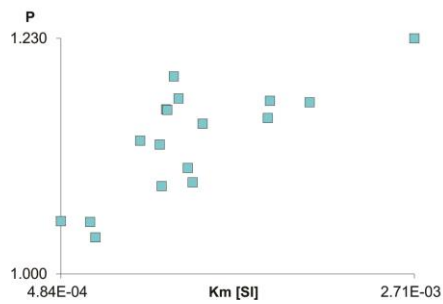
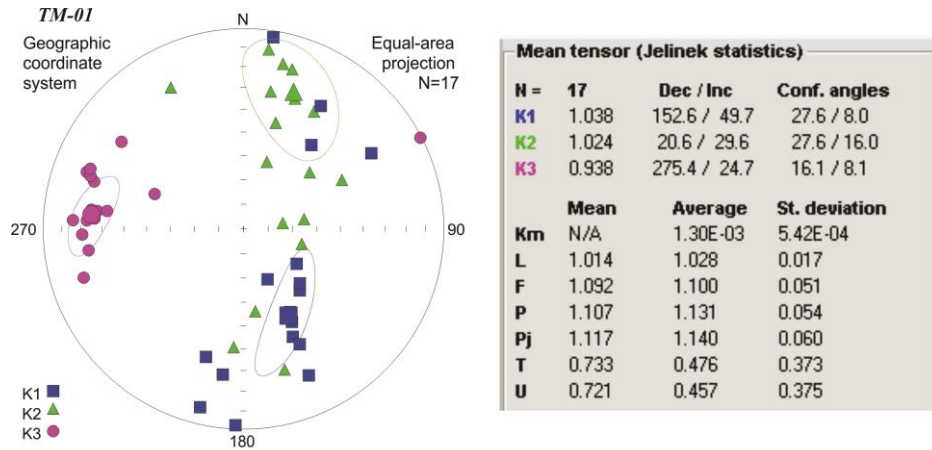
APPENDIX C – Parameters of the Vibrating Sample Magnetometer.

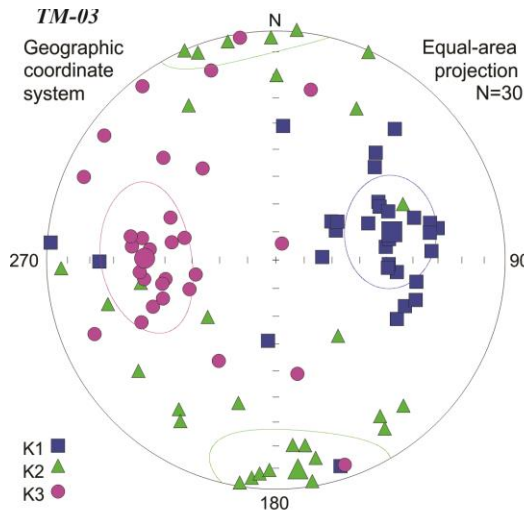
Parameters used during magnetic mineralogy investigations using vibrating sample magnetometer (VSM – MicroMag 3900 0 Princeton measurements Corporation) housed at the Oceanographic Institute of the University of São Paulo (Geoprocessing Laboratory – LabGeo).

Hysteresis Loops		Remanence Curves		First Order Reversal Curves	
Applied Field Maximum	1 T	Sequence	Non linear	Saturating field	600 mT
Applied Field Increment	2 mT	Initial Field	20 μ T	Hu (min)	-80 mT
Averaging Time	300 ms	Final Field	1 T	Hu (max)	80 mT
Pause at maximum field	1 s	Number of points	150	Hc (min)	0 T
Averages	1	Saturating field (DCD)	1 T	Hc (max)	150 mT
Saturate before measuring	No	pause at saturation	1 s	Averaging time	200 ms
Demagnetize before measuring	No	Pause at zero field	1 s	Field increment	1.08 mT
Include initial moment	No	Slew rate to applied field	1 T	Number of FORCs	300
Include hysteresis loop	Yes	Demagnetize before measurement	Yes	Allow for smoothing factor of	5
		Isothermal remanent moment	Yes	Pause at saturating field	200 ms
		DC demagnetization remanence	Yes	Pause at calibration field	150 ms
		Repeat saturation (in DCD)	No	Pause at reversal field	150 ms
		Include direct moment	No	Slew rate limit	1 T/s
				Include hysteresis loop	No
				Include Msi(H)?	No
				Save on completion (?)	No
				Repeat measurement ?	Yes
				Number of measurements	No
				Measurement time (approximate)	

APPENDIX D – AMS graphs and directional parameters.

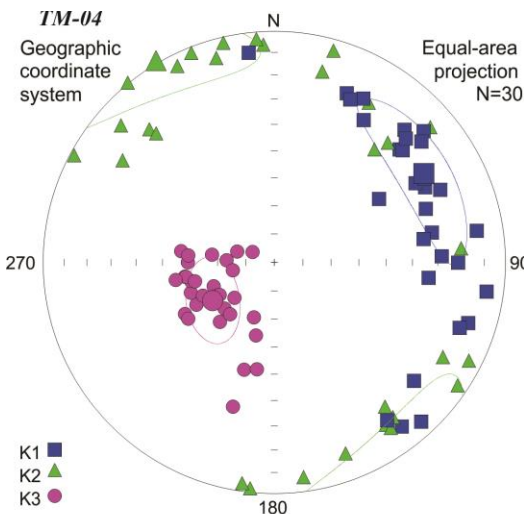
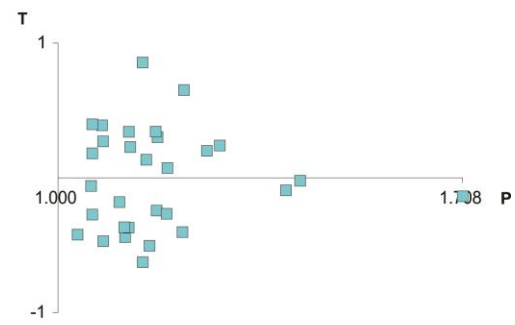
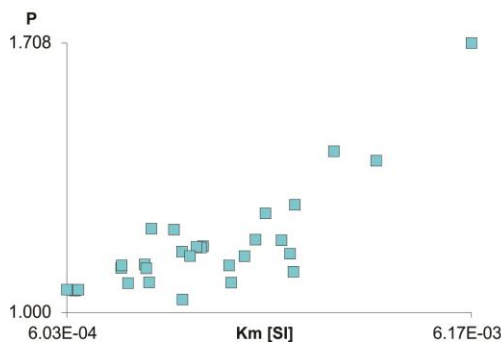
AMS graphs obtained for this work using Anisoft 4.2.





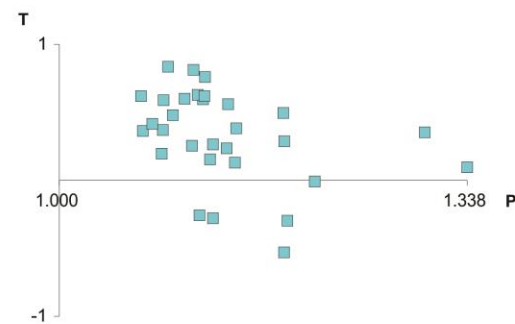
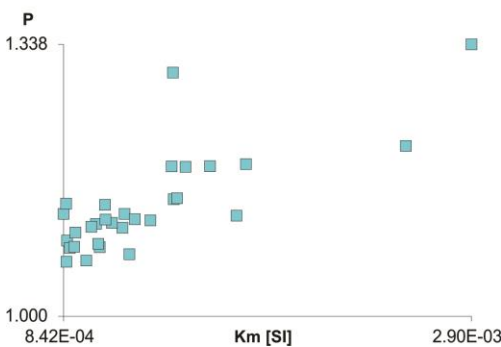
Mean tensor (Jelinek statistics)

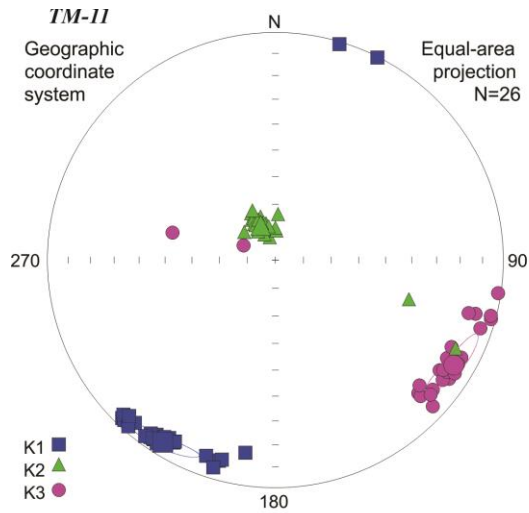
N =	30	Dec / Inc	Conf. angles
K1	1.061	76.3 / 46.8	19.2 / 17.1
K2	0.990	174.1 / 7.3	25.5 / 18.2
K3	0.949	270.7 / 42.3	25.2 / 17.5
	Mean	Average	St. deviation
Km	N/A	2.51E-03	1.30E-03
L	1.071	1.083	0.071
F	1.044	1.082	0.062
P	1.118	1.175	0.137
Pj	1.119	1.178	0.137
T	-0.230	-0.009	0.372
U	-0.256	-0.044	0.374



Mean tensor (Jelinek statistics)

N =	30	Dec / Inc	Conf. angles
K1	1.047	59.3 / 25.7	28.8 / 10.8
K2	1.014	329.1 / 0.4	28.8 / 14.3
K3	0.939	238.2 / 64.3	15.1 / 9.5
	Mean	Average	St. deviation
Km	N/A	1.26E-03	4.79E-04
L	1.032	1.048	0.038
F	1.080	1.085	0.036
P	1.115	1.137	0.062
Pj	1.119	1.142	0.062
T	0.416	0.324	0.341
U	0.394	0.298	0.349

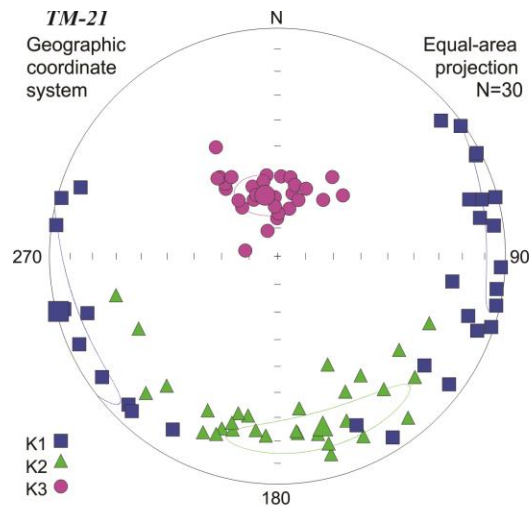
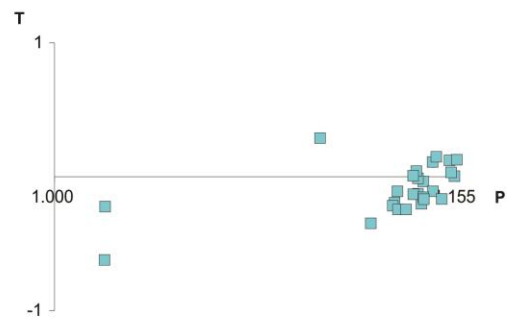
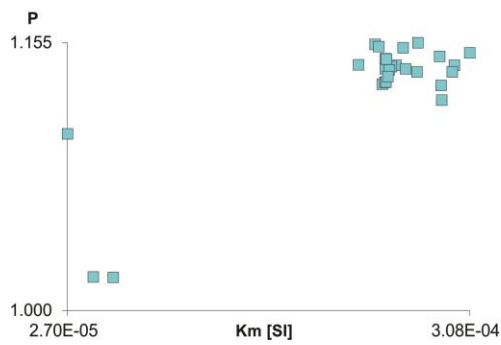




Mean tensor (Jelinek statistics)

N =	26	Dec / Inc	Conf. angles
K1	1.059	211.7 / 6.6	10.6 / 2.9
K2	0.993	334.5 / 78.0	4.6 / 2.8
K3	0.947	120.5 / 10.0	10.8 / 3.8

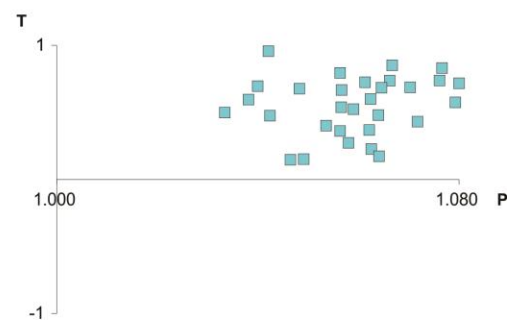
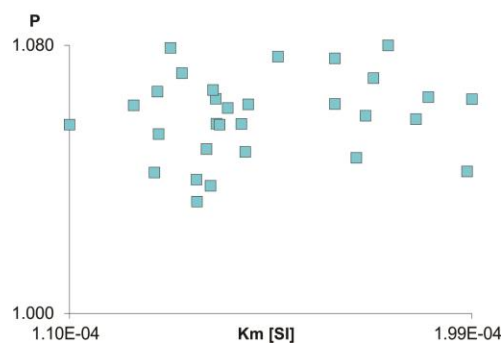
	Mean	Average	St. deviation
Km	N/A	2.38E-04	7.44E-05
L	1.066	1.067	0.019
F	1.049	1.059	0.020
P	1.118	1.130	0.034
Pj	1.119	1.131	0.034
T	-0.149	-0.093	0.186
U	-0.176	-0.123	0.182

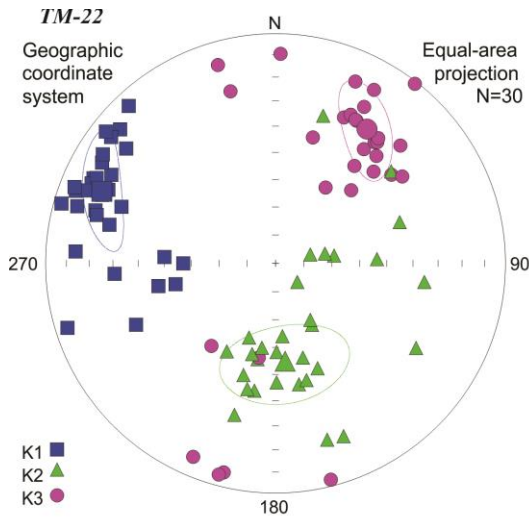


Mean tensor (Jelinek statistics)

N =	30	Dec / Inc	Conf. angles
K1	1.019	255.8 / 1.1	29.3 / 8.7
K2	1.012	165.4 / 22.2	28.8 / 7.8
K3	0.969	348.5 / 67.8	10.9 / 7.3

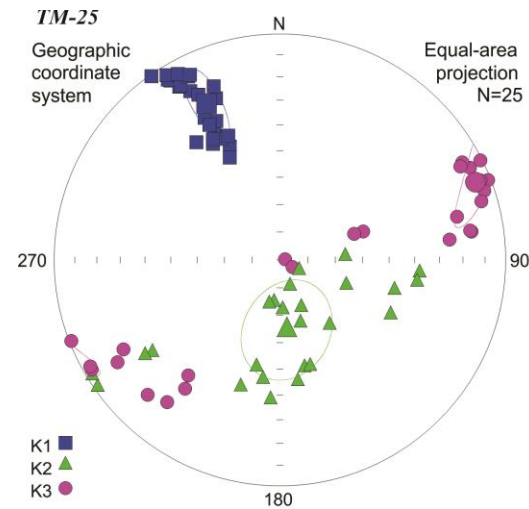
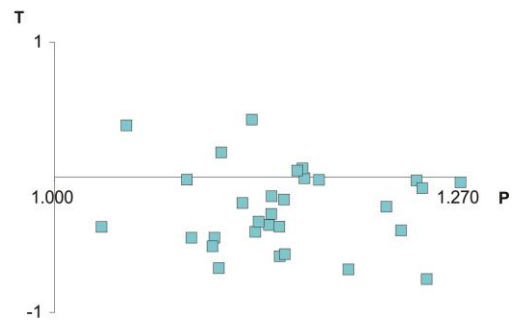
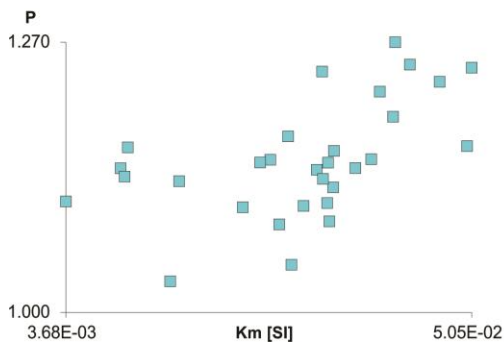
	Mean	Average	St. deviation
Km	N/A	1.53E-04	2.33E-05
L	1.007	1.013	0.006
F	1.044	1.046	0.013
P	1.052	1.059	0.012
Pj	1.056	1.062	0.014
T	0.720	0.553	0.218
U	0.714	0.544	0.221





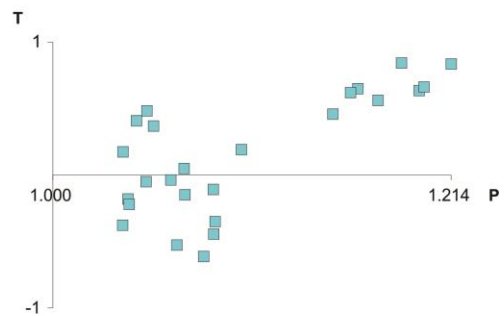
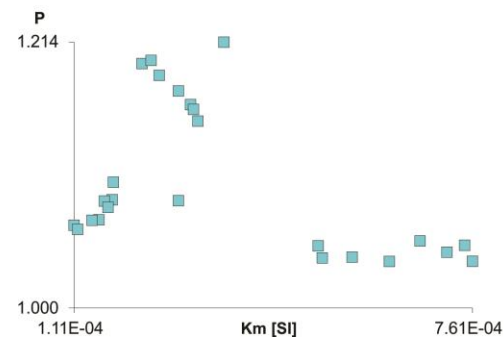
Mean tensor (Jelinek statistics)

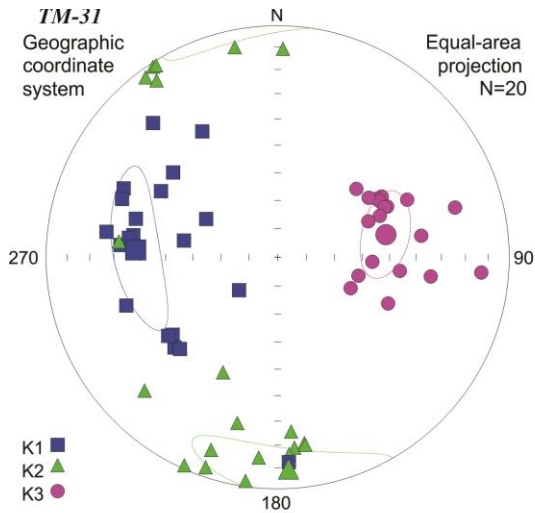
N =	Dec / Inc	Conf. angles
K1	1.065	292.5 / 19.3
K2	0.988	174.6 / 53.2
K3	0.948	34.2 / 30.0
Mean Average St. deviation		
Km	N/A	3.08E-02
L	1.078	1.092
F	1.042	1.055
P	1.123	1.152
Pj	1.125	1.156
T	-0.291	-0.231
U	-0.318	-0.261



Mean tensor (Jelinek statistics)

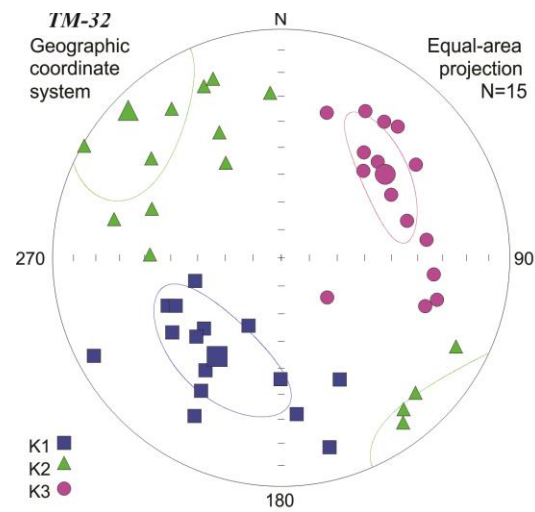
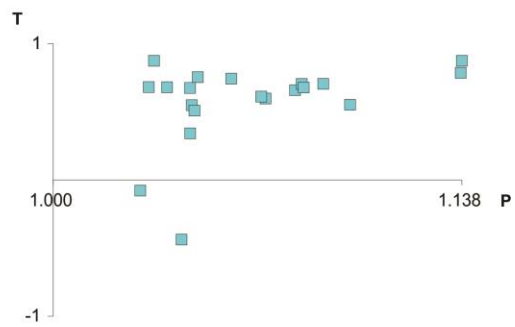
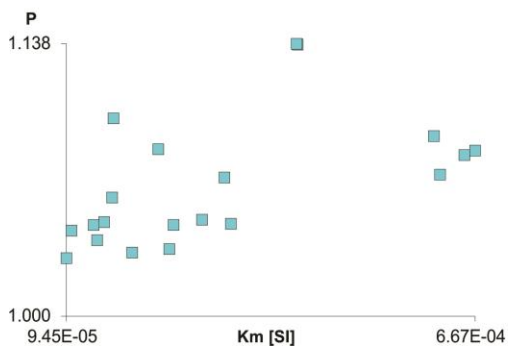
N =	Dec / Inc	Conf. angles
K1	1.039	334.8 / 24.6
K2	1.005	174.3 / 64.2
K3	0.956	68.3 / 7.6
Mean Average St. deviation		
Km	N/A	3.55E-04
L	1.033	1.032
F	1.052	1.066
P	1.087	1.101
Pj	1.088	1.106
T	0.215	0.156
U	0.195	0.139





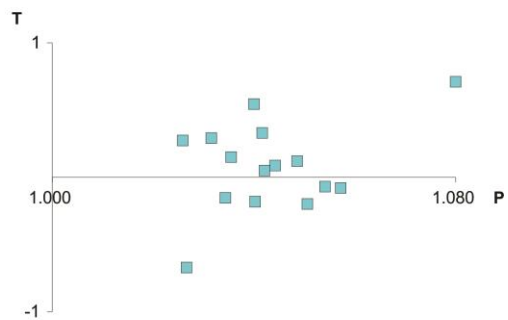
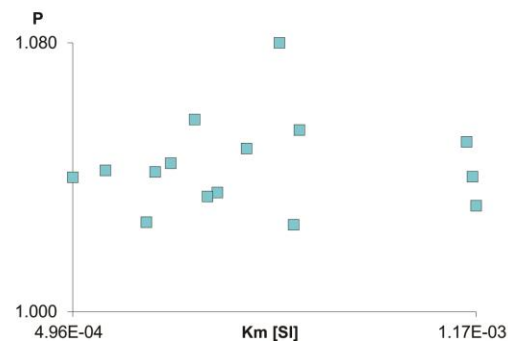
Mean tensor (Jelinek statistics)

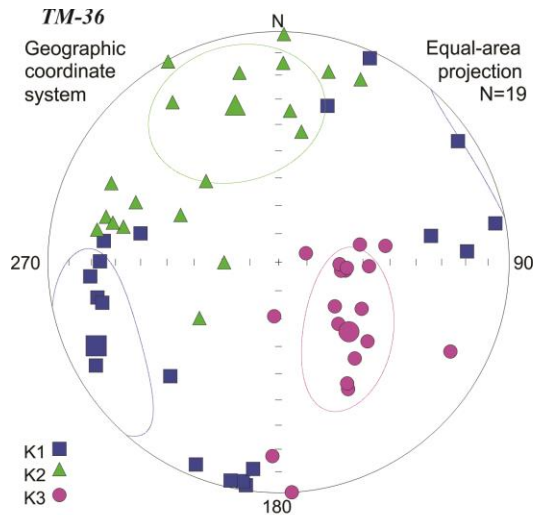
	Mean	Average	St. deviation
N = 20			
K1	1.022	273.0 / 38.6	27.0 / 9.0
K2	1.012	177.1 / 7.3	28.2 / 10.8
K3	0.966	78.2 / 50.5	15.2 / 8.6
Km	N/A	3.06E-04	1.93E-04
L	1.009	1.012	0.006
F	1.048	1.054	0.031
P	1.058	1.067	0.032
Pj	1.062	1.072	0.036
T	0.677	0.574	0.315
U	0.669	0.565	0.315



Mean tensor (Jelinek statistics)

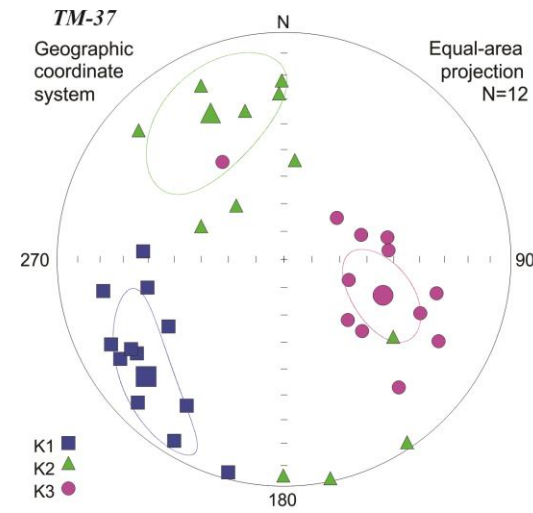
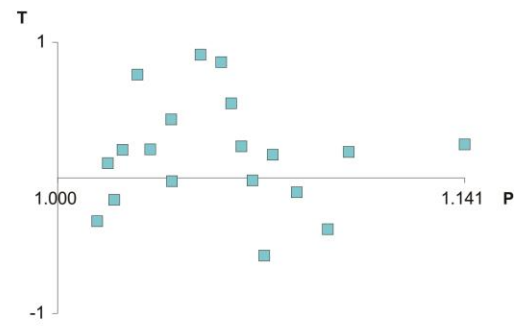
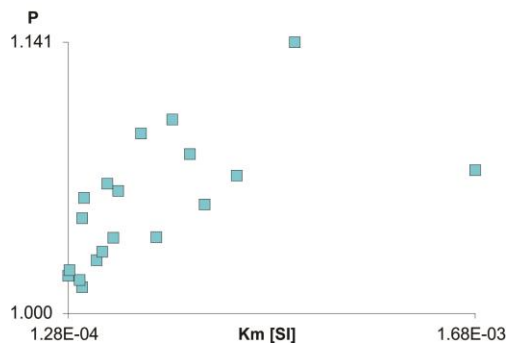
	Mean	Average	St. deviation
N = 15			
K1	1.015	213.0 / 47.3	29.2 / 15.0
K2	1.002	313.1 / 9.2	29.3 / 20.5
K3	0.983	51.3 / 41.2	23.5 / 9.2
Km	N/A	7.96E-04	2.16E-04
L	1.013	1.019	0.007
F	1.019	1.024	0.014
P	1.033	1.044	0.014
Pj	1.033	1.044	0.015
T	0.187	0.081	0.336
U	0.179	0.071	0.336





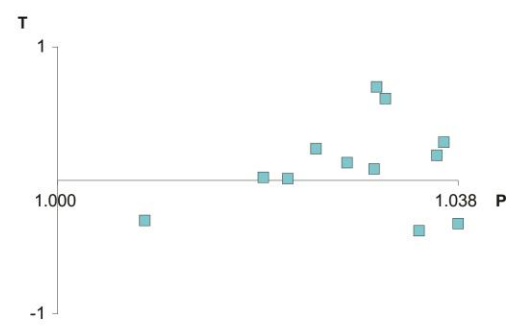
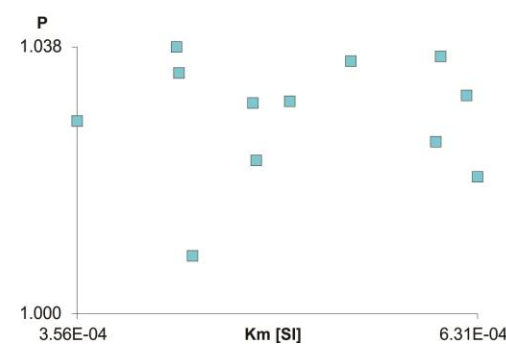
Mean tensor (Jelinek statistics)

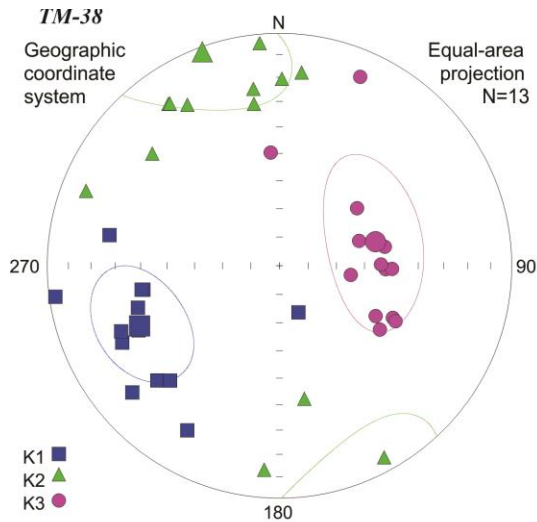
N =	19	Dec / Inc	245.3 / 14.1	Conf. angles	28.1 / 18.2
K1	1.018	245.3 / 14.1		28.1 / 18.2	
K2	1.002	344.2 / 31.7		27.9 / 27.5	
K3	0.980	134.7 / 54.7		29.2 / 16.1	
	Mean	Average	St. deviation		
Km	N/A	4.44E-04	3.81E-04		
L	1.016	1.023	0.019		
F	1.022	1.032	0.020		
P	1.038	1.056	0.033		
Pj	1.039	1.058	0.034		
T	0.149	0.173	0.404		
U	0.140	0.161	0.407		



Mean tensor (Jelinek statistics)

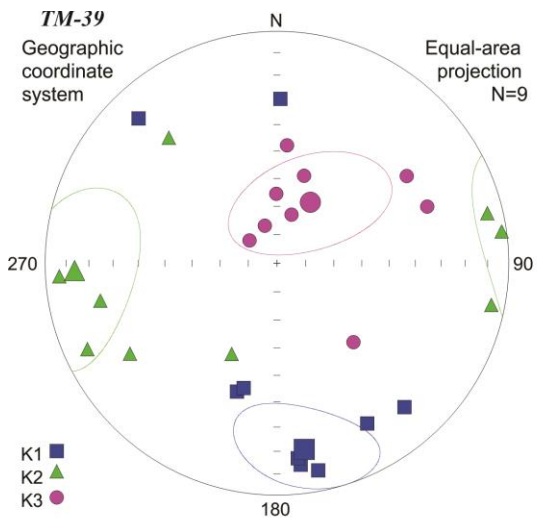
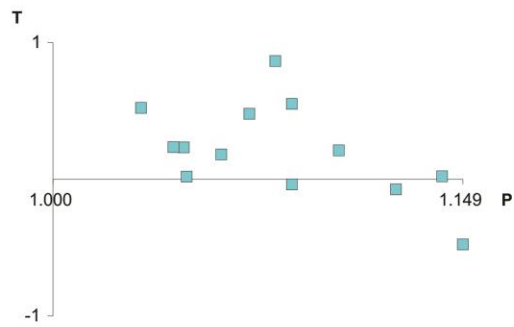
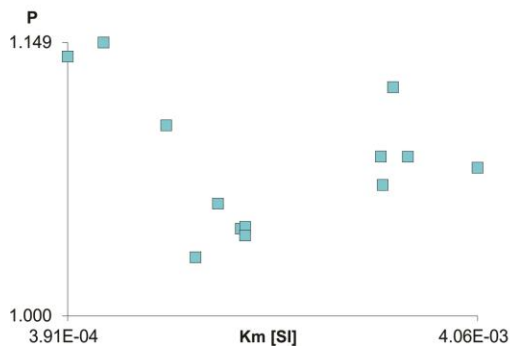
N =	12	Dec / Inc	229.6 / 21.3	Conf. angles	28.5 / 10.7
K1	1.011	229.6 / 21.3		28.5 / 10.7	
K2	1.001	332.7 / 30.2		28.7 / 19.0	
K3	0.989	110.0 / 51.7		19.4 / 10.5	
	Mean	Average	St. deviation		
Km	N/A	5.09E-04	9.17E-05		
L	1.010	1.012	0.006		
F	1.012	1.016	0.007		
P	1.022	1.028	0.009		
Pj	1.022	1.029	0.009		
T	0.110	0.107	0.339		
U	0.104	0.101	0.340		





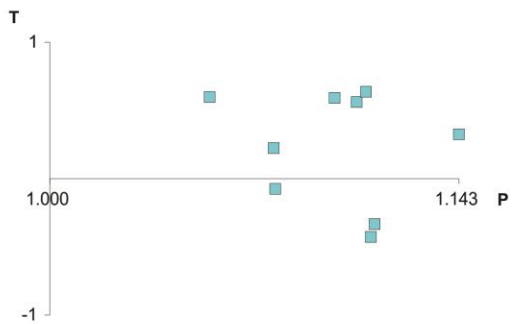
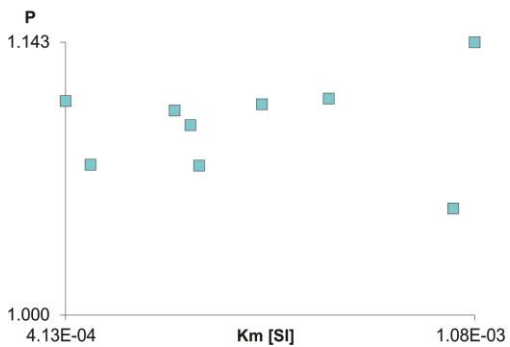
Mean tensor (Jelinek statistics)

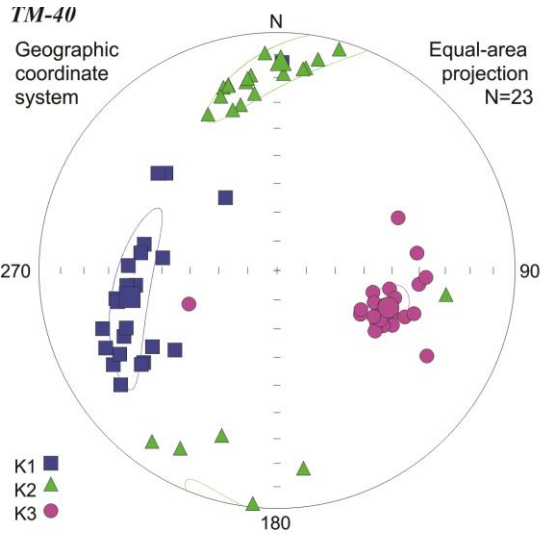
N =	13	Dec / Inc	Conf. angles
K1	1.028	246.8 / 34.8	20.3 / 17.3
K2	1.000	339.8 / 4.3	30.0 / 19.3
K3	0.972	76.0 / 54.9	30.4 / 17.6
	Mean	Average	St. deviation
Km	N/A	2.21E-03	1.13E-03
L	1.028	1.035	0.030
F	1.029	1.046	0.018
P	1.057	1.083	0.038
Pj	1.057	1.085	0.039
T	0.019	0.210	0.342
U	0.005	0.193	0.348



Mean tensor (Jelinek statistics)

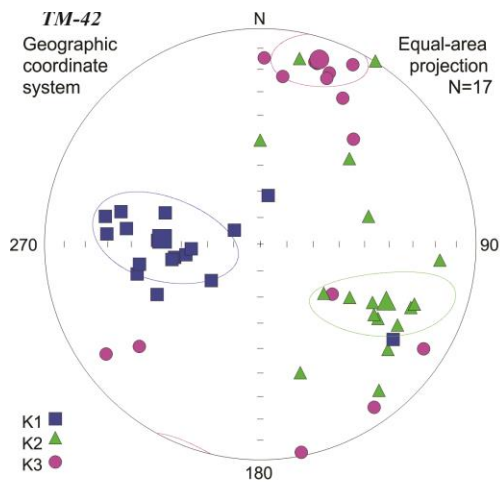
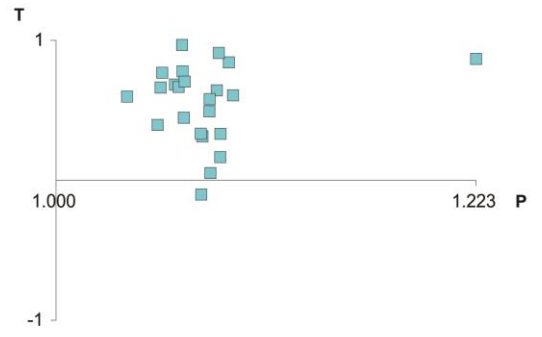
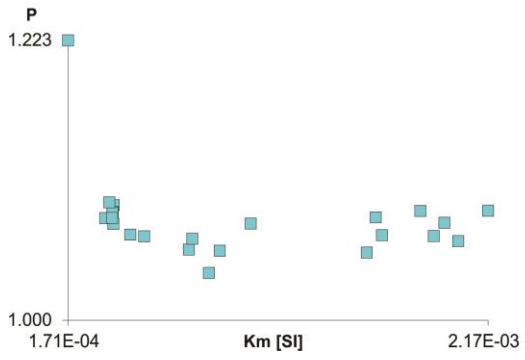
N =	9	Dec / Inc	Conf. angles
K1	1.027	163.7 / 7.2	55.5 / 18.6
K2	1.007	256.7 / 22.6	53.8 / 30.0
K3	0.966	57.0 / 66.1	33.3 / 28.8
	Mean	Average	St. deviation
Km	N/A	6.43E-04	2.20E-04
L	1.019	1.050	0.033
F	1.043	1.068	0.031
P	1.062	1.121	0.051
Pj	1.064	1.124	0.051
T	0.376	0.169	0.398
U	0.363	0.145	0.402





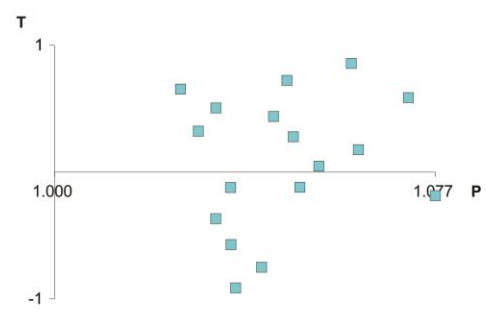
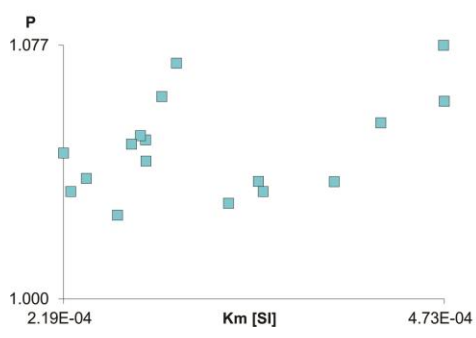
Mean tensor (Jelinek statistics)

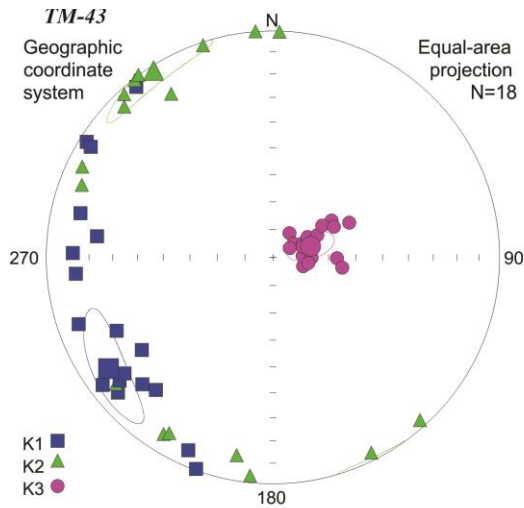
N =	23	Dec / Inc	Conf. angles
K1	1.025	259.7 / 37.2	29.4 / 6.8
K2	1.016	1.0 / 14.5	29.3 / 7.1
K3	0.959	108.4 / 49.1	8.1 / 6.7
	Mean	Average	St. deviation
Km	N/A	9.94E-04	6.78E-04
L	1.009	1.017	0.011
F	1.060	1.062	0.034
P	1.069	1.080	0.034
Pj	1.075	1.085	0.039
T	0.744	0.553	0.277
U	0.737	0.541	0.281



Mean tensor (Jelinek statistics)

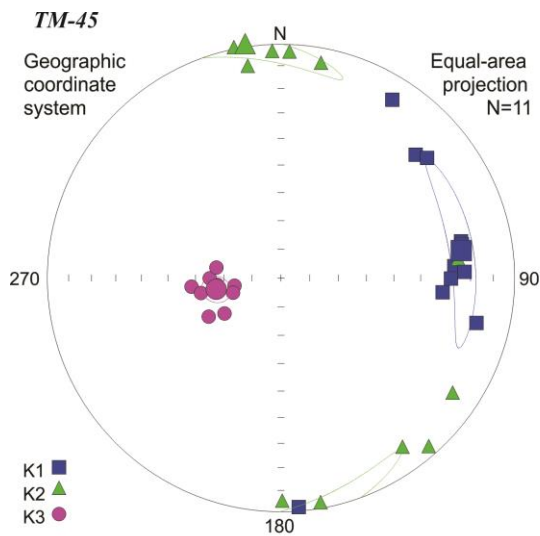
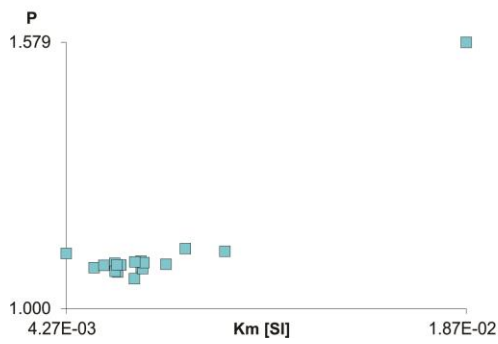
N =	17	Dec / Inc	Conf. angles
K1	1.016	273.1 / 52.4	30.0 / 15.1
K2	1.001	115.6 / 35.4	30.0 / 11.1
K3	0.983	17.7 / 11.0	15.6 / 11.6
	Mean	Average	St. deviation
Km	N/A	3.18E-04	8.27E-05
L	1.015	1.020	0.012
F	1.018	1.026	0.016
P	1.033	1.046	0.015
Pj	1.033	1.048	0.015
T	0.104	0.092	0.529
U	0.096	0.084	0.528





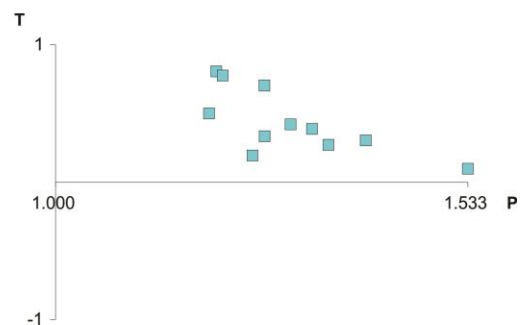
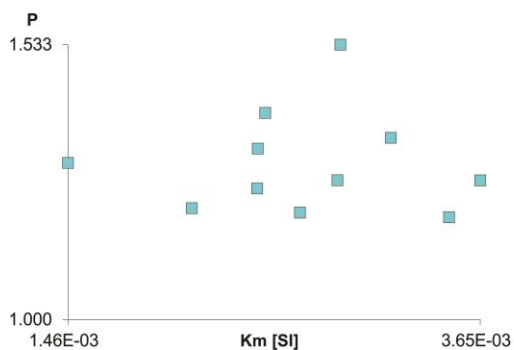
Mean tensor (Jelinek statistics)

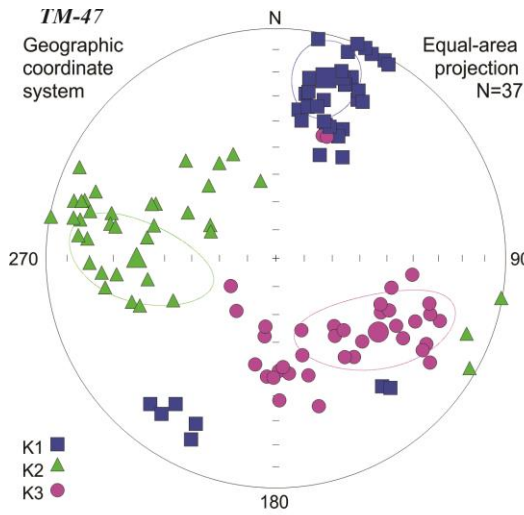
N =	18	Dec / Inc	Conf. angles
K1	1.043	235.9 / 13.5	18.3 / 7.5
K2	1.018	326.9 / 4.1	17.8 / 4.8
K3	0.939	73.4 / 75.9	9.0 / 4.5
	Mean	Average	St. deviation
Km	N/A	7.35E-03	3.10E-03
L	1.025	1.037	0.066
F	1.083	1.082	0.037
P	1.110	1.124	0.115
Pj	1.116	1.129	0.114
T	0.527	0.506	0.236
U	0.508	0.485	0.255



Mean tensor (Jelinek statistics)

N =	11	Dec / Inc	Conf. angles
K1	1.100	81.3 / 23.0	28.3 / 5.0
K2	1.041	351.1 / 0.4	28.3 / 4.5
K3	0.860	260.1 / 67.0	5.2 / 4.5
	Mean	Average	St. deviation
Km	N/A	2.71E-03	6.19E-04
L	1.057	1.084	0.056
F	1.211	1.201	0.038
P	1.279	1.303	0.099
Pj	1.295	1.314	0.094
T	0.553	0.436	0.236
U	0.509	0.383	0.261





Mean tensor (Jelinek statistics)

N =	Dec / Inc	Conf. angles
K1	1.031 15.5 / 19.6	17.1 / 9.8
K2	1.002 268.6 / 39.3	29.2 / 13.0
K3	0.968 125.8 / 44.3	29.4 / 13.1

	Mean	Average	St. deviation
Km	N/A	3.11E-04	1.47E-04
L	1.029	1.035	0.019
F	1.035	1.056	0.049
P	1.065	1.093	0.050
Pj	1.066	1.098	0.054
T	0.092	0.021	0.530
U	0.076	0.005	0.526

